AN ABSTRACT OF THE DISSERTATION OF

Mauro A. Alves for the degree of Doctor of Philosophy in Physics presented on March, 13, 2003.

Title: The Dynamics of Oxygen Vacancies in Zirconia: An Analysis of PAC Data

Abstract Approved:

Redacted for privacy

John A. Gardner

Nuclear techniques such as perturbed angular correlation (PAC) sample the hyperfine interactions of a large number of probe atoms in specific crystallographic sites. Real crystals contain static defects producing a distribution of electric field gradients (EFGs) that add to the ideal EFG of the crystal at any given probe site. Also, dynamic defects like moving vacancies and interstitial atoms can be present in the crystal and contribute to the distribution of EFGs. The distribution of EFGs leads to line broadening and a change in the observed asymmetry parameter η since the total EFG no longer has the symmetry of the perfect crystal. When both defects are present in a material, obtaining quantitative information from the analysis of PAC spectra is usu-

ally very difficult since great care has to be taken to ensure that the source of line broadening is identified correctly. In order to relate the relationship between the static line broadening and changes in the asymmetry parameter η, a uniform random distribution of point charges was used to simulate the static defect EFG. PAC spectra collected on cubic niobium metal, cubic stabilized zirconia and Nb-doped tetragonal zirconia were fitted with this model. Although the quality of the fits is good, more work is needed to clarify the relationship between the new model parameters and the line broadening and asymmetry parameter derived from conventional model fits. The PAC spectra of Nb-doped tetragonal zirconia were fitted with a conventional static model to establish a reliable relationship between line broadening and the asymmetry parameter when only static defects are present in a sample. To account for effects of dynamic defects, a four state stochastic model for vacancy motion was adapted in order to include the line broadening and changes in the asymmetry produced by static defects. As a result, the activation energies corresponding to the rates at which a oxygen vacancy is trapped by, detraps from, and hops among equivalent sites about a PAC probe atom were calculated. The values that were found are physically reasonable, indicating that the dynamics of an oxygen vacancy around a PAC probe atom are satisfactorily described.

The Dynamics Of Oxygen Vacancies In Zirconia: An Analysis Of PAC Data

by
Mauro A. Alves

A DISSERTATION

submitted to

Oregon State University

in partial fulfillment of
the requirements for the
degree of

Doctor of Philosophy

Presented March 13, 2003
Commencement June 2003

Doctor of Philosophy dissertation of Mauro A. Alves presented on March 13, 2003

APPROVED:

Redacted for privacy

Major Professor, representing Physics

Redacted for privacy

Head of Department of Physics

Redacted for privacy

Dean of Graduate School

I understand that my dissertation will become part of the permanent collection of Oregon State University Libraries. My signature below authorizes release of my dissertation to any reader upon request.

Redacted for privacy

Mauro A. Alves, Author

ACKNOWLEDGMENTS

It is a pleasure to acknowledge the help and encouragement of all with whom I have been involved during my stay at the Department of Physics. Without their support I would not be able to come this far.

First, it is with respect and appreciation that I express my deepest gratitude to my advisor Professor John A. Gardner for his guidance, support and patience throughout these years. He has been a reliable source of encouragement and inspiration during my work.

Also, I especially want to thank Professor Dr. William E. Evenson for the very helpful and stimulating discussions and for being so generous with his time. Dr. Evenson also reviewed this thesis and corrected many embarrassing errors.

I consider myself very fortunate to have had the opportunity to work with these two fine scientists.

I am very grateful to the Department of Physics for the financial support, and to Dr. Henry Jansen for his help and understanding during some rather difficult times.

I would like to express my appreciation to the previous graduates students and members of the PAC group at Oregon State University, and in particular to: Dr. John Griffith, Dr. Herbert Jaeger, Dr. Theresa A. Lee, Dr. Niels Mommer and Dr. Matthew O. Zacate. Their diligent work on PAC provided a wealth of information from which I constantly resorted to. The PAC data used in this work were collected by Dr. Herbert Jaeger, Dr. Theresa A. Lee, Dr. Niels Mommer and Dr. William Warnes. Many thanks go to Mr. Ethan

Bernard who provided the multiple data set fitting program used in this work. This fitting program was an essential tool for the data analysis in parts of this work.

I want to thank the Conselho Nacional de Desenvolvimento e Pesquisa (CNPq - Brazil) for their financial support during the first part of my graduate work, at the College Of Oceanic and Atmospheric Sciences, and for making it possible for me to continue my graduate studies at the Department of Physics.

TABLE OF CONTENTS

TABLE OF CONTENTS (continued)

LIST OF FIGURES

LIST OF FIGURES (continued)

LIST OF FIGURES (continued)

LIST OF FIGURES (continued)

LIST OF TABLES

The Dynamics Of Oxygen Vacancies In Zirconia: An Analysis Of PAC Data

1 INTRODUCTION

Zirconia is a material with wide potential for applications in modern industry due to its unique properties. It is tough, strong and is resistant to caustic and corrosive chemicals. Its uses range from the cubic zirconia crystal, commonly used in jewelry, to special ceramics with high ionic conductivity that are found in oxygen sensors, high temperature heating elements, catalytic converters, and solid electrolyte fuel cells. It can be used as a refractory material due to its high melting point. Also, due to its nonreactive nature and its biocompatibility it can be used in prosthetic devices.

In spite of all its useful characteristics for technological applications, zirconia cannot usually be employed in its pure form. Zirconia can exist in more than one crystalline structure. The phases of pure solid zirconia at ambient pressure are monoclinic, tetragonal and cubic. During a phase transition from the monoclinic to the tetragonal form there is a significant change in volume. This volume change makes zirconia, in its pure form, unusable for engineering applications where one needs to fabricate ceramic devices with this material.

In order to suppress this phase transition, dopants are added so that the mechanical characteristics of zirconia are improved. These dopants can alter the ionic conductivity of these materials. For example, when a lower-valence dopant like Y_2O_3 is used, the negative charge introduced by the dopant is compensated by the formation of oxygen vacancies. The oxygen vacancies that are thus formed increase the ionic conductivity of the ceramic material. On the other hand, lower valence dopants can trap these oxygen vacancies and in the process reduce the ionic conductivity of the material. Macroscopic techniques like conductivity measurements and thermogravimetric analysis have been used to measure ionic conductivity in ceramic materials. But the results are sparse and non-conclusive. Moreover, the high temperatures at which these measurements need to be made (the operating temperatures of some of the ceramic devices) can affect the quality of such measurements.

Perturbed angular correlation of γ rays (PAC) is a non-contact nuclear measuring technique that allows probing the microscopic environment around a probe nucleus. PAC requires the introduction of very small quantities of radioactive atoms to the sample being studied. The angular correlation of gamma rays emitted by the probe nucleus is affected by electric field gradients (EFGs) due to the charges of the crystal lattice and defects present in the sample material. The oxygen vacancies introduced by the dopants are dynamic defects. The vacancies are free to move around the probe nucleus and perturb the angular correlation of the emission of gamma rays. In the sample material there are a number of other kinds of defects. Static defects must be taken into consideration when the PAC technique is used. Interstitial ions, stresses in the crystalline structure, and impurities are examples of static defects that can produce electric field gradients and perturb the angular correlation of gamma rays.

If the PAC technique is employed to study the dynamics of oxygen vacancies in zirconia ceramics, one must be able to separate the effects of the static and dynamic defects. Fig. 1.1 shows, schematically, how these effects add up. As an example, it is shown how the PAC spectrum and perturbing function should look for a probe atom located in the interior of an ideal tetragonal crystal under the influence of static and dynamic defects. The perturbation function shows the characteristic oscillations that results from the hyperfine splitting frequencies. The presence of defects leads to the broadening of the PAC spectral lines and damping of the PAC perturbation function, $G_{22}(\mathrm{t})$.

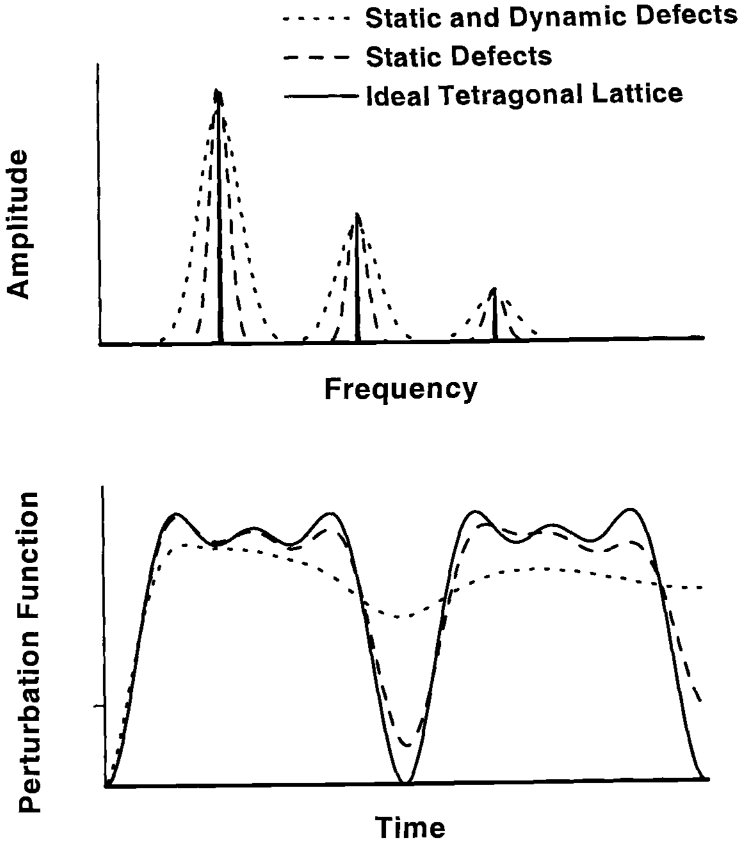

Figure 1.1: Simplified representation of the effects of the presence of static and dynamic defects on the PAC spectrum and perturbation function. The spectral line broadening (top) and the damping of the perturbation function $G_{22}(\mathrm{t})$ (bottom) are a direct result of the presence of defects in the material.

It is possible to identify qualitatively the contribution of static and dynamic defects. The perturbing function that describes the influence of the defects is temperature-dependent. The contribution of static defects to the perturbation is weakly dependent on the temperature, and it is due to the expansion of the crystalline lattice. On the other hand, the motion of ions in a material is highly dependent on the temperature. At high temperatures the rapid motion of the ionic conductors averages out the perturbations; at lower temperature the presence of dynamic defects is more discernible.

Various studies have addressed the problem of quantifying and modeling the presence of static defects in crystalline structures. But, they neither yield satisfactory results nor present quantitative expressions that could be directly used in a PAC experiment. For this reason the main objective of this thesis is to develop a method to quantify the contributions of the static defects and to extract the contribution of static-defect-related line broadening in cases where dynamic line broadening is also present. As a direct result of this analysis, quantities directly related to the ionic conductivity of zirconia, the trapping, detrapping and hopping of oxygen vacancies, will be determined. An overview of PAC theory is presented in Chapter 2. Chapters 3 and 4 are concerned with the description of materials and methods used in this work. In Chapter 3 a review of zirconia ceramics is given. The data used in this work, the experimental procedure and the data handling are briefly described in Chapter 4. Chapter 5 is devoted to presentation of a model that seeks to simulate the presence of static defects and their influence in the PAC data. Chapter 6 details the results of a second model used to simulate the distribution of static defects. Chapter 7 is a summary of this work.

2 PERTURBED ANGULAR CORRELATION

Like Mössbauer spectroscopy, nuclear magnetic resonance (NMR), and nuclear quadrupole resonance (NQR), perturbed angular correlation (PAC) is a nuclear technique that measures the hyperfine interaction between the nuclear moment and electromagnetic fields.

In the case of PAC, what is measured is the hyperfine interaction between the quadrupole moment of a probe nucleus and the electric field gradient (EFG) generated by the electronic charge in the environment about the probe. PAC is a technique that has been widely utilized to study the properties of very different materials. It has emerged as an important materials characterization technique. PAC provides atomic scale information about the structure and function of materials in physics, chemistry and biology [1, 2, 3, 4]. PAC has some advantages when compared to other hyperfine interactions techniques: It gives the same signal efficiency at all temperatures. Also, the quantity of probe nuclei needed in a typical PAC experiment is very small, on the order of $10^{11} - 10^{12}$ atoms. This assures that the probe nuclei in the sample material are very dilute. Therefore they do not affect the overall properties of the material being studied. Note, however that the probe must also be seen as an impurity center in the sample material, since it is not native to the sample, usually.

The radiations emitted by a radioactive atom as it decays are not randomly distributed in space. They obey a given angular pattern, or in other words, they are correlated. In the case of PAC, and particularly for this thesis, one is interested in the correlation between the emission of two successive γ rays by a probe nucleus. In order to be useful in a PAC experiment, the γ

rays emitted by a radioactive atom must have different energies in such a way that it is possible for a detector to distinguish between those two radiations. Also, the time interval between emissions has to be large enough to be measurable (> 10 ns), but it should be small enough to avoid a high probability of the simultaneous detection of other decaying atoms ($<$ several microseconds). Moreover, the radioactive probe must have chemical characteristics that will allow its incorporation into the material to be studied. As a consequence of these requirements, only a few atoms can be used as PAC probes. The data analyzed in this thesis were collected in PAC experiments that used two different probes: ^{181}Hf and ^{111}In.

A very interesting characteristic of hafnium is that most zirconium minerals contain about 1% of this metal occupying substitutional zirconium positions; i.e. zirconia materials usually contain about 1% of HfO_2 [47]. The PAC probe, ^{181}Hf can be obtained by the irradiation of the sample material by thermal neutrons. The most important features of the decay scheme of ^{181}Hf are shown in Fig. 2.1. ^{181}Hf decays by the emission of a β^-, and has a half life of 42.4 days. The excited state of ^{181}Ta has a half-life of 17.8 μs. The decay to the ground state can occur by the emission of different γ rays. Of interest in PAC are the 133 keV and the 482 keV radiations. The intermediate state in this cascade has a 10.8 ns half-life, and has a quadrupole moment, $Q_{+5/2} = 2.36(5)$ b, that interacts with the sample material EFG [5].

The decay scheme for ^{111}In is shown in Fig. 2.2. It decays to an excited level of ^{111}Cd by electron capture. The excited state of ^{111}Cd has a half-life of 120 ps. The decay to the ground level occurs by the emission of two successive γ rays of energies 171 keV and 245 keV. The half-life of the intermediate level is 85 ns.

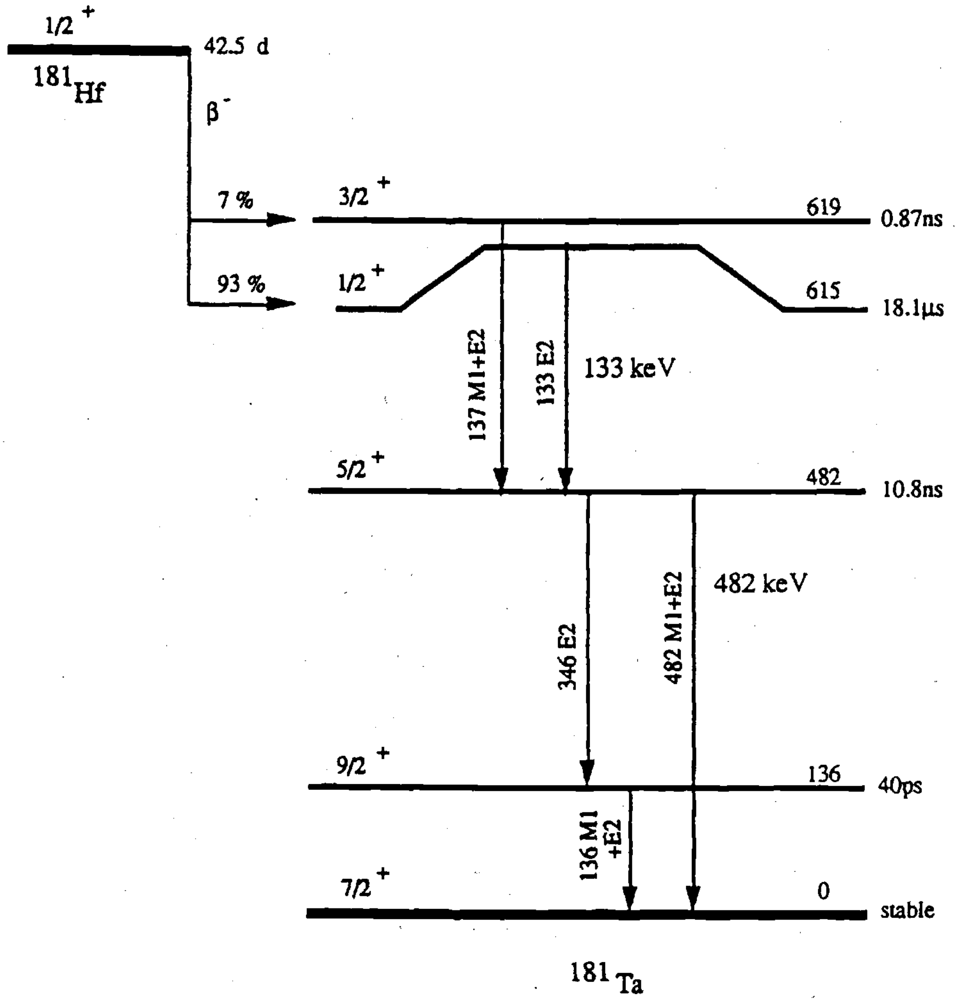

Figure 2.1: Decay scheme of ^{181}Hf ⟶ ^{181}Ta.

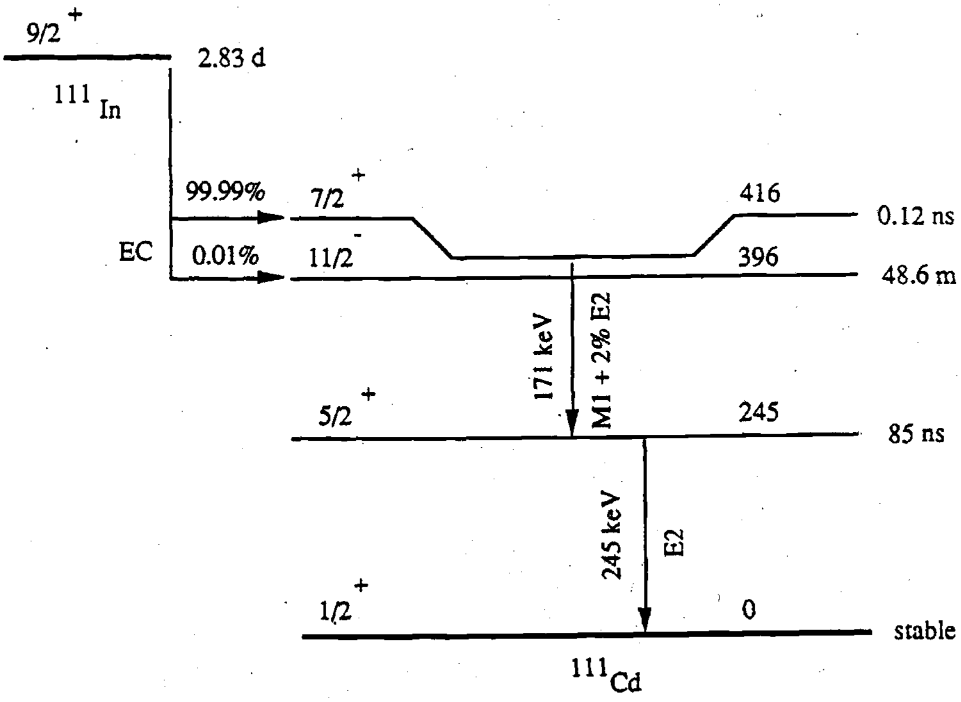

Figure 2.2: Decay scheme of ^{111}In $\longrightarrow$ ^{111}Cd.

The interaction with a local EFG is proportional to a quadrupole moment of $Q_{+5/2} = 0.83(13)$ b. ^{111}In is the most often used PAC probe. It is available commercially as indium chloride in dilute HCl solution.

To measure the angular correlation between the radiations emitted by the probe nuclei, it is necessary to define a given orientation in space. In a bulk experiment, as is performed with zirconia materials, this is not possible. The relatively large number of probe nuclei in a sample have the nuclear quadrupole principal axes randomly oriented, which prevents the choice of any favored spatial orientation. The randomness in the orientation can be removed in two ways. The first one consists in lowering the temperature of the sample material in very strong electric field gradients. In the second one, the spatial orientation is defined by the emission of the first γ ray, γ_1 of the cascade decay, and a detector at an arbitrary position. The direction of emission of γ_1 is then used to define a quantization z-axis. Associated to the z-direction is the quantum number m. The conservation of angular momentum in a radioactive decay dictates that only certain intermediate nuclear m-states take part in the decay. So, by choosing the direction of emission of the γ_1 ray of the cascade, a population of nuclei oriented with a specific angular distribution are selected. In this way it is possible to measure the angular correlation of γ_2 with respect to γ_1. As a result it is observed that radiation is emitted according to an anisotropic pattern [6]. This anisotropic radiation pattern is shown in Fig. 2.3. Angular correlation experiments are useful to obtain nuclear properties such as spins, parities of nuclear states and occasionally the magnetic moment of nuclear levels.

The angular correlation as described above occurs for nuclei in a region of space where there are no EFGs. In this situation, the measurements of coincidences and the recording of the number of radiations γ_2 by a detector in a fixed position in space will result in exponential decay with half-life equal to the half-life of the intermediate state of the probe being used.

A probe nucleus, when introduced in a material, will feel the effects of the local EFG. This interaction will then perturb the angular correlation of emission of the radiations. By measuring the γ_2 decays, as indicated above, one can observe, superimposed on the exponential decay curve, "oscillations" or "wiggles". These wiggles are a direct result of the hyperfine interaction between the quadrupole moment of the nuclei and the local EFG.

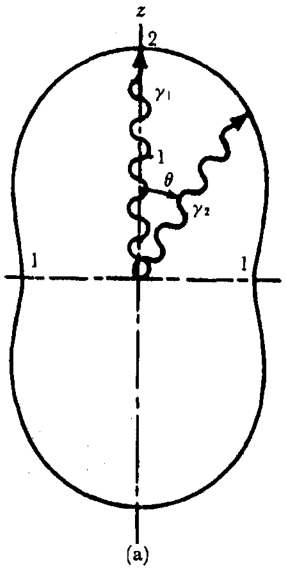

Figure 2.3: Angular distribution of γ_2 with respect to the direction of a preceding γ_1 in a radioactive transition [7].

In order to better understand the results obtained in a PAC experiment, in the following sections will be discussed the theory describing the angular correlation of γ rays and the perturbations caused by the presence of static and time dependent EFGs. The formal theory of PAC is rather complicated. Other theses and publications have described it in detail [40, 47, 49, 5, 8]. In this thesis, the main results of PAC theory will be presented in a compact way, based on previous Ph.D. dissertations from our department [47, 9, 10]. The reader interested in the formal theory of PAC is referred to the references listed above.

2.1 THE ANGULAR CORRELATION FUNCTION

In a nuclear cascade $I_i \rightarrow I \rightarrow I_f$, the initial state $|I_i, M_i\rangle$ decays by the emission of radiation γ_1 into the intermediate state $|I, M\rangle$, and then into the final state $|I_f, M_f\rangle$ by the emission of γ_2. The probability that these two radiations are emitted in the directions $\mathbf{k}_1$ and $\mathbf{k}_2$ into the solid angles $d\Omega_1$ and $d\Omega_2$ is given by $W(\mathbf{k}_1, \mathbf{k}_2, t)d\Omega_1 d\Omega_2$, where t is the time separation of emission of the radiations (see Fig. 2.4). The function $W(\mathbf{k}_1, \mathbf{k}_2, t)$ defines the angular correlation of γ_1 and γ_2.

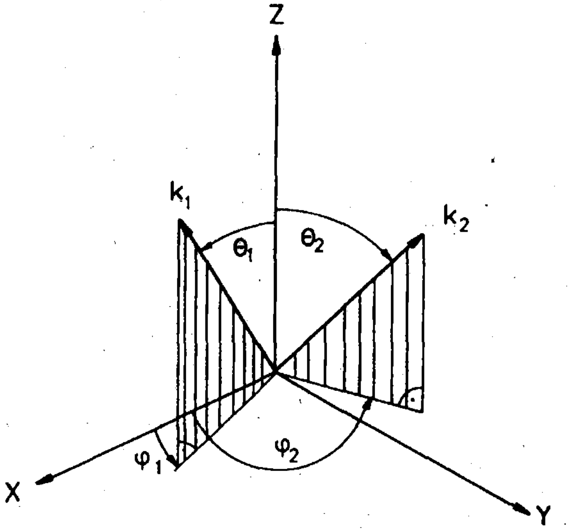

Figure 2.4: Angles used for the definition of the γ_1 and γ_2 radiation directions.

Using density matrix formalism, the most general form of the angular correlation function is

$$W(\mathbf{k}_1, \mathbf{k}_2, t) = Tr[\rho(\mathbf{k}_1, t)\rho(\mathbf{k}_2, 0)] = \sum_{mm'} \langle m|\rho(\mathbf{k}_1, t)|m'\rangle\langle m'|\rho(\mathbf{k}_2, 0)|m\rangle \quad (2.1)$$

where $\rho(\mathbf{k}_1, t)$ and $\rho(\mathbf{k}_2, 0)$ are the density operators that describe the system immediately after the emissions of γ_1 and γ_2, respectively; m and m' are the sub-levels for the intermediate state.

Since the intermediate level has a finite lifetime, the presence of perturbations, i.e. EFGs, can affect the angular correlation between successive radiations. The interaction between the probe nucleus and the local EFG occurs during the lifetime t of the intermediate state, and it is described by the interaction Hamiltonian $K(t)$. The time evolution operator of the system is given as

$$\Lambda(t) = \exp\left(-\frac{1}{\hbar}\int_0^t K(t')dt'\right) \tag{2.2}$$

The matrix elements of the first term in the right-hand side of (2.1) can be expressed as

$$\langle m|\rho(\mathbf{k}_1,t)|m'\rangle = \sum_{\substack{m_b m_{b'} \\ m_a m_{a'}}} \langle m_b|\rho(\mathbf{k}_1,0)|m_{b'}\rangle\langle m_b m_{b'}|G(t)|m_a m_{a'}\rangle \tag{2.3}$$

where

$$\langle m_b m_{b'}|G(t)|m_a m_{a'}\rangle = \langle m_a|\Lambda(t)|m_b\rangle\langle m_{b'}|\Lambda(t)|m_{a'}\rangle \tag{2.4}$$

and

$$\rho(\mathbf{k}_1,t) = \Lambda(t)\rho(\mathbf{k}_1,0)\Lambda^+(t) \tag{2.5}$$

In (2.3) and (2.4), m_a, $m_{a'}$ define the sublevels in the intermediate state immediately after the emission of γ_1, and m_b, $m_{b'}$ the sublevels immediately before the emission of γ_2. $G(t)$ is the perturbation factor.

If polarization of the radiations is not observed, the matrix elements of $\rho(\mathbf{k}_1,t)$ and $\rho(\mathbf{k}_2,0)$ are given by

$$\langle m|\rho(\mathbf{k}_1,0)|m'\rangle = \sum_{k_1 N_1}(-1)^{2I-I_i+m}A_{k_1}(\gamma_1)\begin{pmatrix} I & I & k_1 \\ m' & -m & N_1\end{pmatrix}\sqrt{4\pi}Y_{k_1}^{N_1}(\theta_1,\phi_1) \tag{2.6}$$

$$\langle m|\rho(\mathbf{k}_2,0)|m'\rangle = \sum_{k_2N_2}(-1)^{2I-I_f+m}A_{k_2}(\gamma_2)\begin{pmatrix} I & I & k_2 \\ m' & -m & N_2 \end{pmatrix}\sqrt{4\pi}Y_{k_2}^{N_2}(\theta_2,\phi_2) \tag{2.7}$$

The terms $\begin{pmatrix} I & I & k_1 \\ m' & -m & N_1 \end{pmatrix}$ and $\begin{pmatrix} I & I & k_2 \\ m' & -m & N_2 \end{pmatrix}$ are the Wigner 3-j symbols, and $Y_{k_i}^{N_i}$ are spherical harmonics.

Combining equations (2.1) and (2.3), and using equations (2.6) and (2.7) gives

$$W(\mathbf{k}_1,\mathbf{k}_2,t) = \sum_{\substack{k_1k_2\\N_1N_2}} \frac{A_{k_1}(\gamma_1)A_{k_2}(\gamma_2)}{\sqrt{(2k_1+1)(2k_2+1)}}G_{k_1k_2}^{N_1N_2}(t)Y_{k_1}^{N_1}(\theta_1,\phi_1)Y_{k_2}^{*N_2}(\theta_2,\phi_2) \tag{2.8}$$

The perturbation factor $G_{k_1k_2}^{N_1N_2}(t)$ is defined as

$$\begin{aligned} G_{k_1k_2}^{N_1N_2}(t) = &\sum_{\substack{m_am_{a'}\\m_bm_{b'}}}(-1)^{2I-m_a+m_b}\sqrt{(2k_1+1)(2k_2+1)} \\ &\times \begin{pmatrix} I & I & k_1 \\ m' & -m & N_1 \end{pmatrix}\begin{pmatrix} I & I & k_2 \\ m' & -m & N_2 \end{pmatrix}\langle m_a|\Lambda(t)|m_b\rangle\langle m_{b'}|\Lambda(t)|m_{a'}\rangle \end{aligned} \tag{2.9}$$

Equation (2.8) expresses the angular correlation in its most general way when the polarization of the radiations is not considered. The perturbation factor, given by equation (2.9), contains all the information about the interaction between the probe nuclei and the external EFG. Note that in equation (2.9) the summation is carried over all sublevel transitions. Also, the Wigner 3-j symbols give the amplitude of the coupling of the angular momentum of the nucleus and the local EFG.

$A_{k_1}(\gamma_1) = A_{k_1}(L_1L_1'I_iI)$ and $A_{k_2}(\gamma_2) = A_{k_2}(L_2L_2'I_fI)$ are factors known as the anisotropies of the angular correlation, and they depend only on the spins of the nuclear states, I, I_i and I_f involved in the transition and on the multipolarities of the emitted radiations, L.

One can say that, classically, the perturbation exists because the torque exerted by the local EFG on the probe nucleus causes it to precess about the axis of symmetry of the EFG with a given precession frequency. The precessional motion of the nucleus will reorient it in space, and, in turn, alter the angular correlation of the emitted radiations. Fig 2.5 illustrates the classical interpretation of the perturbation on the angular correlation. This view does not correspond to what is really happening quantum mechanically, but it is useful in helping to visualize the interaction between the nucleus and the EFG. The changes observed in the angular correlation are a consequence of the redistribution in the m-state populations caused by transitions in the probe nucleus as a result of its interaction with the local EFG.

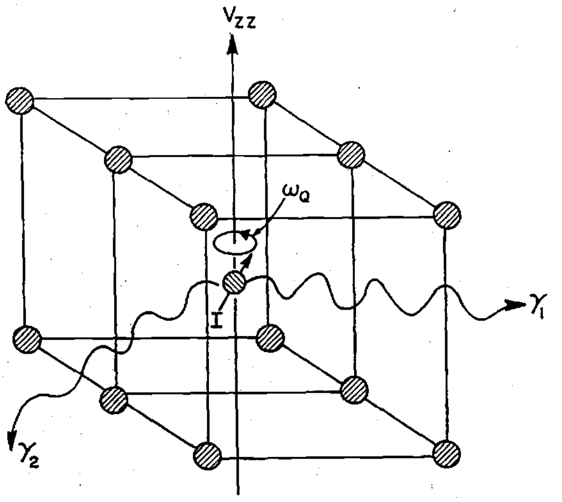

Figure 2.5: Classical interpretation of the perturbed angular correlation. The nuclear spin I precesses about the V_{zz} axis with precession frequency ω_Q.

2.2 ANGULAR CORRELATION OF FREE NUCLEI

If the sum of all perturbations is equal to zero, as is the case if the probe nucleus is in material whose lattice has cubic symmetry and is defect-free, the interaction Hamiltonian $K(t) = 0$, and $\Lambda(t) = 1$.

Equation (2.4) becomes

$$\langle m_a|\Lambda(t)|m_b\rangle\langle m_{b'}|\Lambda(t)|m_{a'}\rangle = \delta_{m_a m_b}\delta_{m_{a'} m_{b'}} \tag{2.10}$$

Introducing this result in equation (2.9), and using the orthogonality relation for the 3-j symbols

$$\sum_{mm'} = \begin{pmatrix} I & I & k_1 \\ m' & -m & N_1 \end{pmatrix}\begin{pmatrix} I & I & k_2 \\ m' & -m & N_2 \end{pmatrix} = (2k_1+1)^{-1}\delta_{k_1 k_2}\delta_{N_1 n_2} \tag{2.11}$$

the perturbation factor is then given by

$$G_{k_1 k_2}^{N_1 N_2}(t) = \delta_{k_1 k_2}\delta_{N_1 n_2} \tag{2.12}$$

Using the addition theorem for spherical harmonics

$$P_k(\cos\theta) = \frac{4\pi}{2k+1}\sum_{N=-k}^{k} Y_k^{*N}(\theta_1\phi_1)Y_k^N(\theta_2\phi_2) \tag{2.13}$$

and inserting equation (2.12) into equation (2.8), and carrying out the summation over N_1 and N_2, one obtains the unperturbed form of the angular correlation function

$$W(\mathbf{k}_1,\mathbf{k}_2) = \sum_{k=0,even}^{k_{max}} A_k(\gamma_1)A_k(\gamma_2)P_k(\cos\theta) = \sum_{k=0,even}^{k_{max}} A_{kk}P_k(\cos\theta) \tag{2.14}$$

$P_k(\cos\theta)$ are the Legendre polynomials,θ is the angle between the radiations γ_1 and γ_2, and $A_{kk} = A_k(\gamma_1)A_k(\gamma_2)$. The summation in equation (2.14) contains only even values because it is assumed that the polarization of the radiations is not observed, and $k_{max} = MIN(2I, L_1 + L_1', L_2 + L_2')$. The probe nuclei ^{181}Ta and ^{111}Cd have spin of the intermediate state $I = 5/2$, which gives $k_{max} = 4$. The cascade decay depends only on nuclear transition parameters, given by the A_{kk} parameters. The Legendre polynomial term gives the connection between successive radiations in the cascade decay.

2.3 EFFECT OF STATIC EFGS ON THE ANGULAR CORRELATION FUNCTION

If the EFG at the probe site stays constant during the lifetime of the intermediate state, the interaction Hamiltonian, K will be time independent, and the time evolution operator is given by

$$\Lambda(t) = \exp\left(-\frac{i}{\hbar}Kt\right) \tag{2.15}$$

To diagonalize the interaction Hamiltonian, K, a unitary matrix is used:

$$UKU^{-1} = E \tag{2.16}$$

where E is the diagonal energy matrix with energy eigenvalues E_n.

Combining (2.16) and (2.15), and expanding the result in a power series, it can be shown that time evolution operator is given by

$$\Lambda(t) = U^{-1}\exp\left(-\frac{i}{\hbar}Et\right)U \tag{2.17}$$

The matrix elements of $\Lambda(t)$ are

$$\langle m_a|\Lambda(t)|m_b\rangle = \sum_n \langle m_a|n\rangle\langle n|m_b\rangle \exp\left(-\frac{i}{\hbar}E_n t\right) \tag{2.18}$$

Using this result, the matrix elements of $G(t)$ (see (2.4)) become

$$\langle m_b m_{b'}|G(t)|m_a m_{a'}\rangle = \sum_{nn'} \langle m_a|n\rangle\langle m_{a'}|n'\rangle^*\langle m_b|n\rangle^*\langle m_{b'}|n'\rangle \exp\left(-i\frac{E_n - E_{n'}}{\hbar}t\right) \tag{2.19}$$

and the perturbation factor can be written as

$$G_{k_1k_2}^{N_1N_2}(t) = \sum_{\substack{m_a m_{a'} \\ m_b m_{b'}}} \sum_{nn'} (-1)^{2I-m_a+m_b}\sqrt{(2k_1+1)(2k_2+1)} \begin{pmatrix} I & I & k_1 \\ m' & -m & N_1 \end{pmatrix} \times \begin{pmatrix} I & I & k_2 \\ m' & -m & N_2 \end{pmatrix} \langle m_a|n\rangle\langle m_{a'}|n'\rangle^*\langle m_b|n\rangle^*\langle m_{b'}|n'\rangle \exp\left(-i\frac{E_n - E_{n'}}{\hbar}t\right) \tag{2.20}$$

Analytical expressions for $G_{k_1k_2}^{N_1N_2}(t)$ for various values of I for static interactions can be found in [12].

If the EFG is axially symmetric, the quantization axis can be chosen to coincide with the axis of the symmetry. In this situation, K and $\Lambda(t)$ become diagonal, and the perturbation function is given by

$$G_{k_1k_2}^{N_1N_2}(t) = \sum_{nn'} (-1)^{2I-m_a+m_b}\sqrt{(2k_1+1)(2k_2+1)} \begin{pmatrix} I & I & k_1 \\ m' & -m & N_1 \end{pmatrix} \times \begin{pmatrix} I & I & k_2 \\ m' & -m & N_2 \end{pmatrix} \exp\left(-i\frac{E_n - E_{n'}}{\hbar}t\right) \tag{2.21}$$

If any of the radiations is emitted parallel to the symmetry axis of the perturbing field, the corresponding spherical harmonic Y_l^m in equation (2.9) becomes

$$Y_k^N = \delta_{N0}\left(\frac{2k_i+1}{4\pi}\right)^{1/2} \tag{2.22}$$

Using the sum rule of the 3-j symbols in (2.32) gives $n' - n + N = 0$; all terms $n \neq n'$ vanish and the perturbation function becomes

$$G_{k_1 k_2}^{N_1 N_2}(t) = \delta_{k_1 k_2} \tag{2.23}$$

which shows that in this situation the angular correlation is not perturbed.

Commonly, powder samples are used in PAC experiments. These samples can be seen as a collection of a large number of microcrystals randomly oriented in space. In order to find the perturbation function, it is necessary to average equation (2.20) over all possible spatial orientations of the microcrystals. $D(\Omega)$ is the rotation matrix that transforms the interaction Hamiltonian $K(\mathbf{z})$ from the lab coordinate system $\mathbf{z}$ to the principal axes system of a single microcrystal $\mathbf{z}'$ through a set of Euler angles $\Omega = (\phi, \theta, \gamma)$

$$K(\mathbf{z}') = D(\Omega) K(\mathbf{z}) D^{-1}(\Omega) \tag{2.24}$$

Using the operator U to diagonalize $K(\mathbf{z}')$, the time evolution operator is

$$\Lambda(t) = D^{-1}(\Omega) U^{-1} \exp\left(-\frac{i}{\hbar} E t\right) U D(\Omega) \tag{2.25}$$

and the matrix elements of $\Lambda(t)$ are

$$\langle m_a | \Lambda | m_b \rangle = \sum_{m_1 m_2 n} \langle n | m_1 \rangle \langle n | m_2 \rangle^* \exp\left(-\frac{i}{\hbar} E t\right) D^{I*}_{m_1 m_a}(\Omega) D^{I}_{m_2 m_b}(\Omega) \tag{2.26}$$

where the terms

$$D^{I}_{m_1 m_i}(\Omega) = \langle m_1 | D(\Omega) | m_i \rangle \tag{2.27}$$

are the matrix elements for the rotation operator.

With (2.26) the matrix elements of $G(t)$ are

$$\langle m_b m_{b'} | G(t) | m_a m_{a'} \rangle = \sum_{\substack{m_1 m_{1'} \\ m_2 m_{2'}}} \sum_{n n'} \langle n | m_1 \rangle \langle n' | m_1 \rangle^* \langle n | m_2 \rangle^* \langle n' | m_{2'} \rangle$$
$$\times \exp\left(-\frac{E_n - E_{n'}}{\hbar} t\right) D^{I*}_{m_1 m_a}(\Omega) D^{I}_{m_{1'} m_{a'}}(\Omega) D^{I*}_{m_2 m_a}(\Omega) D^{I}_{m_{2'} m_{b'}}(\Omega) \tag{2.28}$$

Combining (2.26) and (2.9), and the contraction relation for the 3-j symbols:

$$\begin{pmatrix} j_1 & j_2 & j \\ m_1' & m_2' & m' \end{pmatrix} D^{j}_{mm'} = \sum_{m_1 m_2} \begin{pmatrix} j_1 & j_2 & j \\ m_1 & m_2 & m \end{pmatrix} D^{j_1}_{m_1 m_1'} D^{j_2}_{m_2 m_2'} \qquad (2.29)$$

and after the summation over $m_a m_a'$ and $m_b m_b'$ is performed, the perturbation is

$$G^{N_1 N_2}_{k_1 k_2}(t) = \sum_{\substack{m_1 m_2 \\ m_1' m_2'}} \sum_{nn'} (-1)^{2I+m_1+m_2} [(2k_1+1)(2k_2+1)]^{\frac{1}{2}} \exp\left(-i\frac{E_n - E_{n'}}{\hbar}\right)$$
$$\times \begin{pmatrix} I & I & k_1 \\ m_1' & -m_1 & p_1 \end{pmatrix} \begin{pmatrix} I & I & k_2 \\ m_2' & -m_2 & p_2 \end{pmatrix} D^{k_1 *}_{p_1 N_1}(\Omega) D^{k_2}_{p_2 N_2}(\Omega)$$
$$\times \langle n|m_1\rangle \langle n'|m_1\rangle^* \langle n|m_2\rangle \langle n'|m_{2'}\rangle^* \qquad (2.30)$$

With the orthonormality of the rotation matrices given by

$$\int D^{j_1 *}_{m_1 m_1}(\Omega) D^{j_2}_{m_2 m_2}(\Omega) d\Omega = \frac{1}{2j+1} \delta_{j_1 j_2} \delta_{m_1 m_2} \delta_{m_1' m_2'} \qquad (2.31)$$

it is possible to average (2.30) over all possible orientations of the microcrystals in the powder sample. The result is

$$G_{k_1 k_2}(t) = \delta_{k_1 k_2} \delta_{N_1 N_2} \delta_{p_1 p_2} \sum_{nn'} S^{k_1 k_2}_{nn'} \exp\left(-i\frac{E_n - E_{n'}}{\hbar} t\right) \qquad (2.32)$$

The $S^{k_1 k_2}_{nn'}$ coefficients are defined by:

$$S^{k_1 k_2}_{nn'} = \sum_{\substack{m_1 m_2 \\ m_1' m_2'}} (-1)^{2I+m_1+m_2} \begin{pmatrix} I & I & k_1 \\ m_1' & -m_1 & p \end{pmatrix} \begin{pmatrix} I & I & k_2 \\ m_2' & -m_2 & p \end{pmatrix}$$
$$\times \langle n|m_1\rangle^* \langle n'|m_1\rangle \langle n|m_2\rangle \langle n'|m_{2'}\rangle^* \qquad (2.33)$$

The selection rules of the 3-j symbols require $m_1' - m_1 + p = 0$ and $m_2' - m_2 + p = 0$. The sums over m_1, m_1' and m_2, m_2' can therefore be replaced by a sum over p. Inserting (2.33) in (2.32) gives

$$G_{kk}(t) = \sum_{\substack{m_1 m_2 \\ m_1' m_2'}} \sum_{nn'} (-1)^{2I+m_1+m_2} \begin{pmatrix} I & I & k_1 \\ m_1' & -m_1 & p \end{pmatrix} \begin{pmatrix} I & I & k_2 \\ m_2' & -m_2 & p \end{pmatrix} \times \exp\left(-i\frac{E_n - E_{n'}}{\hbar}t\right) \langle n|m_1\rangle^* \langle n'|m_1\rangle \langle n|m_2\rangle \langle n'|m_{2'}\rangle^* \quad (2.34)$$

The comparison of (2.34) with (2.20) shows that the perturbation function for a powder sample is the average of the perturbation function of a single crystal

$$G_{kk}(t) = \frac{1}{2k+1} \sum_p G_{kk}^{pp}(t) \quad (2.35)$$

Rearranging (2.32) gives the perturbation function for a powder

$$G_{kk}(t) = \sum_n S_{nn}^{kk} + \sum_{n \neq n'} S_{nn}^{kk} \cos\left(\frac{(E_n - E_n')}{\hbar}t\right) \quad (2.36)$$

Inserting this equation in (2.8) and summing over N_1, N_2 and applying the addition theorem for the spherical harmonics gives a the angular correlation function for a powder

$$W(\theta, t) = \sum_{k=0,even}^{k_{max}} A_{kk} G_{kk}(t) P_k(\cos\theta) \quad (2.37)$$

The term $\sum S_{nn'}^{kk}$ is independent of time; it is known as the hard core term. This term shows that the angular correlation of a powder is never completely wiped out by static fields of any kind. Its origin is due to the fact that a powder sample with a very large number of microcrystals has a number of these microcrystals aligned with the direction of propagation of one of the γ

rays emitted by the probe nuclei. According to the result given by (2.23), in this situation, the angular correlation is not perturbed.

For $I = 5/2$, $k_{max} = 4$ and (2.37) is given by

$$W(\theta, t) = 1 + A_{22}G_{22}(t)P_2(\cos\theta) + A_{44}G_{44}(t)P_4(\cos\theta) \qquad (2.38)$$

The A_{kk}s are normalized so that $A_{00} = 1$.

2.4 THE STATIC QUADRUPOLE INTERACTION

After obtaining an expression for the angular correlation function, it is now necessary to calculate the perturbation factor. The perturbation results from the interaction of the electric quadrupole moment of the probe nucle with the local EFG. Nuclei that have non-spherically symmetric charge distributions possess quadrupole moments (see Fig. 2.6).

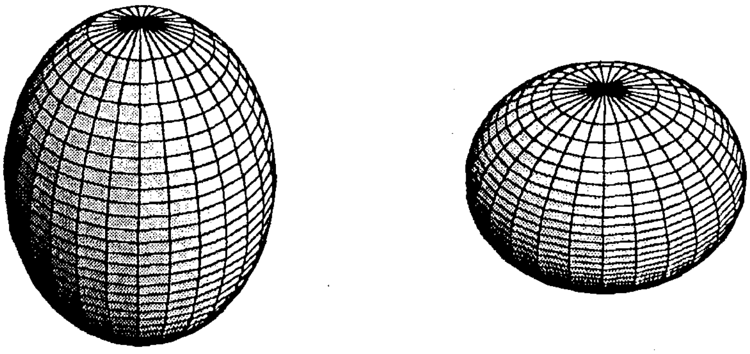

Figure 2.6: Shape of charge distribution in a nucleus. A positive quadrupole moment corresponds to a prolate (left) charge distribution. A negative quadrupole moment corresponds to an oblate charge distribution [7].

The energy of interaction of the nuclear charge distribution $\rho(\mathbf{r})$ and the extranuclear field potential $\Phi(\mathbf{r})$ is

$$E_e = \int \rho(\mathbf{r})\Phi(\mathbf{r})d\mathbf{r} \tag{2.39}$$

Expanding the potential in a Taylor series about $\mathbf{r} = 0$ gives

$$\Phi(\mathbf{r}) = \Phi(0) + \sum_{i=1}^{3} \left(\frac{\partial\Phi}{\partial x_i}\right)_0 + \frac{1}{2}\sum_{i,j=1}^{3}\left(\frac{\partial^2\Phi}{\partial_i\partial_j}\right) x_i x_j + \ldots \tag{2.40}$$

The interaction energy can then be written as

$$E_E = E^{(0)} + E^{(1)} + E^{(2)} + \ldots \tag{2.41}$$

where

$$E^{(0)} = \Phi_0 \int \rho(\mathbf{r})d\mathbf{r} \tag{2.42}$$

$$E^{(1)} = \sum_{i=1}^{3}\left(\frac{\partial\Phi}{\partial x_i}\right)_0 \int \rho(\mathbf{r})x_i d\mathbf{r} \tag{2.43}$$

$$E^{(2)} = \frac{1}{2}\sum_{i,j=1}^{3}\left(\frac{\partial^2\Phi}{\partial_i\partial_j}\right) x_i x_j \int \rho(\mathbf{r})x_i x_j d\mathbf{r} \tag{2.44}$$

The term $E^{(0)}$ corresponds to the energy contribution of a point charge distribution; and it is a constant. The term $E^{(1)}$ describes the energy of interaction between the dipole moment and the electric field at the center of the nucleus. This term does not contribute because the expectation value of the dipole moment is zero. The only important term in the expansion is $E^{(2)}$. This term is a 3×3 symmetric matrix that can be diagonalized into a principal axis system. The diagonalization yields

$$E^{(2)} = \frac{1}{2}\sum_i \Phi_{ii}\int \rho(\mathbf{r})x_i^2 d\mathbf{r} = \frac{1}{6}\sum_i \Phi_{ii}\int \rho(\mathbf{r})r_i^2 d\mathbf{r} + \frac{1}{2}\sum_i \Phi_{ii}\int \rho(\mathbf{r})\left(x_i^2 - \frac{r^2}{3}\right)d\mathbf{r} \tag{2.45}$$

where

$$\Phi_{ii} = \frac{\partial^2 \phi}{\partial x_i^2} \tag{2.46}$$

Since the potential obeys the Poisson equation, at the center of the nucleus, the potential can be expressed as

$$\left(\nabla^2 \Phi\right)_0 = \sum_i \Phi_{ii} = \frac{e}{\epsilon_0} |\psi(0)|^2 \tag{2.47}$$

where $|\psi(0)|^2$ is the probability density of the electron wave function at the center of the nucleus. Inserting (2.47) into (2.45) gives

$$E^{(2)} = E_M + E_Q \tag{2.48}$$

where

$$E_M = \frac{e}{6\epsilon_0} |\psi(0)|^2 \int \rho(\mathbf{r}) d\mathbf{r} \tag{2.49}$$

and

$$E_Q = \frac{1}{2} \sum_i \Phi_{ii} \int \rho(\mathbf{r}) \left(x_i^2 - \frac{r^2}{3} \right) d\mathbf{r} \tag{2.50}$$

E_M is the monopole term and can be written as

$$E_M = \frac{Ze^2}{6\epsilon_0} |\psi(0)|^2 \langle r^2 \rangle \tag{2.51}$$

The monopole term depends only on the mean square of the nuclear radius; it does not depend on the nuclear orientation and does not contribute to the interaction between the nucleus and the external EFG. E_Q, the quadrupole term, does depend on the nuclear orientation and is the source of the quadrupole interaction. By defining the tensors

$$Q_{ii} = \frac{1}{e} \int \rho(\mathbf{r}) \left(x_i^2 - \frac{r^2}{3} \right) d\mathbf{r} \tag{2.52}$$

and

$$\Phi_{ii} = V_{ii} + \frac{1}{3} \left(\nabla^2 \Phi\right) \delta_{ii} \tag{2.53}$$

the quadrupole term can be written as

$$E_Q = \frac{e}{6}\sum_i V_{ii}Q_{ii} \tag{2.54}$$

Note that V_{ii} is a traceless matrix and that $\frac{1}{3}\left(\nabla^2\right)\delta_{ii}$ does not contribute since $\sum_i Q_{ii} = 0$. V_{ii} is the tensor that describes the EFG, and only charges not localized in the nucleus contribute to V_{ii}.

Since $\sum_i V_{ii} = 0$, the EFG can be completely defined by two parameters. By choosing a principal axis system, one can have $|V_{zz}| \geq V_{yy}| \geq V_{xx}|$. One of these parameter is V_{zz}, the other is the asymmetry parameter η defined as

$$\eta = \frac{V_{yy} - V_{xx}}{V_{zz}}, \qquad 0 \geq \eta \geq 1 \tag{2.55}$$

To calculate E_Q, it is easier to express Q_{ii} and V_{ii} as spherical tensors. The components of the EFG are

$$\begin{aligned} V_{20} &= \frac{1}{4}\sqrt{\frac{5}{\pi}}V_{zz} \\ V_{2\pm1} &= \pm\frac{1}{2}\sqrt{\frac{5}{6\pi}}\left(V_{xz} \pm V_{yz}\right) \\ V_{2\pm2} &= \pm\frac{1}{4}\sqrt{\frac{5}{6\pi}}\left(V_{xx} - V_{yy} \pm 2iV_{xy}\right) \end{aligned} \tag{2.56}$$

A principal axis transformation yields

$$\begin{aligned} V_{20} &= \frac{1}{4}\sqrt{\frac{5}{\pi}}V_{zz} \\ V_{2\pm1} &= 0 \\ V_{2\pm2} &= \pm\frac{1}{4}\sqrt{\frac{5}{6\pi}}\left(V_{xx} - V_{yy}\right) = \mp\frac{1}{4}\sqrt{\frac{5}{6\pi}}\eta V_{zz} \end{aligned} \tag{2.57}$$

The classical electric quadrupole moment is

$$Q = \frac{1}{e}\sqrt{\frac{16\pi}{5}}\int \rho(\mathbf{r})Y_2^0 d\mathbf{r} \tag{2.58}$$

In quantum mechanics Q is defined as the expectation value of the quadrupole operator

$$Q = \frac{1}{e}\sqrt{\frac{16\pi}{5}}\langle Im|r^2Y_2^0|Im\rangle \tag{2.59}$$

By the Wigner-Eckart theorem

$$\langle Im|Q_{20}|Im\rangle = (-1)^{I-m}\begin{pmatrix} I & 2 & I \\ -m & 0 & m \end{pmatrix}\langle I|Q_2|I\rangle \tag{2.60}$$

In this way it is possible to define the electric quadrupole moment as

$$Q_{2q} = r^2Y_2^q \tag{2.61}$$

and the quadrupole energy is expressed as

$$E_Q = \frac{4\pi}{5}\sum_q(-1)^q eQ_{2q}V_{2-q} \tag{2.62}$$

In the quantum formalism (2.62) the electric quadrupole energy is the expectation value of the quadrupole interaction and Q_{2q} is the operator operating on the nuclear states

$$E_Q = \langle Im|H_Q|Im'\rangle = \frac{4\pi}{5}\sum_{q=-2}^{2}(-1)^q\langle Im|Q_{2q}|Im'\rangle V_{2-q} \tag{2.63}$$

When calculating the energy eigenvalues, it is interesting to consider the cases where $\eta = 0$ and where $\eta > 0$.

For the axial symmetry case ($\eta = 0$), applying the condition $V_{xx} = V_{yy}$ to (2.62) yields

$$E_Q = \langle Im|H_Q|Im\rangle = \sqrt{\frac{\pi}{5}}eV_{zz}\langle Im|Q_{20}|Im\rangle \tag{2.64}$$

With the definition of Q

$$Q = 4\sqrt{\pi 5}\langle II|Q_{20}|II\rangle = 4\sqrt{\pi 5}\begin{pmatrix} I & 2 & I \\ -I & 0 & I \end{pmatrix}\langle I|Q_2|I\rangle \tag{2.65}$$

and substituting (2.60) into (2.64) gives

$$E_Q = \frac{1}{4}V_{zz}(-1)^{I-m}\frac{\begin{pmatrix} I & 2 & I \\ -m & 0 & m \end{pmatrix}}{\begin{pmatrix} I & 2 & I \\ -I & 0 & I \end{pmatrix}}eQ = V_{zz}\frac{3m^2 - I(I+1)}{4I(2I-1)})eQ \tag{2.66}$$

The transition energies between two sublevels m and m' are given by

$$E_Q(m) - E_Q(m') = \frac{eQV_{zz}}{4I(2I-1)} = 3(m - m'^2)\hbar\omega_Q \tag{2.67}$$

where

$$\omega_Q = \frac{eQV_{zz}}{4I(2I-1)\hbar} \tag{2.68}$$

is the quadrupole frequency.

In (2.67) the term $(m^2 - m'^2)$ is always an integer and, as a consequence, the transition frequencies are integer multiples of the lowest transition frequency: $\omega_Q^0 = 6\omega_Q$ for half-integer I, and $\omega_Q^0 = 3\omega_Q$ for integer I.

For $I = 5/2$, the transition energies are

$$\begin{aligned} E_Q(m = \pm 1/2) &= -\frac{1}{5}eQV_{zz} \\ E_Q(m = \pm 3/2) &= -\frac{1}{20}eQV_{zz} \\ E_Q(m = \pm 5/2) &= \frac{1}{4}eQV_{zz} \end{aligned} \tag{2.69}$$

and the PAC transition frequencies are

$$\begin{aligned} \omega_1 &= \frac{E_Q(\pm 3/2) - E_Q(\pm 1/2)}{\hbar} = 6\omega_Q \\ \omega_2 &= \frac{E_Q(\pm 5/2) - E_Q(\pm 3/2)}{\hbar} = 12\omega_Q \\ \omega_3 &= \omega_1 + \omega_2 = 18\omega_Q \end{aligned} \tag{2.70}$$

Fig. 2.7 shows the energy splitting for an $I = 5/2$ nuclear level and the PAC transition frequencies.

Using (2.67), the perturbation function for a powder sample (2.36) becomes

$$G_{kk}(t) = \sum_{m} S^{kk}_{mm} + \sum_{m \neq m'} S^{kk}_{mm'} \cos[3\omega_Q(m^2 - m'^2)t] \tag{2.71}$$

Equation (2.71) can be further simplified by introducing an index $n = |m_2 - m'^2|/2$, for half-integer I, or $n = |m^2 - m'^2|$, for integer I, and by defining

$$S_{kn} = \sum_{mm'} S^{kk}_{mm'} = \sum_{mm'} \begin{pmatrix} I & I & k \\ m' & -m & p \end{pmatrix}^2 \tag{2.72}$$

The result is

$$G_{kk}(t) = S_{k0} + \sum_{n>0} S_{kn} \cos(n\omega^0_Q t) \tag{2.73}$$

The S_{kn} are normalized so that $\sum_n S_{kn} = 1$, and $G_{kk}(0) = 1$. The meaning of (2.73) is that the perturbation function rotates with frequencies $n\omega^0_Q$ and that each frequency is weighted by the amplitudes S_{kn}.

If the interaction Hamiltonian is not axially symmetric, it has to be diagonalized to find the energy eigenvalues. Although this is difficult for non-axial symmetries, it is still possible to express the matrix elements of the Hamiltonian for the general case as

$$\begin{aligned} H_{m,m} &= \hbar\omega_Q[3m^2 - (I(I-1)] \\ H_{m,m\pm1} &= 0 \\ H_{m,m\pm2} &= \hbar\omega_Q\eta[(I \mp m - 1)(I \pm m + 1)(I \pm m + 2)]^{\frac{1}{2}} \end{aligned} \tag{2.74}$$

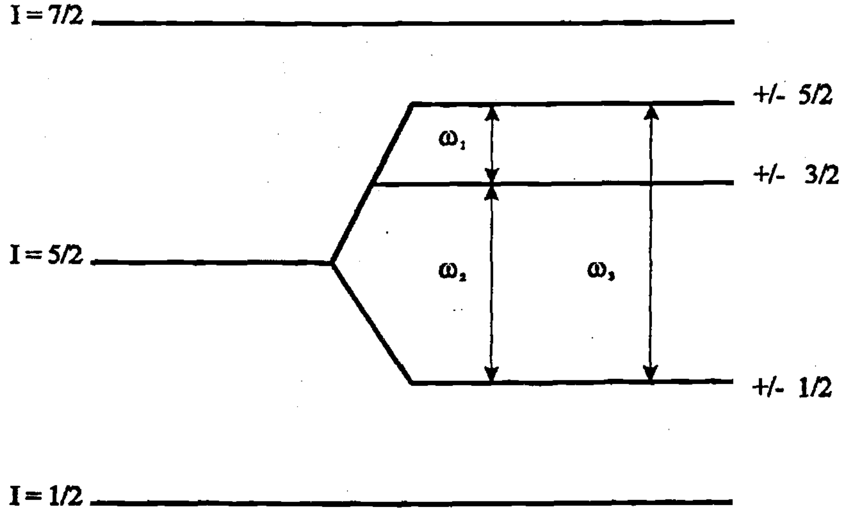

Figure 2.7: The electric quadrupole splitting of the intermediate state $I = 5/2$.

The probe nuclei ^{181}Ta and ^{111}Cd have the spin of the intermediate state $I = 5/2$. In this situation the Hamiltonian matrix as a function of η is

$$H_Q = \hbar\omega_Q \begin{pmatrix} 10 & 0 & \eta\sqrt{10} & 0 & 0 & 0 \\ 0 & -2 & 0 & 3\eta\sqrt{2} & 0 & 0 \\ \eta\sqrt{10} & 0 & -8 & 0 & 3\eta\sqrt{2} & 0 \\ 0 & 3\eta\sqrt{2} & 0 & -8 & 0 & \eta\sqrt{10} \\ 0 & 0 & 3\eta\sqrt{2} & 0 & -2 & 0 \\ 0 & 0 & 0 & \eta\sqrt{10} & 0 & 10 \end{pmatrix} \tag{2.75}$$

The secular equation for the quadrupole Hamiltonian is

$$E^3 - 28E(\eta^2 + 3)(\hbar\omega_Q)^2 - 160(1 - \eta^2)(\hbar\omega_Q)^3 = 0 \tag{2.76}$$

and the eigenvalues are [13]

$$\begin{aligned} E_{\pm 5/2} &= 2\alpha\hbar\omega_Q \cos\left[\frac{1}{3}\cos^{-1}\beta\right] \\ E_{\pm 3/2} &= -2\alpha\hbar\omega_Q \cos\left[\frac{1}{3}(\pi + \cos^{-1}\beta)\right] \\ E_{\pm 1/2} &= -2\alpha\hbar\omega_Q \cos\left[\frac{1}{3}(\pi - \cos^{-1}\beta)\right] \end{aligned} \tag{2.77}$$

where

$$\alpha = \sqrt{\frac{28}{3}(\eta^2 + 3)} \tag{2.78}$$

$$\beta = \frac{80(1 - n^2)}{\alpha^3} \tag{2.79}$$

The transition frequencies are the differences between the energy levels (2.77).

$$\begin{aligned} \omega_1 &= \frac{E_{\pm 3/2} - E_{\pm 1/2}}{\hbar} = 2\sqrt{3}\omega_Q \sin\left[\frac{1}{3}\cos^{-1}\beta\right] \\ \omega_2 &= \frac{E_{\pm 5/2} - E_{\pm 3/2}}{\hbar} = 2\sqrt{3}\omega_Q \sin\left[\frac{1}{3}(\pi - \cos^{-1}\beta)\right] \\ \omega_3 &= \frac{E_{\pm 5/2} - E_{\pm 1/2}}{\hbar} = 2\sqrt{3}\omega_Q \sin\left[\frac{1}{3}(\pi + \cos^{-1}\beta)\right] \end{aligned} \tag{2.80}$$

where $\omega_3 = \omega_1 + \omega_2$. The energies of the levels and the PAC transition frequencies are dependent on η. Figure (2.4) shows the eigenvalues (2.77) and the frequencies (2.80) as a function of η.

Introducing again the index $n = |m^2 - m'^2|/2$ the expression for the perturbation function in a powder is

$$G_{kk} = S_{k0}(\eta) + \sum_{n=1}^{3} S_{kn}(\eta)\cos[\omega_n(\eta)t] \tag{2.81}$$

When $\eta > 0$ the S_{kn} coefficients are functions of the asymmetry parameter η [14]. These coefficients are tabulated in Table 2.1. As in the case $\eta = 0$, the S_{kn} are normalized so that $\sum_{n=0}^{3} S_{kn} = 1$.

For $I = 5/2$, the angular correlation function is

$$W(\theta, t) = 1 + A_{22}G_{22}(t)P_2(\cos\theta) + A_{44}G_{44}(t)P_4(\cos\theta) \tag{3.38}$$

The dependence of the perturbation function $G_{22}(t)$ on the asymmetry parameter η is shown in Fig. 2.9.

The probe nuclei in the interior of a material are under the influence of the EFGs generated by the material. There are four sources that can contribute to the total EFG at the probe nuclei [40, 15]:

(*i*) Ions and electrons from the crystalline lattice surrounding the probe.

(*ii*) Electrons in the probe atom located in unfilled atomic shells.

(*iii*) Electrons in filled electronic shells in the probe atom.

(*iv*) Defects in the lattice.

The contribution of the first source (*i*), although relatively important, has the same symmetry as the crystal where the probe nuclei are located, it only adds to the overall EFG of the material without changing its symmetry significantly.

In first approximation it is valid to consider that the contribution of the electrons from (*ii*) is not important if one assumes that electrons in filled atomic shells have a spherically symmetric distribution and therefore do not contribute to the EFG at a probe site. The other electrons in unfilled shells contribute to the EFG and reduce the EFG from the crystal due to their asymmetric distribution. It is estimated that this effect has a small importance on the total EFG at the probe site.

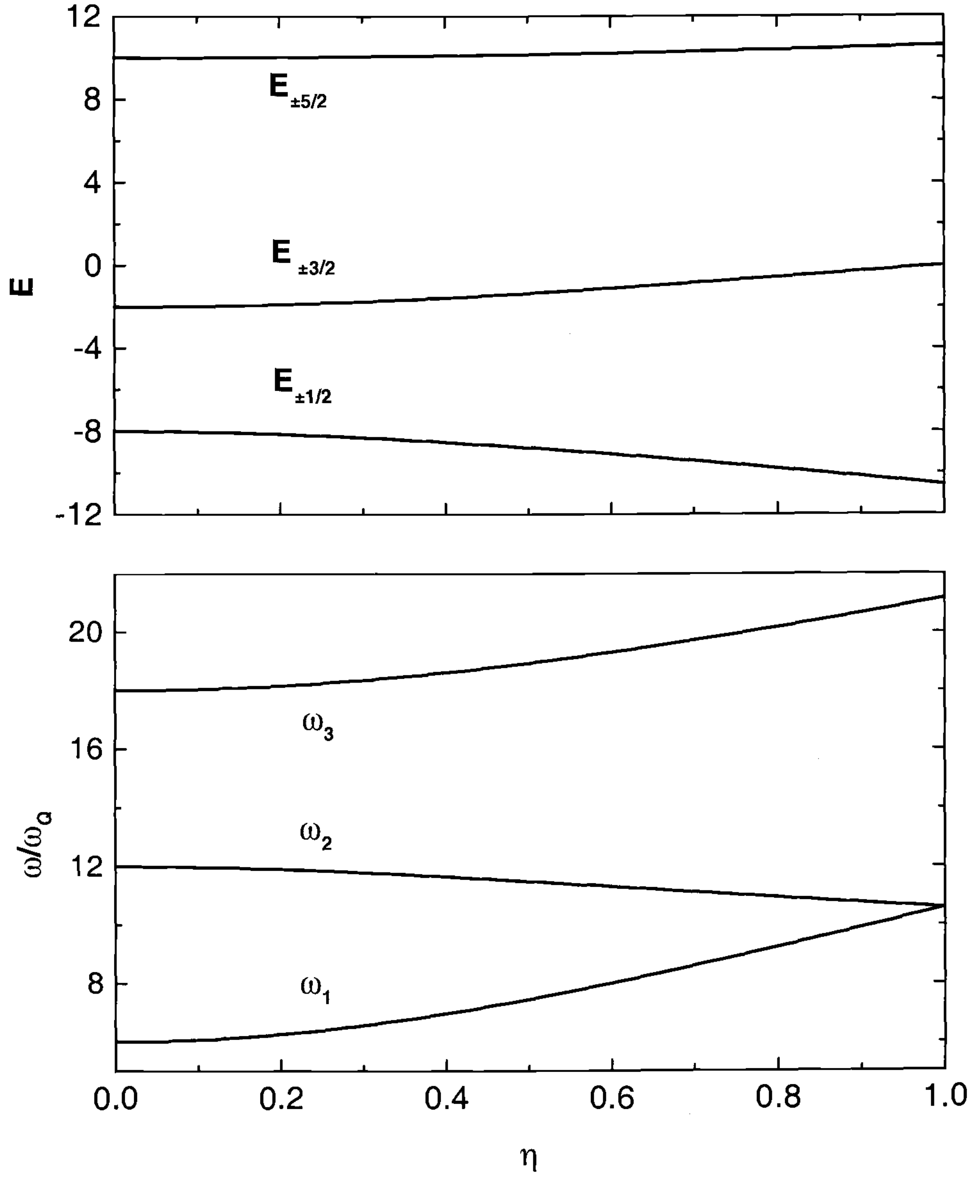

Figure 2.8: Eigenvalues (top) and PAC frequencies (bottom) for quadrupole interaction ($I = 5/2$) as a function of the asymmetry parameter η. Energies are given in units of $\hbar\omega_Q$.

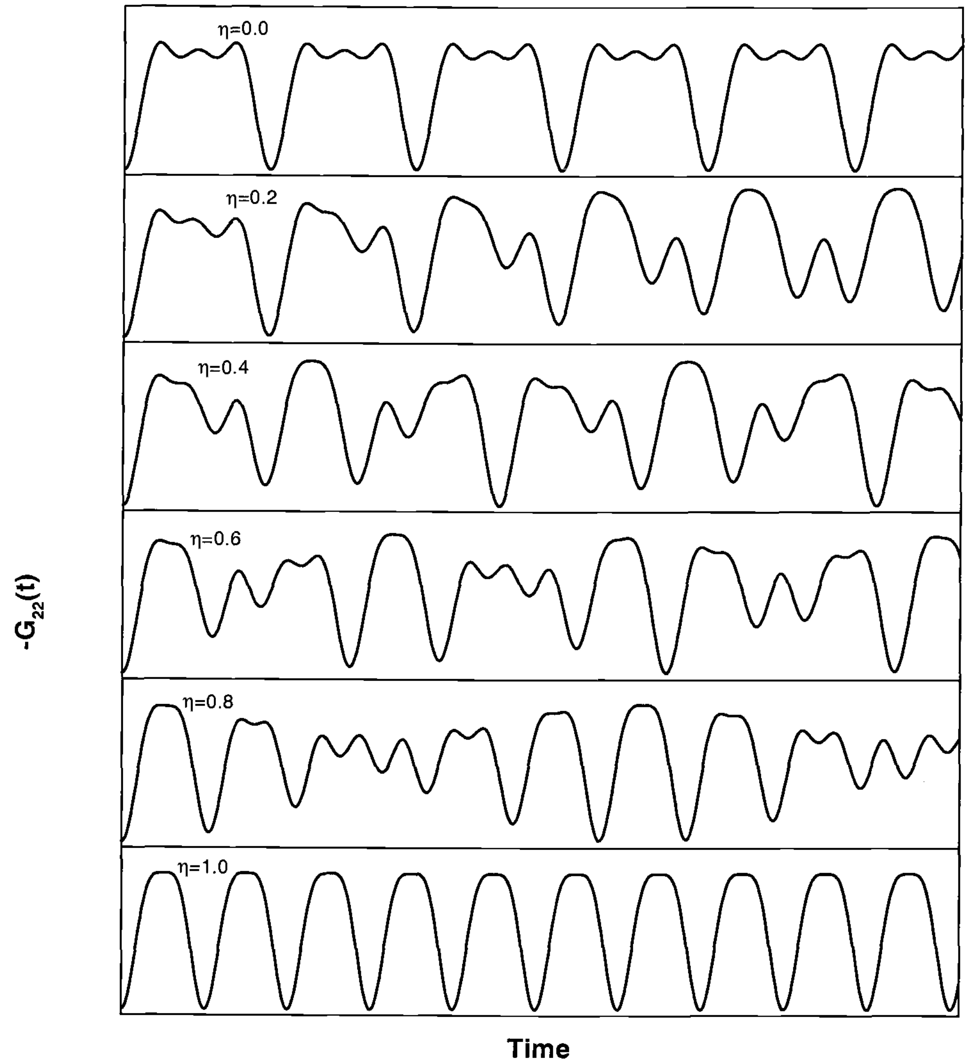

Figure 2.9: Perturbation function $G_{22}(t)$ for a static quadrupole interaction ($I = 5/2$) as a function of η.

η	S_{20}	S_{21}	S_{22}	S_{23}
	S_{20}	S_{21}	S_{22}	S_{23}
0.0	0.2000	0.3714	0.2857	0.1429
	0.1111	0.2381	0.2857	0.3651
0.1	0.2024	0.3688	0.2855	0.1432
	0.1098	0.2395	0.2858	0.3649
0.2	0.2090	0.3617	0.2850	0.1443
	0.1061	0.2435	0.2861	0.3643
0.3	0.2181	0.3517	0.2844	0.1458
	0.1010	0.2491	0.2864	0.3634
0.4	0.2280	0.3405	0.2840	0.1474
	0.0955	0.2553	0.2867	0.3625
0.5	0.2373	0.3296	0.2841	0.1490
	0.0904	0.2613	0.2866	0.3617
0.6	0.2451	0.3198	0.2847	0.1504
	0.0860	0.2668	0.2863	0.3609
0.7	0.2511	0.3113	0.2861	0.1515
	0.0827	0.2715	0.2855	0.3603
0.8	0.2552	0.3044	0.2882	0.1522
	0.0804	0.2753	0.2844	0.3599
0.9	0.2576	0.2988	0.2910	0.1526
	0.0791	0.2784	0.2828	0.3596
1.0	0.2583	0.2945	0.2945	0.1528
	0.0787	0.2808	0.2808	0.3596

Table 2.1: S_{kn} coefficients ($k = 2, 4$) as a function of η for a quadrupole interaction with $I = 5/2$.

When in free space, the filled electronic shells of the probe atom possess spherical symmetry. Inside the material, due to the presence of the lattice EFG, the filled shells are distorted and lose their spherical symmetry, and this will produce an EFG that will add to the EFG already present at the probe site. The EFG is proportional to r^{-3}, and due to the proximity of the probe nucleus to the electrons in these distorted shells, this contribution can be significant. But, unfortunately, the calculation of this effect is complicated.

In a defect-free lattice the EFG at the probe site has the symmetry determined by the lattice. The presence of a defect in near proximity to the nucleus will alter significantly the symmetry at the probe site. A charged impurity or stresses in the lattice structure can significantly increase or decrease the EFG symmetry at the probe site. Defects are considered to be the most important factors that can alter or disturb the EFG in a material.

It is very difficult to model or to account for these contributions to the EFG. Still, PAC is capable of providing important information about the environment surrounding the probe nuclei because, usually, the two parameters that are used to describe the EFG at the probe site, η and V_{zz}, are unique depending on the conditions present around the probe nuclei.

Equations (2.73) and (2.81) were obtained by assuming that the microcrystals in a powder are defect-free. Even though high purity crystals can be prepared, most of the materials of interest have static defects such as impurities, lattice deformations, etc. When these defects are present in small concentrations, the EFG from these imperfections is often assumed to be described by simple distribution functions such as Gaussian and Lorentzian distributions. The perturbation functions are then modified to include the contribution of the static defects. The Gaussian and Lorentzian distributions are used when the relative width of the EFG distribution, $\delta = \Delta V_{zz}/V_{zz}$ is small.

The perturbation function is given by the convolution of the theoretical perturbation function with the distribution function. This is expressed as

$$G'_{kk}(t) = \int G_{kk}(t) f(\omega - \omega') d\omega \tag{2.83}$$

where $f(\omega - \omega')$ is the normalized distribution function and ω' is the peak frequency.

The Gaussian distribution is

$$f_G(\omega - \omega') = \frac{1}{\sqrt{2\pi}\sigma} \exp\left[-\frac{(\omega - \omega')^2}{2\sigma^2}\right] \tag{2.84}$$

σ is the width parameter of the distribution. The result of its convolution with the theoretical perturbation function for powder samples is

$$G'_{kk}(t) = S_{k0}(\eta) + \sum_{n=1}^{3} S_{kn}(\eta) \cos[\omega'_n(\eta)t] \exp\left[-\frac{(\delta\omega'_n t)^2}{2}\right] \tag{2.85}$$

where $\delta = \sigma/\omega_Q$. The peak frequencies ω'_n, as well as the damping term δ, are determined by fitting the experimental PAC data with the model.

For a Lorentzian distribution

$$f_L(\omega - \omega') = \frac{1}{\pi} \frac{\Gamma/2}{(\Gamma/2)^2 + (\omega - \omega')^2} \tag{2.86}$$

where Γ is the FWHM of the distribution. Its convolution with the perturbation function for a powder gives

$$G'_{kk}(t) = S_{k0}(\eta) + \sum_{n=1}^{3} S_{kn}(\eta) \cos[\omega'_n(\eta)t] \exp(-\delta\omega'_n t) \tag{2.87}$$

with δ defined as: $\delta = \Gamma/2\omega_Q$.

The normalized Gaussian and Lorentzian distribution functions are shown in Fig. 2.10. They represent the expected profile of the PAC spectral lines.

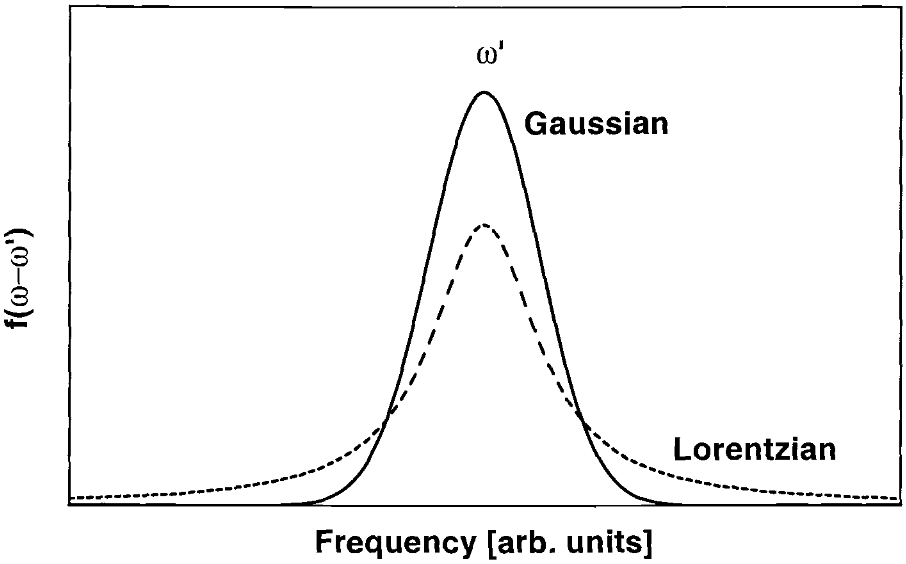

Figure 2.10: Graphs of normalized Lorentzian and Gaussian distributions, with FWHM, $\Gamma = 2.354\sigma$. ω' is the peak frequency.

2.5 TIME-DEPENDENT PERTURBATIONS

The existence of mobile charge carriers like vacancies in a material gives rise to time-varying EFGs. The motion of these dynamic defects causes the lattice to relax and alter the local lattice EFG, at least on average. A probe nucleus located in proximity to a dynamic defect feels the change in the symmetry of the local EFG which perturbs the angular correlation of the γ cascade decay. The understanding of the relaxations caused by randomly fluctuating EFGs are relevant in the study of zirconia ceramics, being related to important physical quantities such as activation energies.

The first studies of time-dependent perturbations [16] considered probe nuclei in a liquid solution. The Brownian motion of the ions and the tumbling motion of the probes in the liquid are the source of the varying EFG experienced by the probes. Assuming that the interaction between the environment EFG and the quadrupole moment of the probe nuclei varies randomly in time, the perturbation function was found to be a simple function:

$$G_{kk}(t) = e^{-\lambda_k t} \tag{2.88}$$

The damping factor λ_k is given by

$$\lambda_k = \frac{3}{5}\langle\omega_Q^2\rangle\tau_c k(k+1)[4I(I+1) - k(k+1) - 1] \tag{2.89}$$

where τ_c is the relaxation time that describes the time it takes for local configuration to change in the liquid ($\tau_c \approx 10^{-12}$), and $\langle\omega_Q^2\rangle$ is the time and spatial average of the quadrupole frequency. Eq. (2.88) is valid when $\langle\omega_Q^2\rangle\tau_c \ll 1$, which corresponds to the fast motion of small molecules in low viscosity liquids.

The slow rotational diffusion effect on the angular correlation was derived assuming a tumbling motion of the probe nuclei in an axially symmetric molecular EFG [17]. The perturbation function in this case is

$$G_{kk}(t) = e^{-\lambda_k t} G_{kk}^{static}(t) \tag{2.90}$$

$G_{kk}^{static}(t)$ is the perturbation function discussed in a previous section. $\lambda_k = k(k+1)D$, where D is the rotational diffusion coefficient. Interestingly, the liquid behave as if it were frozen and the perturbation function is modified by an exponential factor that damps the angular correlation, which is typical of dynamic effects in quadrupole interactions [18]. This result has been used to fit PAC data on zirconia ceramics [47].

A formula for simultaneous static and time-dependent perturbation was derived [47] based on the formalism of the Bloch, Wangness and Redfield theory of nuclear relaxation [19]. The perturbation function in a powder when both static and time-dependent perturbations are present is

$$G_{kk}(t) = e^{-\lambda_{k0}t} S_{k0}(\eta) + \sum_{n=1}^{3} S_{kn}(\eta) \cos(\omega_n t) e^{-\lambda_n t} \tag{2.91}$$

λ_{k0} is given by (2.89). The λ_n are defined as

$$\lambda_1 = \lambda_{1/2,3/2}$$

$$\lambda_2 = \lambda_{3/2,5/2}$$

$$\lambda_3 = \lambda_{1/2,5/2}$$

with

$$\lambda_{mm'} = \frac{6}{5}\tau_c \langle \omega_Q^2 \rangle \left[I^2(I+1)^2 + I(I+1)(m^2 + m'^2 - 1) - 3m^2 m'^2 \right] \tag{2.92}$$

When there is no static interaction, the perturbation function simplifies to (2.88), the expression derived for the perturbations in a liquid.

Other studies addressed this problem. Some tried to derive analytical expressions to describe the time-dependent perturbations [20]. But the results obtained are not entirely reliable due to assumptions and simplifications that had to be made in order to deal with this difficult problem. To circumvent the complexity of the theory of quadrupole interactions, stochastic models have been developed with the purpose of obtaining numerical solutions for the perturbation functions. An extensive reference list of stochastic models can be found in [18, 21].

Blume's stochastic model [22, 23] serves as core for various stochastic models that solved numerically the perturbation function. One model [24] considers that only a fast fluctuating EFG is present. In this case, the resulting perturbation function is equal to (2.88). Another model [25] also includes in the calculations a static EFG, the perturbation function obtained in this situation corresponds to a high visciosity case and (2.90) is revcovered.

More recently, a family of stochastic models has been developed [26, 27, 18, 21, 28]. They expanded previous models to include the trapping and detrapping of vacancies by a probe nucleus. Of particular interest to this work is the four-state stochastic model for vacancy motions with trapping and detrapping in the high-temperature regime [29]. It is described in Chapter 6.

3 ZIRCONIA

Zirconia ceramics have been extensively studied due to their various applications. As a ceramic material, it presents mechanical hardness, interesting dielectric properties, as well as resistance to heat and to the attack of chemicals. But one of the mechanical properties of zirconia renders it useless in technological applications: the tetragonal to monoclinic transformation results not only in a change of symmetry but also in a volume expansion of about 4.7 %. This transformation occurs very fast and causes a break-up of a ceramic device [30].

In order to preserve the integrity of a ceramic device, zirconia can be alloyed with metal oxides and rare-earth metal oxides such as CaO, CeO_2, MgO, Sc_2O_3, La_2O_3, and Y_2O_3. The introduction of these dopants stabilizes the material by lowering the temperature for the cubic to tetragonal and tetragonal to monoclinic phase transformations. Even though systems like CaO-, MgO- and Y_2O_3-ZrO_2 have been investigated thoroughly, it is not yet known with certainty why the introduction of dopants has a stabilizing effect; the solubility in a solid solution of the stabilizing ion together with a suitable value of the atomic radius seem to be dominant parameters in the stabilization process for zirconia [31, 32]. This work is mainly concerned with the effects of doping zirconia with yttria, Y_2O_3.

To better understand the results obtained from PAC and from the analysis presented here, in the next sections is reviewed some of the physical properties of pure and doped zirconia, the defects and previous PAC studies of zirconia systems.

3.1 ZIRCONIA STRUCTURE

Pure zirconia is a solid that can exist in three different crystalline structures or polymorphs: the monoclinic, tetragonal, and cubic phases. Also, at room temperature and at high pressures ($> 40\times10^8$ Pa) zirconia can exist as an orthorhombic crystal [33].

The monoclinic, tetragonal and cubic phases are based on the fluorite crystal structure shown in Fig. 3.1. This structure is a face-centered-cubic packing of the cations, with the anions occupying the interstitial tetrahedral sites.

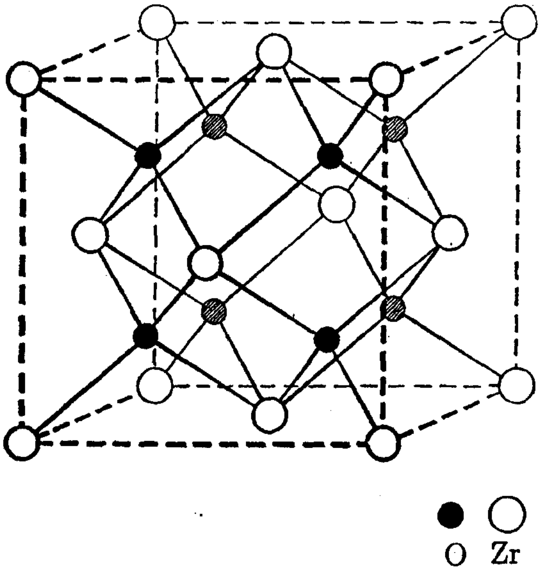

Figure 3.1: The fluorite structure of zirconia [34].

Monoclinic zirconia exists at temperatures below 1170°C. Its crystal structure is the one that most deviates from fluorite structure. It can be seen as a distortion of the fluorite structure where the unit cell is stretched along the c-axis followed by a tilt of the c-axis versus the a-axis by $\sim 9°$. Its cell dimensions are: a = 5.1505 Å, b = 5.2116 Å, c = 5.3173 Å, and $\beta = 81.22°$. It has $P2_1/c$ space group symmetry. The atomic arrangement in the unit cell is $(4e) \pm (x, y, z; \overline{x}, y + 1/2, 1/2 - z)$, with the following parameters: Zr($x = 0.2578, y = 0.0404, z = 0.2809$), O-I($x = 0.069, y = 0.342, z = 0.345$) and O-II($x = 0.451, y = 0.758, z = 0.479$). The coordination number of the Zr atom is seven. In this system there are two types of oxygen atoms, O-I has three Zr neighbors and O-II has four Zr neighbors. The O-I atoms are triangularly coordinated to the Zr and are approximately parallel to the (100) plane. The four O-II atoms are coordinated nearly tetrahedrally in a distorted square parallel to the (100) plane. The Zr atoms are located between the layers formed by the O-I and O-II atoms. At room temperature the distances between Zr and the O-I atoms range from 2.05 to 2.16 Å, and for the Zr and O-II atoms from 2.15 to 2.29 Å[35, 36].

The tetragonal phase of zirconia is stable between ~ 1170 and 2370°C. The structure of tetragonal zirconia can be represented by a slightly distorted fluorite structure where the c-axis has been stretched. The dimensions of the unit cell are $a = 3.64$ Å and $c = 2.065$ Å. The tetragonal cell is described by means of two formula units. The Zr atoms are at (0,0,0) and $(1/2, 1/2, 1/2)$. The O atoms are located at $(0, 1/2, z)$, $(1/2, 0, -z)$, $(0, 1/2, 1/2 + z)$, and $(1/2, 0, 1/2 - z)$. The parameter z is slightly dependent on temperature [37]. For instance, at T=1250°C, $z = 0.185$. The space group symmetry is $P4_2/nmc$. Each O atom is coordinated by four Zr atoms, and each Zr atom is eight-fold coordinated with four O atoms at a distance 2.455 Å, and four at 2.065 Å. The first four O atoms and the Zr form an elongated tetrahedron. The closer group O atoms and the Zr form a flattened tetrahedron rotated by 90° with respect to the first [35].

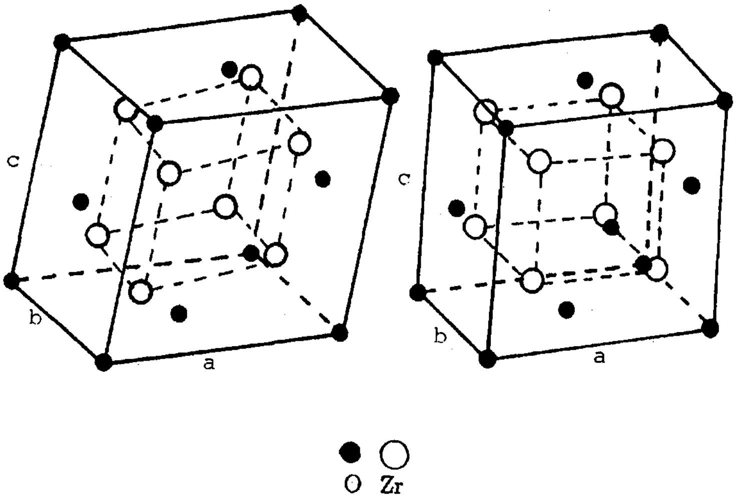

Figure 3.2: Crystal structure of monoclinic (left) and tetragonal (right) zirconia [34].

Above 2370°C and up to the melting point at 2680°C, zirconia exists in the cubic phase. The cubic phase has the fluorite structure with a lattice constant $a = 5.07$ Å. The Zr atoms are located at (0,0,0) and the O atoms are located at the eight $(\pm 1/4, \pm 1/4, \pm 1/4)$ positions. It has the space group symmetry Fm3m. Each Zr atom is eight-fold coordinated by equidistant O atoms, and the O atoms are tetrahedrally coordinated by four Zr atoms [35, 39].

In Fig. 3.3 is shown the Zr-O phase diagram. Metallic Zr is present in low concentrations up to nearly stoichiometric ZrO_2.

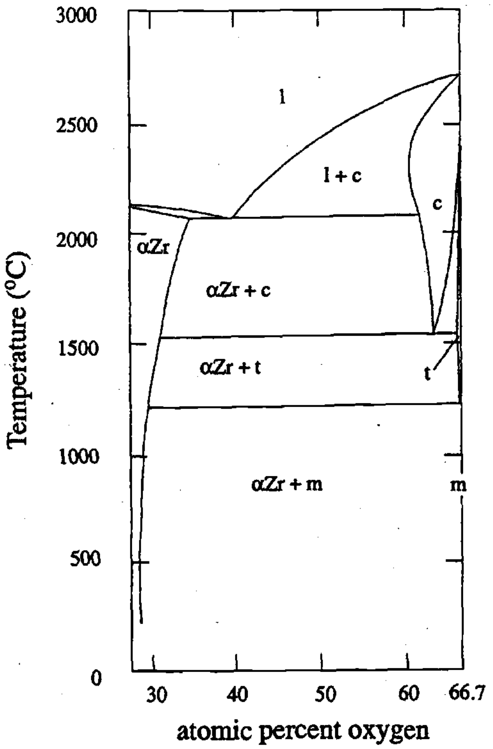

Figure 3.3: Zr-O phase diagram [40].

3.2 ZIRCONIA-YTTRIA

In Fig.3.4 is shown the zirconia-rich section of the zirconia-yttria phase diagram. Fully stabilized zirconia (FSZ) is obtained by the addition of at least 17 wt.% yttria. FSZ stabilizes to the cubic phase over the entire range of temperatures up to its melting point. Partially stabilized zirconia (PSZ) results when less of the stabilizing agent is added, PSZ is a mixture of cubic and tetragonal or cubic and monoclinic phases.

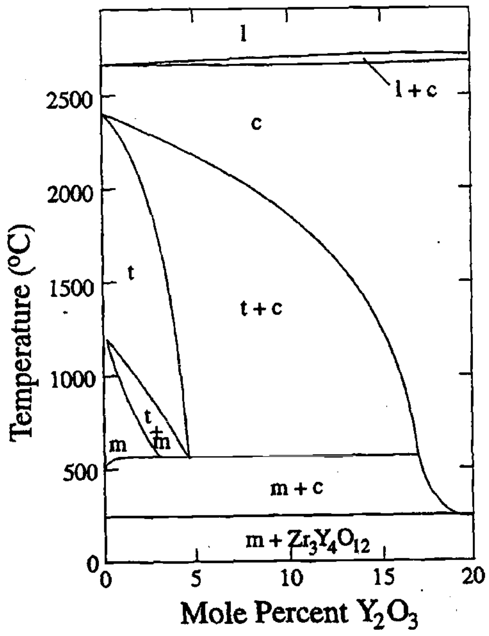

Figure 3.4: Phase diagram of the Y_2O_3- ZrO_2 system [40].

Of particular interest is PSZ. It has better mechanical and thermal characteristics than pure zirconia or FSZ [41]. It has a smaller volume change coefficient related to the tetragonal-monoclinic phase transformation. The doping of zirconia with Y_2O_3 introduces cations on the regular Zr sites. Due to charge conservation, oxygen vacancies are created. The introduction of two three-valent cations such as Y^{3+} generates one oxygen vacancy. These oxygen vacancies possess great mobility and move through the ceramic material with velocities many orders of magnitude faster than the cations [30].

3.3 POINT DEFECTS IN ZIRCONIA

Various kinds of defects can exist in a crystal. Of particular interest are point defects such as vacancies, substitutional ions, electrons, holes, interstitial atoms and impurities. Also of importance are extended defects like strains in the crystal lattice and defects that are induced by temperature changes in the material. All of these defects can, at least in principle, have their presence measured by PAC. The PAC technique can measure with great sensitivity the interaction between a probe ion and the surrounding electric field gradient. Due to this sensitivity, and in order to better interpret the results from a PAC experiment, it is useful to know what kind of defects can be present in zirconia as measured by other techniques.

In ionic conductors like zirconia ceramics, the concentration of ionic defects can be several orders of magnitude larger than the concentration of electronic defects [30]. Dynamic properties of the material, like diffusion and electrical conductivity, are dependent on the concentration of ionic defects. Various techniques have been used to characterize and quantify the ionic defects present in the material. Conductivity measurements indicate that oxygen vacancies are the main ionic defect at lower partial oxygen pressure in monoclinic [42] and in tetragonal zirconia [43, 44]. At higher partial oxygen pressure in monoclinic [42] and tetragonal zirconia [43] the dominant ionic defect is the fully-charged zirconium vacancy. Other studies using electrical conductivity measurements [45] disagree with the results at higher oxygen partial pressure; it is proposed that a coupled transport by oxygen vacancies and oxygen interstitials is the dominant effect.

Thermogravimetric measurements [46] made at temperatures between 900 and 1400°C confirm some of the results found by conductivity measurements; at lower oxygen partial pressures oxygen vacancies dominate, and at higher oxygen partial pressures zirconium vacancies dominate.

Vacancies and interstitial atoms can also be classified as dynamic defects. Strains in the crystal lattice and impurities in the ceramic material, due to their limited mobility, can be classified as static defects. Their presence can be measured by X-ray diffraction or scanning electron microscopy in the case of strains, or by analytical techniques like neutron activation analysis, neutron scattering analysis and traditional analytical chemical techniques. However, these studies do not shed any light on how static defects interact with a probe ion in a PAC experiment. It is necessary to use models to describe how the presence of static defects affects the electric field gradient around a probe ion. These models and their results are presented in Chapter 5.

3.4 PREVIOUS PAC STUDIES OF ZIRCONIA

Two different probe nuclei, ^{181}Hf and ^{111}In, have been used in PAC to study zirconia. Their dissimilar chemical characteristics allow the investigation of different properties of the sample material.

Hafnium has the same valence as zirconium; they are very similar chemically. Hafnium in zirconia occupies substitutional zirconium positions. Therefore, it cannot attract point defects in a material electrostatically. Hafnium's daughter atom, ^{181}Ta, the actual PAC probe, has a +5 formal charge, and it has an effective +1 charge when substituted in the crystal lattice. In principle, ^{181}Ta should attract negatively-charged point defects and repel oxygen vacancies which have an effective charge of +2. Monte Carlo simulations [47, 48] performed in order to reproduce frequency distributions in Hf PAC in 18.4 wt.% yttria-stabilized zirconia showed that an oxygen vacancy never populates the nearest neighboring anionic shell. This suggests that the dynamics of an oxygen vacancy near a ^{181}Ta probe may be different from a zirconium atom or different from a trivalent dopant like yttrium [49]. Hf PAC can be used to determine phase transitions, the diffusive motion of oxygen vacancies that lead to relaxation of the lattice, and the presence of impurities in the ceramic material.

^{111}In and its daughter atom, ^{111}Cd, attract oxygen vacancies, due to the fact that they have lower valences than zirconium. The probe atom, ^{111}Cd, has a formal charge of +2. In the zirconia crystal lattice this corresponds to an effective charge of −2. It is expected that ^{111}Cd will respond to the dynamics of an oxygen vacancy around a divalent or trivalent dopant in the zirconia system.

Hf PAC has been used to identify the phases and to study the phase transitions in zirconia [47]. In Fig. 3.5 are shown typical Hf PAC data for pure zirconia. The crystal lattice in each phase defines the local electric field gradient (EFG). The pure zirconia monoclinic and tetragonal phases have quite distinct PAC spectra. It can be argued that the ^{181}Ta probe can attract and trap negatively charged point defects, and that these defects, in principle, could affect the local EFG. But, at the high temperatures at which the PAC data was obtained, the trapping and detrapping of these defects by the PAC probe occur many times during the lifetime of the intermediate state of ^{181}Ta. These effects average out, and the net contribution to the local EFG comes from the crystal lattice.

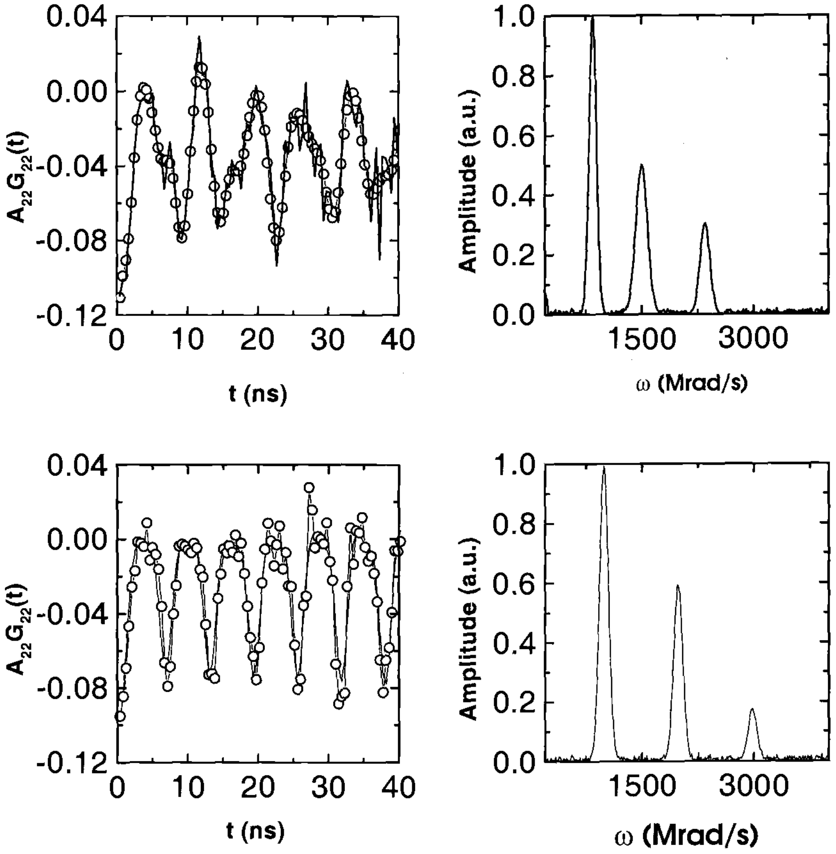

Figure 3.5: Hf PAC time and frequency spectra for monoclinic (top) and tetragonal (bottom) zirconia.

In Fig. 3.6 is shown the hysteresis curve of the tetragonal-monoclinic transformation in zirconia as measured by PAC. The large hysteresis in the transition is a consequence of the volume change of 4.7% that occurs during the transformation.

Table 3.1 lists the frequencies ω_1, ω_2, and the values of the asymmetry parameter, η. Only ω_1 and ω_2 are listed since $\omega_3 = \omega_1 + \omega_2$.

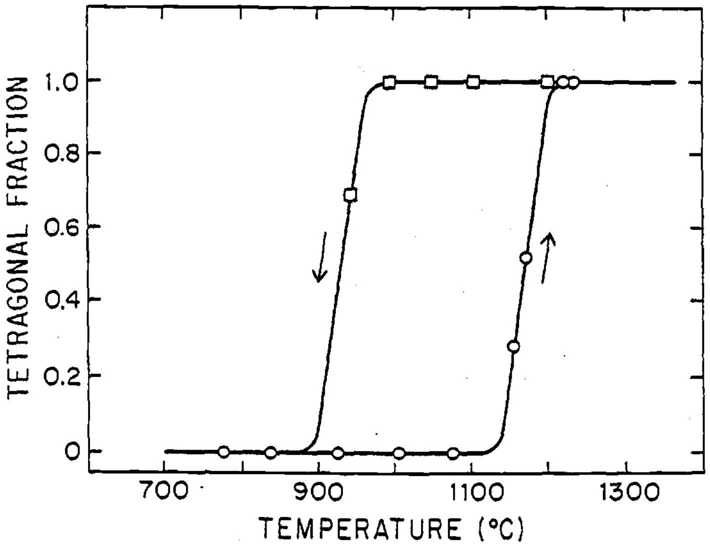

Figure 3.6: The monoclinic-tetragonal phase transformation on heating and cooling of pure zirconia [47].

phase	ω_1 (Mrad/s)	ω_2 (Mrad/s)	η
monoclinic (800°C)	847(4)	1503(6)	0.32(1)
tetragonal (1200°C)	993(4)	1985(5)	0.01(1)

Table 3.1: Hyperfine parameters in pure monoclinic and tetragonal zirconia as measured by Hf PAC [40].

Another interesting system studied with Hf PAC is yttria-stabilized cubic zirconia (CSZ). The EFG experienced at a probe site in CSZ is dependent on the oxygen vacancies and dopants surrounding it. This is very different from the EFG at a cation site in pure cubic zirconia where every probe nucleus experiences, in the case of a perfect crystal, a zero EFG. In pure tetragonal and monoclinic zirconia the PAC frequency spectrum consists of three different frequencies.

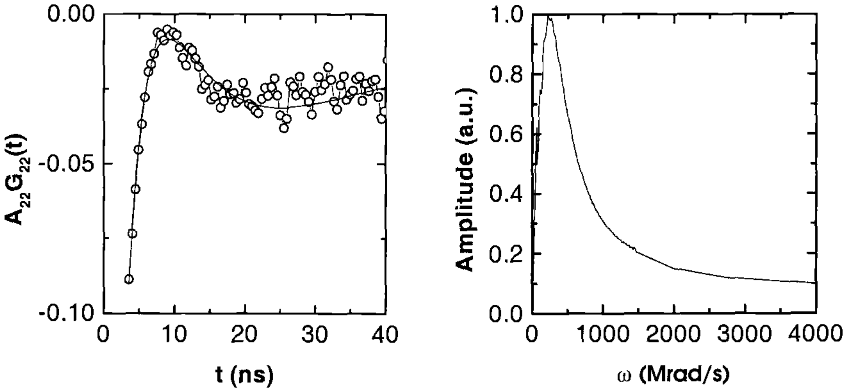

Figure 3.7: Hf PAC time and frequency spectra for 18.4 wt.% yttria cubic-stabilized zirconia.

In CSZ the PAC frequency spectrum consists of a wide distribution of frequencies, this is due to the fact that there are many different ways to arrange dopants and oxygen vacancies around the probe nuclei in CSZ. In Fig. 3.7 are shown time and frequency spectra of 18.4 wt.% yttria CSZ. Note that the wide distribution of frequencies results in a nonoscillatory behavior of the PAC perturbation function.

Phase identification can also be performed with In PAC. In Fig. 3.8 are shown typical In PAC data for 0.5 wt.% Nb_2O_3 doped zirconia [49]. ^{111}In and ^{111}Cd have lower valence than zirconium and can attract oxygen vacancies that can perturb the lattice EFG. To obtain the frequency triplets that correspond uniquely to the lattice, it is necessary to dope zirconia with niobia to remove oxygen vacancies. The triplet frequencies and η are listed in Table 3.2.

In order to study the dynamics of oxygen vacancies, zirconia can be doped with different quantities of yttria. In Fig. 3.9 is plotted the dependence of the quadrupole interaction frequency ω_Q versus temperature in tetragonal zirconia at various levels of doping [50].

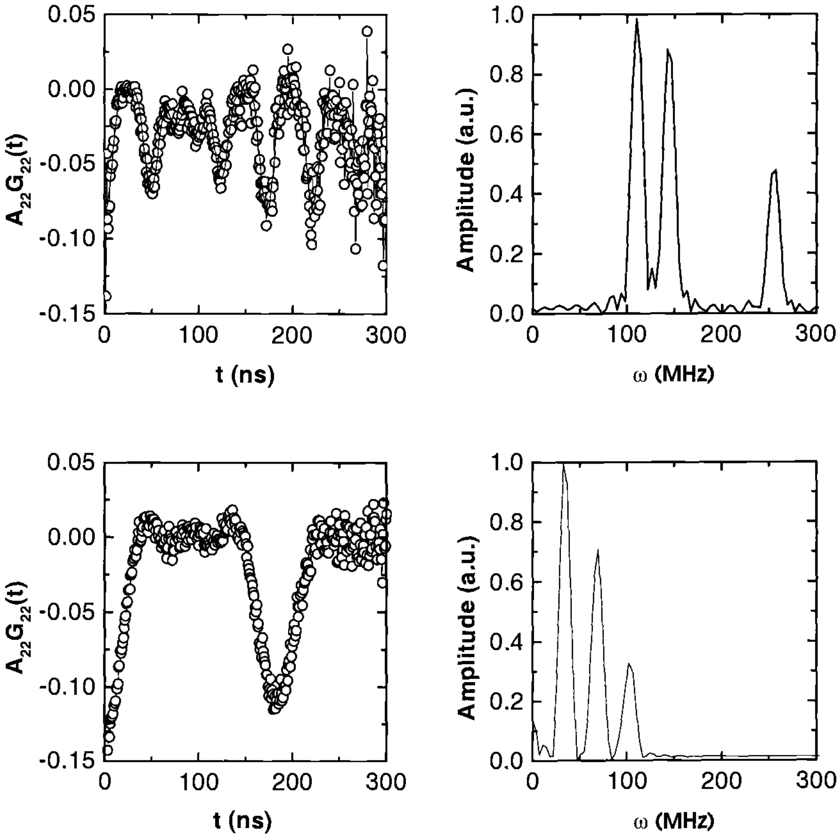

Figure 3.8: Hf PAC time and frequency domain spectra for 0.5 wt.% Nb_2O_3 doped (top) monoclinic and (bottom) tetragonal zirconia.

The weak temperature dependence in niobia-doped zirconia can be explained by the thermal expansion of the crystal lattice. The temperature dependence of the pure and yttria-doped zirconia can be explained [51] by the interaction between oxygen vacancies and the probe nuclei. An increasing concentration of yttria will result in a larger concentration of vacancies due to charge compensation. The high temperature of measurement favors the rapid motion of trapped vacancies around the probe nuclei. This rapid motion averages out the interaction between the probe and the vacancy, resulting in a weak, or even zero, EFG experienced by the probe nuclei. In this situation, the interaction frequency measured by PAC is the result of the weighted average contributions of the lattice and the average over the time a vacancy is trapped by a probe nucleus [49]

$$\omega_{measured} = f\omega_{V_O} + (1-f)\omega_{lattice} \tag{3.1}$$

where f is the trapping fraction of occupancy of the vacancy around the probe. It is temperature dependent. ω_{V_O} and $\omega_{lattice}$ are the interaction frequency when the vacancy sits next to a probe, and the interaction frequency that results from the crystal lattice. f is found from statistical mechanics:

$$f = \frac{1}{1 + \frac{1}{Nc}\exp^{-E_A/kT}} \tag{3.2}$$

where N is the number of occupancy sites. N is 8 for nearest-neighbor sites and 24 for next-nearest neighbor sites. E_A is the binding energy, k is Boltzmann's constant and T is the temperature. Computer fits using this model gave best results when $N = 24$, $\omega_{V_O} = 0$ Mrad/s, and $E_A = 0.44(3)$ eV and 0.8(1) eV for the hopping barrier [51].

phase	ω_1 (Mrad/s)	ω_2 (Mrad/s)	η
monoclinic (800°C)	104.6(3)	147.9(4)	0.63(2)
tetragonal (1200°C)	38.5(3)	73.6(4)	0.19(1)

Table 3.2: Hyperfine parameters in 0.5 wt.% Nb_2O_3 doped monoclinic and tetragonal zirconia as measured by In PAC [52].

Another model [40] was proposed to explain the dynamics of the oxygen vacancy at high temperatures near a probe site. In this model, three physical parameters associated to the oxygen vacancy's motion, are associated to the

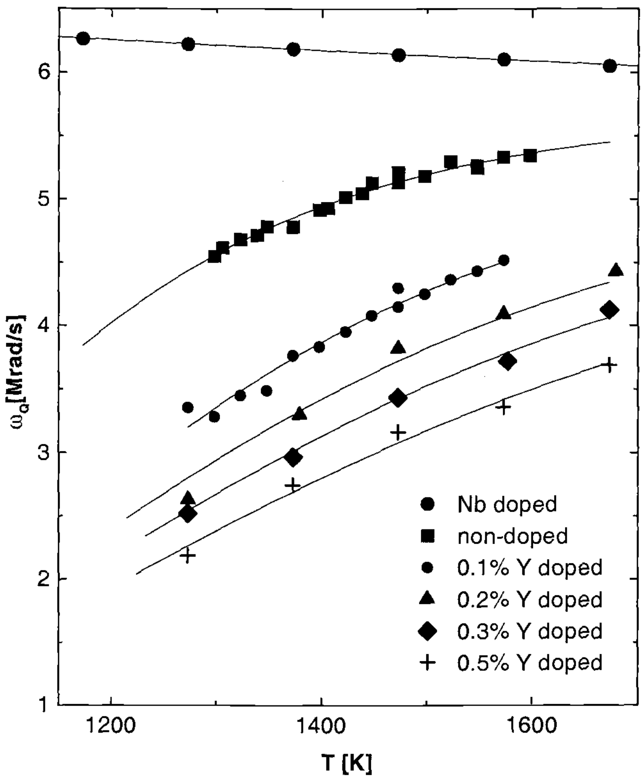

Figure 3.9: Temperature dependence of the quadrupole interaction frequency ω_Q. After [50].

damping of the PAC perturbation function. It is assumed that the oxygen vacancies can hop among equivalent sites around the probe nuclei; they can be trapped by and can detrap from the PAC probes. The activation energies of these three processes, derived by this model, are 0.3-0.6 eV, 0.9-1.6 eV, and 0.4-0.6 eV, respectively [40].

With the improvement in sample-making techniques, it was possible to observe the expected axial symmetry of the EFG in tetragonal zirconia [52, 50]. Also, as a result of the use of purer samples, better values for the binding energies for the vacancy-cadmium and vacancy-yttrium pairs were found to be 0.62(3) eV and 0.28(3) eV, respectively [50].

4 EXPERIMENTAL METHODS

Since the main objective of this thesis is the analysis and interpretation of PAC data, the experimental hardware will be discussed briefly here, with the purpose to make the reader familiar with the experimental aspects of the PAC technique. The data utilized in this thesis were collected by other members of the PAC research group at OSU [40, 47, 52, 53]. Details about sample preparation can be found in these references. The spectrometers used to collect the data analysed in this work were built by the OSU PAC research group. The construction, operation and characteristics of these spectrometers are described in [47, 10, 54].

4.1 PAC SPECTROMETER

The main tasks of the spectrometer are to detect and identify the energy, the time separations, and the angle between the radiations emitted from a sample doped with PAC probe nuclei. The experimental arrangement of the PAC spetrometer can be seen in Fig. 4.1. It consists of four detectors placed in a plane and at 90° intervals about the sample. The angular correlation anisotropy for powder samples is maximized in this geometry. Each detector is formed by a fast-response BaF_2 scintillator and a photo-multiplier tube (PMT). The distance between each detector and the sample is usually a few centimeters.

The detectors collect data according to a 'start-stop' procedure: When one of the PMTs detects a signal corresponding to a γ_1 radiation, it immediately,

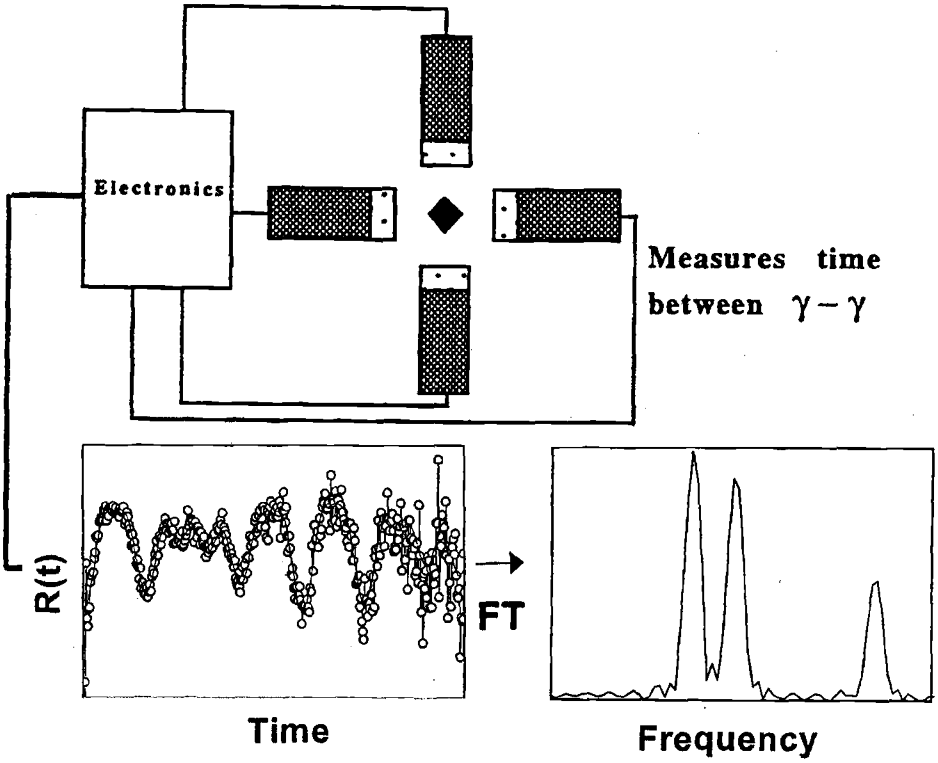

Figure 4.1: Simplified PAC experimental setup. Four detectors placed at 90° and in a plane with the sample in the center.

within the time response of the electronic equipment, stops collecting data and commands the other three detectors to start looking for the γ_2 radiation at the same time that a timing clock starts. As soon as one of the PMTs detects γ_2 the process stops, the energy and the time interval between the detection of the γ rays are recorded and then the cycle starts again. The time the detectors spend waiting for γ_2 depends on the half-life of the intermediate state. Usually, this time is less than five half-lives. If no radiation with the right energy is detected in this time interval, the system resets and the PMTs detectors start again to look for radiations with the right energy. The stop signal is delayed so that it is possible for a γ_2 to be detected by a PMT first and a γ_1 be detected by another PMT. In this situation, the time measured is negative and these combinations are called reverse spectra.

Of interest is the time interval of detection between γ_1 and γ_2. These coincidence pairs of $\gamma_1 - \gamma_2$ are called events. The time interval of each event is recorded in a histogram array, where each array consists of a number of channels (500 -1000) 1 ns wide. Usually, data is collected for 8-24 hours. In a typical run 10^7 events are accumulated, and the channel that corresponds to the peak of the spectrum accumulates in excess of 10^4 events. The events measure the lifetime of the intermediate state. The histogram thus represents the exponential decay of the intermediate state modulated by the perturbation on the angular correlation and other factors. In Fig. 4.2 are shown typical forward and reverse accumulated coincidence spectra.

On the opposite side of the true coincidence counts are the background counts. There is a small, but perceptible, slope decreasing from the peak of the spectrum. Its origin is electronic, but the exact cause of this effect is not clear.

There are eight possible pairs of detectors that can record events; four give forward spectra and the other four reverse spectra. The spectra recorded by a pair of detectors is given by

$$D_{ij}(\theta,t) = N_0 \epsilon_i \epsilon_j \sigma \exp\left(-\frac{t}{\tau}\right) W(\theta,t) + B_{ij} \tag{4.1}$$

where i and j indicate the detector pair, σ is the sample-self absorption, N_0 is the sample activity, ϵ_i and ϵ_j are the PMT efficiencies, τ is the lifetime of the

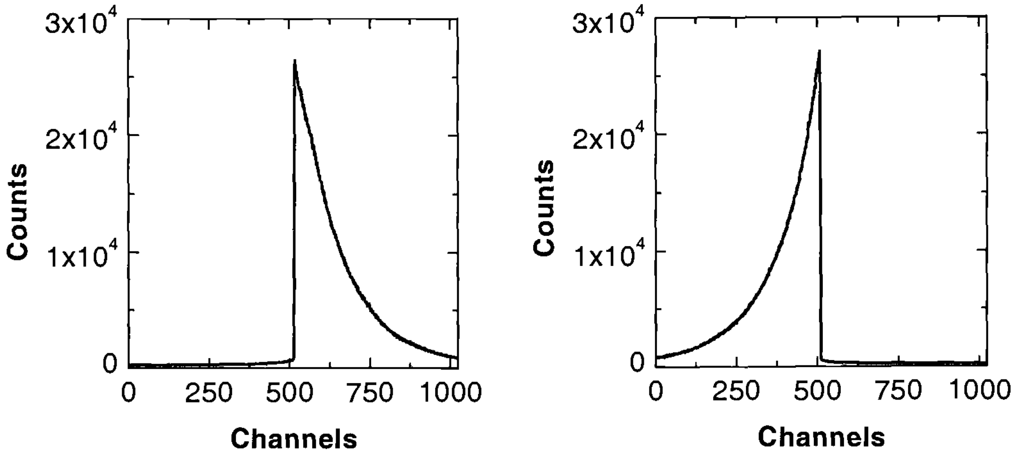

Figure 4.2: Accumulated coincidence spectra. Forward (left) and reverse (right) spectra of actual PAC data.

intermediate level, and B_{ij} is the background count.

The counting rate is obtained after subtracting the background count:

$$C_{ij}(\theta,t) = D_{i,j}(\theta,t) - B_{ij} = N_0\epsilon_i\epsilon_j\sigma \exp\left(-\frac{t}{\tau}\right) W(\theta,t) \qquad (4.2)$$

The correct removal of the background count is very important. When fitting PAC data, one is usually interested in the line broadening δ and the asymmetry parameter η. Both parameters can be affected by the way the background count is subtracted, particularly δ. One method to remove the background count uses the count average of channels located as far away as possible from the peak of the spectrum where the background is the flattest (see Fig.4.2). Also, it is possible to extract the background count by fitting the modified exponential decay with the expression: $c = a_0 exp(-t/\tau) + b$, where b gives the background count.

Several algebraic procedures may be used to extract the perturbation function from the C_{ij}s [55]. One of them is to form the forward and reverse counting ratios as:

$$\begin{aligned} R_f(t) &= 2\frac{\sqrt{C_{02}C_{13}} - \sqrt{C_{03}C_{12}}}{\sqrt{C_{02}C_{13}} + 2\sqrt{C_{03}C_{12}}} \\ R_r(t) &= 2\frac{\sqrt{C_{20}C_{31}} - \sqrt{C_{30}C_{21}}}{\sqrt{C_{20}C_{31}} + 2\sqrt{C_{30}C_{21}}} \end{aligned} \tag{4.3}$$

For practical calculations the expression (3.38) can be approximated as:

$$W(\theta, t) = 1 + A_{22}G_{22}(t)P_2(\cos\theta) \tag{4.4}$$

Inserting (4.4) and (4.2) into (4.3) gives the four spectra ratio

$$R(t) = A_{22}G_{22}(t) \tag{4.5}$$

where

$$G_{22}(t) = S_{20} + S_{21}\cos(\omega_1 t) + S_{22}\cos(\omega_2 t) + S_{23}\cos(\omega_3 t) \tag{4.6}$$

The anisotropy coefficient for ^{111}In is $A_{22} = -0.180$, and for ^{181}Hf is $A_{22} = -0.295$. These values of the anisotropies are only valid for a point source and point detectors. Since these conditions are not true for most experiments, A_{22} is replaced by the effective anisotropy A_{22}^{eff}. As a shorthand, the effective anisotropy is still designated A_{22}.

A PAC experiment is essentially a counting of radioactive decays that occur in a random way. As a consequence, the error associated with N counts is $\sqrt{N}$, which is one standard deviation.

4.2 DATA FITTING

Expression (4.5) gives the experimental perturbation function $G_{22}(t)$. It contains all the information that can be obtained in a PAC experiment. The correct interpretation of the perturbation function allows the description of the environment around the probe nuclei. Also, its Fourier transform can serve as a first step in identifying the key aspects about the material being analysed, like the phase the material is in or the number of probe sites. Examples of $R(t)$ and its Fourier transform can be seen in Figs 2.5, 2.7 and 2.8. In the case of zirconia, the cubic, monoclinic and tetragonal phases are easily identifiable.

To extract all the parameters associated with the environment around the probe, it is necessary to model the experimental data with empirical or theoretical functions. The successful fitting of the data to a model is an indication that it is possible to describe correctly the environment around the probe nuclei.

A fitting program [56] based on the Levenberg-Marquardt algorithm has been used by the PAC research group. More recently, a fitting subroutine that allows the fitting of multiple data sets related to each other through common parameters was developed [57]. It is also based on the Levenberg-Marquardt algorithm. In this work both fitting subroutines have been used.

The goodness of a fit can be described by the parameter χ^2. Its most useful definition is

$$\chi^2_\mu = \sum_i^N \frac{(y_i - y(xi))^2}{\mu\sigma_i^2} \tag{4.7}$$

which is the reduced form of χ^2. y_i is the ith data point, $y(x_i)$ is the value of the fitting function, σ_i is the uncertainty of the data point, and μ is given by the number of data points minus the number of free parameters used in the fitting.

In this definition, χ^2_μ approaches one for a perfect fit. If $\chi^2_\mu > 1.5$, the fitting function cannot represent the data properly. $\chi^2_\mu < 1$ is an indication that the uncertainties have not been calculated correctly. A good fit has $\chi^2_\mu \sim 1.1$.

The Levenberg-Marquardt algorithm is a least-squares fitting method whose purpose is to find the parameters used to define the fitting function in such a way that χ^2_μ is minimized. A description of this algorithm can be found in [58, 59]

4.3 RANDOM NUMBERS

Part of this work (see Chapter 5) consists in the use of a model to describe the experimental PAC data. To generate the functions that describe this model some very long series of random numbers are necessary. Since portability of these series is important, instead of using true random numbers, a subroutine that generates pseudo-random numbers, *rand2* [58], was used. To verify that this subroutine can generate a series of uncorrelated numbers, a series of tests were performed.

Usually, in the case of defective generators, it is possible to discern visually patterns or trends in plots of the run sequence, histogram or scatter plots of the series of generated numbers. As an example, Fig. 4.3 shows a scatter plot of each number generated against the number previously generated $(x_i \times x_{i+1})$. In this kind of plot a significant number of outliers or the presence of patterns

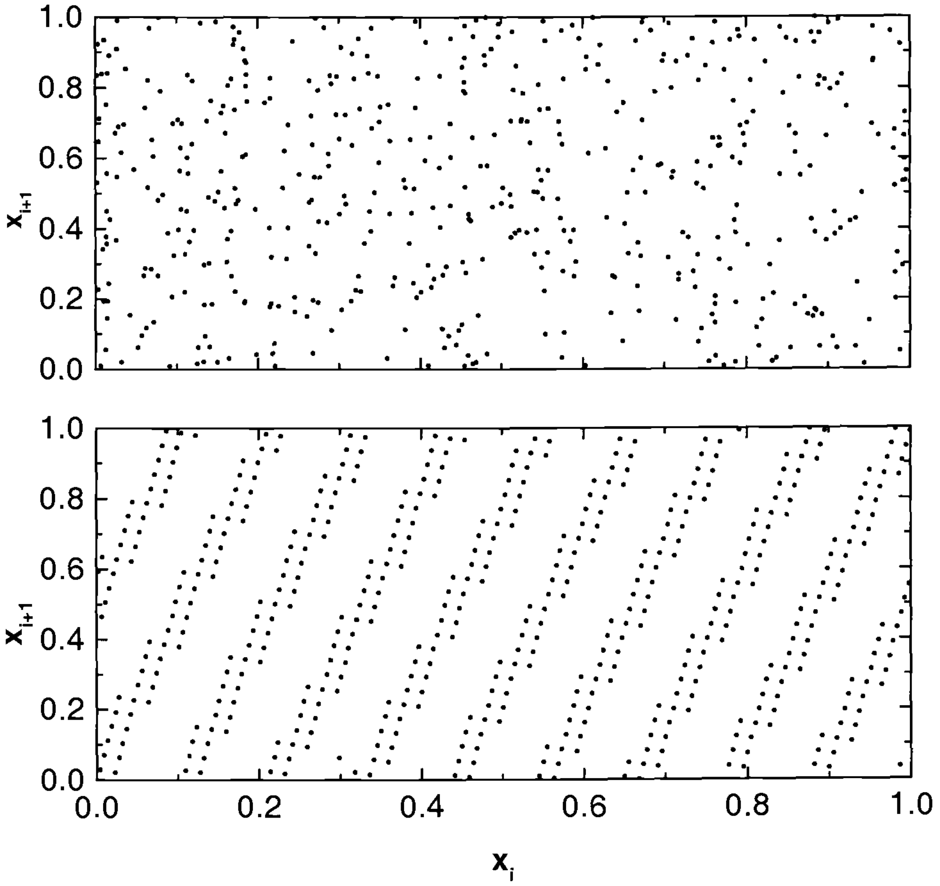

Figure 4.3: Scatter plot of pseudo-random numbers. *Good* (top) and *suspicious* (bottom) generators produce distinct plots. The presence of regular patterns on the bottom plot is an indication of correlation.

is an indication that there is a problem with the generator.

Simple statistical tests can be performed on the number series to assess its randomness and uniformity [60]. If the random numbers are distributed with a uniform probability, the following condition must be satisfied for the kth moment of the random distribution:

$$\frac{1}{N}\sum_{i=1}^{N} x_i^k \simeq \frac{1}{k+1} \tag{4.8}$$

A test with $N = 10^7$ and $k = 1$, 3 and 7 yields 0.49999, 0.246959, and 0.123661, respectively.

Another test to evaluate whether the random numbers are distributed uniformly is the χ^2 test. Data from the histogram of observed distributions of random numbers allows one to calculate

$$\chi^2 = \sum_{i=1}^{k} \frac{(O_i - E_i)^2}{E_i} \tag{4.9}$$

where k is the number of categories or bins in the histogram (see Fig. 4.4), O_i is the observed frequency per bin and E_i is the expected frequency. For $N = 10^7$ and $k = 100$, the critical value at the 5% level of significance is $\chi^2_{0.05,100} = 124.24$. The value found is $\chi^2 = 34.85$, well below the critical value.

The correlations between neighbors can be tested by taking the sum

$$C(k) = \frac{1}{N}\sum_{i=1}^{N} x_i x_{i+k} \simeq \frac{1}{4} \tag{4.10}$$

For $k = 10$, 50, 100 and 1000 the values of $C(k)$ are 0.249993, 0.249867, 0.249759 and 0.249586, respectively.

The correlation between pseudo-random numbers were measured with two physical tests [61, 62]. The first is a *random walk* test. On a plane which is divided in four equal blocks, each of which has an equal probability the random walker will be after a walk of length n. This test is performed N times and the number of occurrences in each of the four blocks is compared to the expected value of $N/4$, using a χ^2 test with three degrees of freedom. The generator fails if the χ^2 value exceeds 7.815 in at least two of three independent runs. This should occur with a probability of 3/400. The value found was $\chi^2 = 3.7815$

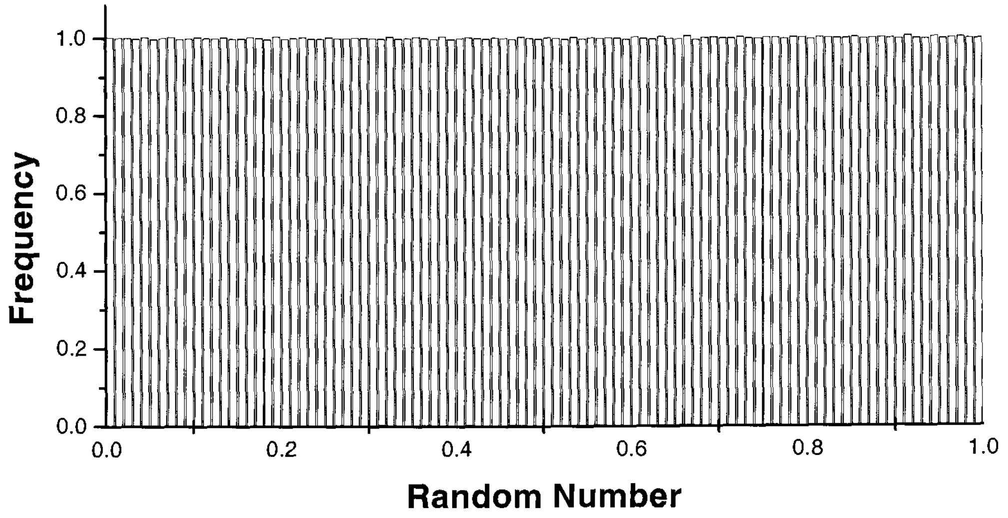

Figure 4.4: Histogram of the observed frequency of random numbers, $N = 10^7$.

with $n = 500$ and $N = 10^6$.

The second test used to quantify the correlations present in the pseudo-random numbers is the *n-block* test. In this test a sequence $\{x_1, x_2, \ldots, x_n\}$ of uniformly distributed random numbers $0 \leq x_i \leq 1$ is generated and the average $\bar{x}$ is calculated. If $\bar{x} \geq 1/2$, $y_i = 1$ is chosen; otherwise $y_i = 0$. This is repeated N times. A χ^2 test on the variables y_i with one degree of freedom is performed. Each test is repeated, and the generator fails the test with fixed n if at least two out three χ^2 values exceeds 3.841, which should occur with a probability of about 3/400.The value found was $\chi^2 = 3.1055$ with $n = 500$ and $N = 10^6$.

The subroutine *rand2* passed in the tests above, indicating that the series of pseudo-random numbers used in this work is reliable.

5 RANDOM STATIC EFGS

Random strains, electric fields, point defects and other static perturbations on the crystal lattice produce a distribution of EFGs that add to theideal EFG of the perfect crystal. This distribution of EFGs leads to line broadening and a change in the observed asymmetry parameter η since the EFG no longer has the symmetry of the perfect crystal.

Random perturbations have been studied, but the focus has usually been on stochastic fluctuations to study dynamic processes in solids [63, 64, 65, 26, 27, 66, 28, 29] or liquids [67, 68, 69] with static perturbations only being treated as a limiting case, if at all. In solids, time-dependent perturbations are usually moving point defects, like vacancies or interstitial atoms, which give rise to line broadening and relaxation. The measurement of relaxation over a temperature range can be used to gain information about hopping, trapping or detrapping rates (see Chapter 6). On the other hand, static line broadening has been used to characterize nanocrystalline materials by estimating the fraction of probe atoms sitting in or near grain boundaries [70]. Static line broadening still is not well understood, and PAC spectra exhibiting static line broadening are usually fitted to a Lorentzian [71] or to a Gaussian [72, 73] without much theoretical justification. Also, earlier research has explored the theoretical aspects of line broadening, but did not provide quantitative expressions that can be fitted immediately to experimental spectra [74].

It is difficult to obtain quantitative information about dynamic processes from the analysis of line broadening because one must be able to separate the contributions from static and dynamic defects. Some information about the origin of the line broadening can be obtained by studying the temperature dependence of the broadening. The line broadening produced by static defects is weakly affected by temperature changes, whereas the broadening that is caused by moving defects is highly dependent on the temperature of the material.

In this chapter, a model that simulates the static line broadening and its relation to the changes in the asymmetry parameter η is presented. This model assumes that the static line broadening has to be directly related to a change in the parameter η since the related EFGs do not have the symmetry of the crystal.

Defects can produce a random EFG^{ran} that is added to the EFG^{lat} of the perfect lattice. As a consequence, both line broadening and the asymmetry parameter η approximately depend only on the ratio of the two EFG components V_{zz}^{ran} and V_{zz}^{lat}, as long as $|V_{zz}^{ran}|$ is small compared to $|V_{zz}^{lat}|$.

5.1 THE STATIC RANDOM DEFECT MODEL

To model the EFG of the static distributions of dissolved impurities and defects in a material, a number of charges (50-5,000) were placed randomly inside a sphere. The EFG at the center of this sphere arising from the charge distribution is

$$V_{\alpha\beta}^{ran} = \frac{Ze}{4\pi\epsilon_0} \sum_{i\neq 0} \frac{1}{r^5} \begin{pmatrix} 3x_i^2 - r_i^2 & 3x_iy_1 & 3x_iz_i \\ 3x_iy_i & 3y_i^2 - r_i^2 & 3y_iz_i \\ 3x_iz_i & 3y_iz_i & 3z_i^2 - r_i^2 \end{pmatrix} \tag{5.1}$$

where r_i is the vector from the origin to the point charge i. The center of the sphere represents the position of a probe site.

Although, in general, the EFG of the undisturbed site may have any symmetry, the model is limited to cubic and axial symmetries, and nuclear probes with $I = 5/2$. For axial symmetry ($\eta = 0$), EFG^{lat} is added to EFG^{ran}. EFG^{lat} is given by

$$V_{\alpha\beta}^{lat} = \begin{pmatrix} V_{xx}^{lat} & 0 & 0 \\ 0 & V_{yy}^{lat} & 0 \\ 0 & 0 & V_{zz}^{lat} \end{pmatrix} \tag{5.2}$$

where the Laplace equation requires $V_{xx} + V_{yy} + V_{zz} = 0$.

The EFG at the center of the sphere was calculated for a large number of random charge distributions ($N_s = 1 \times 10^6$) to obtain a probability distribution of random electric field gradients, EFG^{ran}.

The diagonalization of the resulting EFG tensors yields a distribution of V_{zz}s and ηs, and hence a distribution of ω_1, ω_2 and ω_3 (see Section 2.4). The distributions of V_{zz}s are characterized by their most probable values V_{zz}^{ran}. The ratio

$$\gamma = \frac{V_{zz}^{lat}}{V_{zz}^{ran}} \tag{5.3}$$

is used to define the distributions of the EFGs thus obtained.

From a theoretical point of view, the correct interpretation of the PAC time spectrum is equivalent to solving the following equation:

$$G_{22}(t) = \int_0^1 \int_{-\infty}^{\infty} P(\eta, V_{zz}) G_{22}(\eta, V_{zz}, t) dV_{zz} d\eta \tag{5.4}$$

This is a rather complicated expression. Besides, one lacks a complete knowledge of the distribution function $P(\eta, V_{zz})$. With the static random defect model (SRDM) (5.4) is approximated by

$$G_{22}(t) = \frac{1}{N_s} \sum_{i=1}^{N_s} G_{22}^i(\eta, V_{ZZ}, t) \tag{5.5}$$

where $G^i_{22}(\eta, V_{ZZ}, t)$ is the perturbation function (4.6) for a probe site. The values of η and V_{zz} are obtained from the distributions of EFGs calculated from the spherical charge distributions.

As mentioned above, $G_{22}(t)$ has all the information one can extract from a PAC experiment. The main objective of these simulations is to obtain expressions for $G_{22}(t)$ to describe cubic and axial materials for various defect concentrations. The model utilized here is, in a sense, a statistical model that seeks to simulate the influence of physical defects on the PAC spectra.

The distributions were calculated for other shapes (cubes, ellipsoids, etc.), but the results were essentially identical. This is expected since the EFGs are proportional to r^{-3}. Also, distributions were computed for both bare and exponentially screened impurity potentials with no difference other than scale factors. The model has no intrinsic length scale and the dimension of the sphere does not relate to a unit cell of the crystal.

5.2 CUBIC MATERIALS, $\gamma = 0$

The simulations presented in this section are representative of a defective cubic material. The EFG produced by a cubic crystalline lattice is zero, so the distributions shown below represent the effects of defects alone. Distributions were calculated for different numbers of charges placed inside the spheres, but there were no differences between distributions other than scale factors.

Figs. 5.1-3 show the distributions of the absolute value of the largest eigenvalues $|V_{zz}|$, of the asymmetry parameter η, and the transition frequencies ω_1, ω_2 and ω_3, respectively. Since polarization is not observed in the experiments, the absolute absolute value $|V_{zz}|$ is used.

These distributions are highly asymmetric and they share a common feature: they can be well described by a sum of Lorentzians. The distribution of $|V_{zz}^{ran}|$, Fig. 5.1, is scaled with respect to the most probable value of $|V_{zz}^{ran}|$. Therefore, the peak value of this distribution corresponds to $|V_{zz}^{ran}| = 1$. The shape of the curve does not depend on the magnitude of the distribution at all. As an example, the scaled distribution of $|V_{zz}^{ran}|$ is given by

$$\begin{aligned} P(|V_{zz}^{ran}|) = & \frac{0.0228189}{0.77983 + (|V_{zz}^{ran}| - 0.055426)^2} \\ & - \frac{0.022461}{0.767066 + (|V_{zz}^{ran}| - 0.0564189)^2} \end{aligned} \tag{5.6}$$

The distribution function $P(\eta, |V_{zz}|)$ obtained from the simulations is represented by the surface shown in Fig. 5.4.

With $P(\eta, |V_{zz}|)$ it is possible, in principle, to calculate $G_{22}(t)$ for a defective cubic material. The description of this function is very complicated. Since the main objective of the SRDM is to find an expression for $G_{22}(t)$, a numerical representation of $P(\eta, |V_{zz}|)$ is of little help because the integral in (5.4) still must be solved.

In this model, the perturbation function is now calculated according to (2.81):

$$G_{22}(t) = \frac{1}{N_s}\left(\sum_{i=1}^{N_s}[S_{20}^i + S_{21}^i\cos(\omega_1^i t) + S_{22}^i\cos(\omega_2^i)t) + S_{23}^i\cos(\omega_3^i t)]\right) \tag{5.7}$$

with $S_{kk}^i = S_{kk}(\eta_i)$ and $\omega_k^i = \omega_k(\eta_i, |V_{zz}|_i)$.

As a matter of convenience, equation (5.7) is rewritten as

$$G_{22}(t) = f_0 + f_1(t) + f_2(t) + f_3(t) \tag{5.8}$$

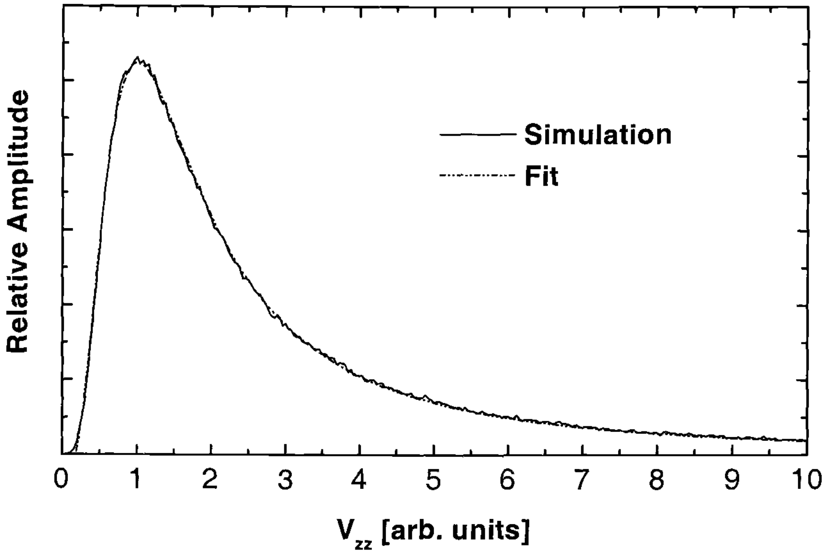

Figure 5.1: Distribution of the absolute values of V_{zz}, and fit to the distribution, $\gamma = 0$.

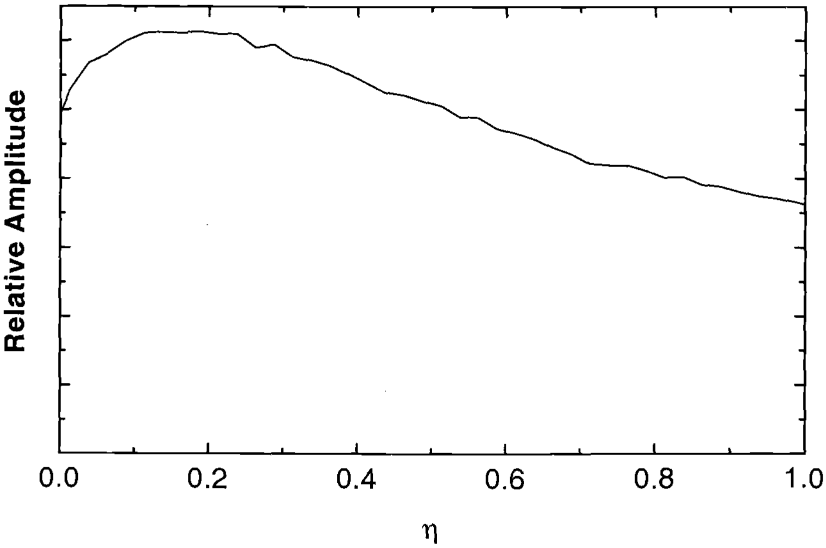

Figure 5.2: Distribution of the asymmetry parameter η, $\gamma = 0$.

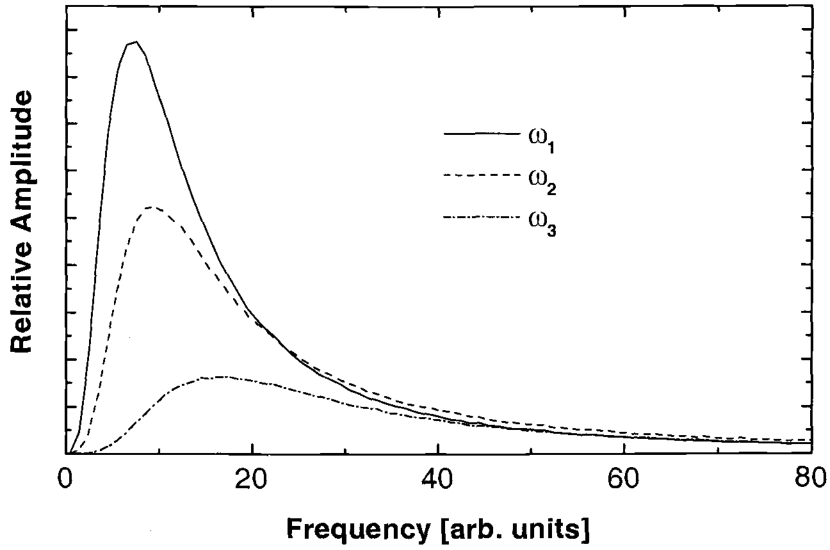

Figure 5.3: Distribution of transition frequencies, $\gamma = 0$.

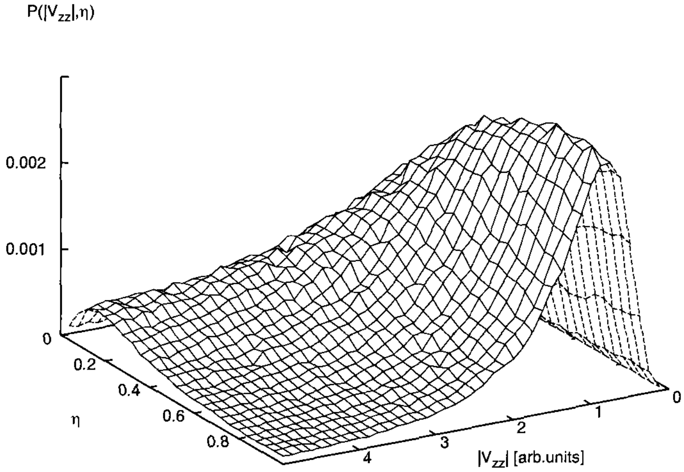

Figure 5.4: Distribution $P(\eta, |V_{zz}|)$, $\gamma = 0$.

where

$$f_0 = \frac{1}{N_s} \sum_{i=1}^{n_s} S_{20}^i \tag{5.9}$$

$$f_1(t) = \frac{1}{N_s} \sum_{i=1}^{N_s} S_{21}^i \cos(\omega_1^i t) \tag{5.10}$$

$$f_2(t) = \frac{1}{N_s} \sum_{i=1}^{N_s} S_{22}^i \cos(\omega_2^i t) \tag{5.11}$$

$$f_3(t) = \frac{1}{N_s} \sum_{i=1}^{N_s} S_{23}^i \cos(\omega_3^i t) \tag{5.12}$$

The simulated perturbation function, $G_{22}(t)$, and its constituents, $f_1(t), f_2(t)$ and $f_3(t)$, are shown in Fig. 5.5. Their behavior is nonoscillatory, as expected. In order to find an expression for $G_{22}(t)$ derived from the numerical simulations, the constituents $f_1(t), f_2(t)$ and $f_3(t)$ were fitted with the following function

$$y(t) = a_0 \cos[(a_1 t)^{a_2}] \exp[-(a_3 t)^{a_4}] \tag{5.13}$$

where the a_is are free fitting parameters. Several fitting functions can be used, the advantage of (5.13) is the small number of parameters used in the fitting. In the scale used in Fig. 5.5 it is not possible to distinguish between the results of the simulations and the fits. The perturbation function for $\gamma = 0$ is given by:

$$\begin{aligned}
&G_{22}(t) = -0.22647 \\
&- 0.339859 \cos[(14.851\omega_Q^{fit} t)^{0.797764}] \exp[-(5.2707\omega_Q^{fit} t)^{0.482657}] \\
&- 0.283964 \cos[(20.1621\omega_Q^{fit} t)^{0.804196}] \exp[-(8.11835\omega_Q^{fit} t)^{.388161}] \\
&- 0.149709 \cos[(34.6959\omega_Q^{fit} t)^{0.811655}] \exp[-(13.0661\omega_Q^{fit} t)^{0.433809}]
\end{aligned} \tag{5.14}$$

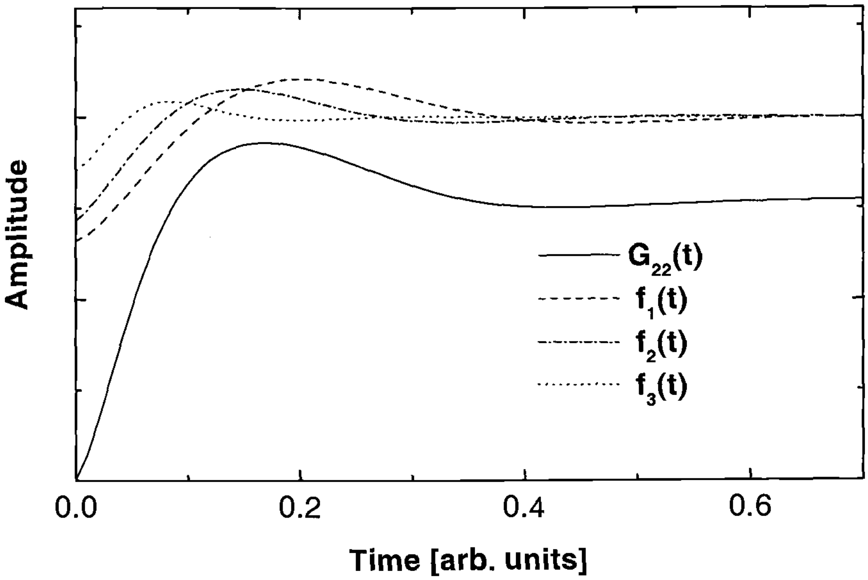

Figure 5.5: Simulated perturbation function, $G_{22}(t)$, and its constituents, $f_1(t), f_2(t)$ and $f_3(t)$, $\gamma = 0$.

where ω_Q^{fit} is the fitting parameter. With (5.14) it is possible to fit experimental PAC data for defective cubic materials using only two fitting parameters, ω_Q^{fit} and A_{22} (see Eq. (4.5)). In order to test the validity of the model being proposed, a series of tests were performed. Experimental PAC data for different materials are fitted with the SRDM. The results are presented in the following subsections.

5.2.1 Cubic Niobium Metal

Niobium is a metal with a body-centered cubic structure. Since it has cubic symmetry, the only EFG at a probe site is due to the presence of defects.

PAC data on Hf-doped niobium metal with different impurity contents (0.84 – 8.4 at.%) were collected [53]. The probe atom in these PAC experiments is ^{181}Ta. Since these samples are free of dynamic defects, the PAC data obtained in these experiments can be fitted with (5.14).

The time and the corresponding Fourier spectra of the PAC data and the fits with the SRDM are shown in Figs. 5.6 and 5.7. In Table 5.1 are listed the impurity levels, the history of the samples, and the parameters A_{22} and ω_Q^{fit} obtained from the fits. These samples were irradiated at a reactor to produce the desired ^{181}Hf activity, and are susceptible to radiation damage. In Table 5.1, *CW* refers to samples whose PAC spectra were measured in a cold-worked condition at room temperature, and *AN* refers to samples that were annealed in order to remove any radiation damage.

5.2.2 Cubic Stabilized Zirconia

Zirconia is stabilized in the cubic phase in the full range of temperatures when it is doped with at least 17 wt.% yttria. Since yttrium is three-valent, its addition as a dopant to zirconia will cause one oxygen vacancy to be formed for every two atoms added. In cubic zirconia the EFG at a probe site vanishes due to the cubic symmetry. The replacement of Zr^{+4} with a Y^{+3} disturbs the cubic symmetry and the EFG is no longer zero. The EFG is the same as an empty lattice with a relative charge of $-e$ at the position of the Y ion. Also, when an O^{-2} is removed, a vacancy is created and the EFG is the same as an empty lattice with a relative charge of $+2e$ at the site of the vacancy. In this way, the EFG at a site in stabilized zirconia depends on the surrounding distribution of oxygen vacancies and dopants. The dopants and vacancies can

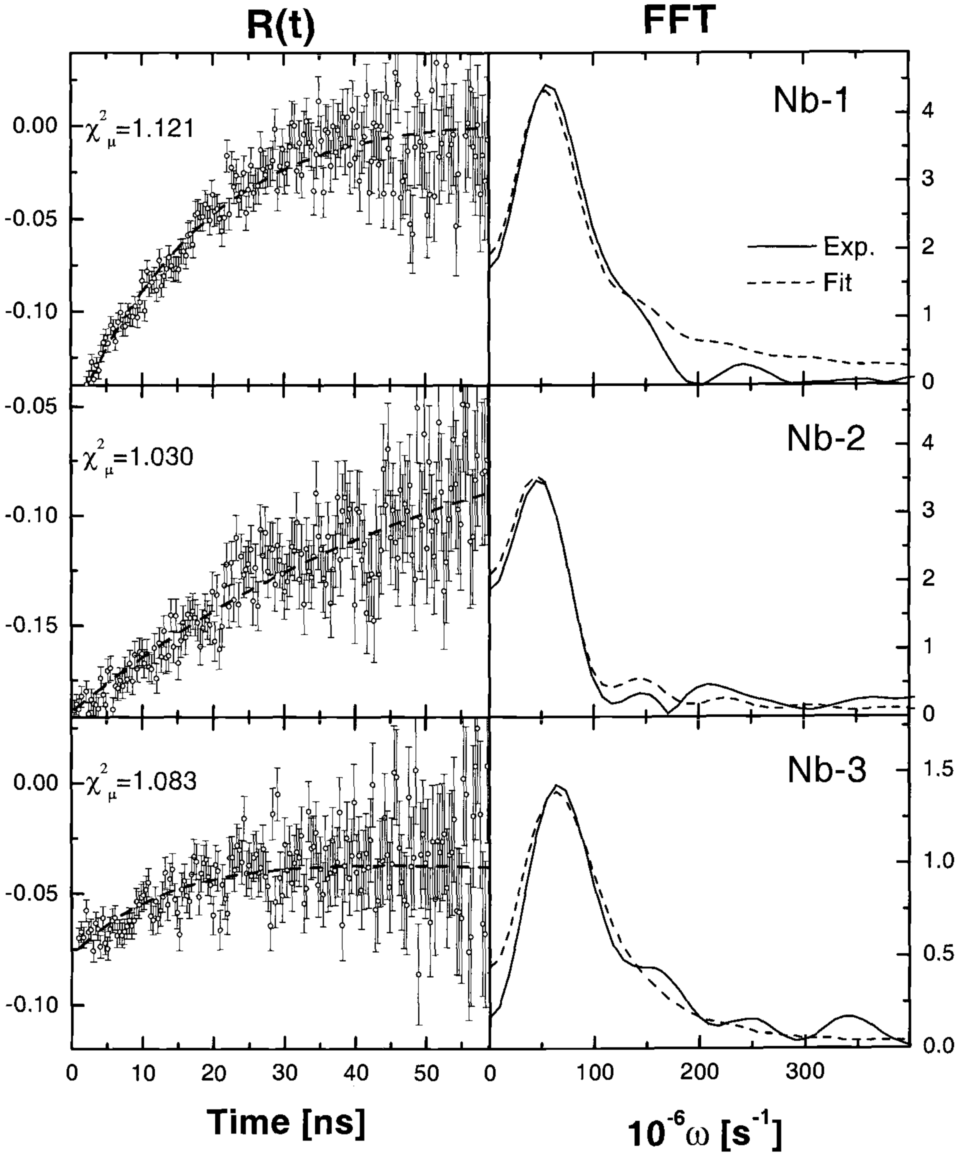

Figure 5.6: PAC time spectra and Fourier transforms of Hf-doped Niobium metal. Samples Nb-1, Nb-2 and Nb-3.

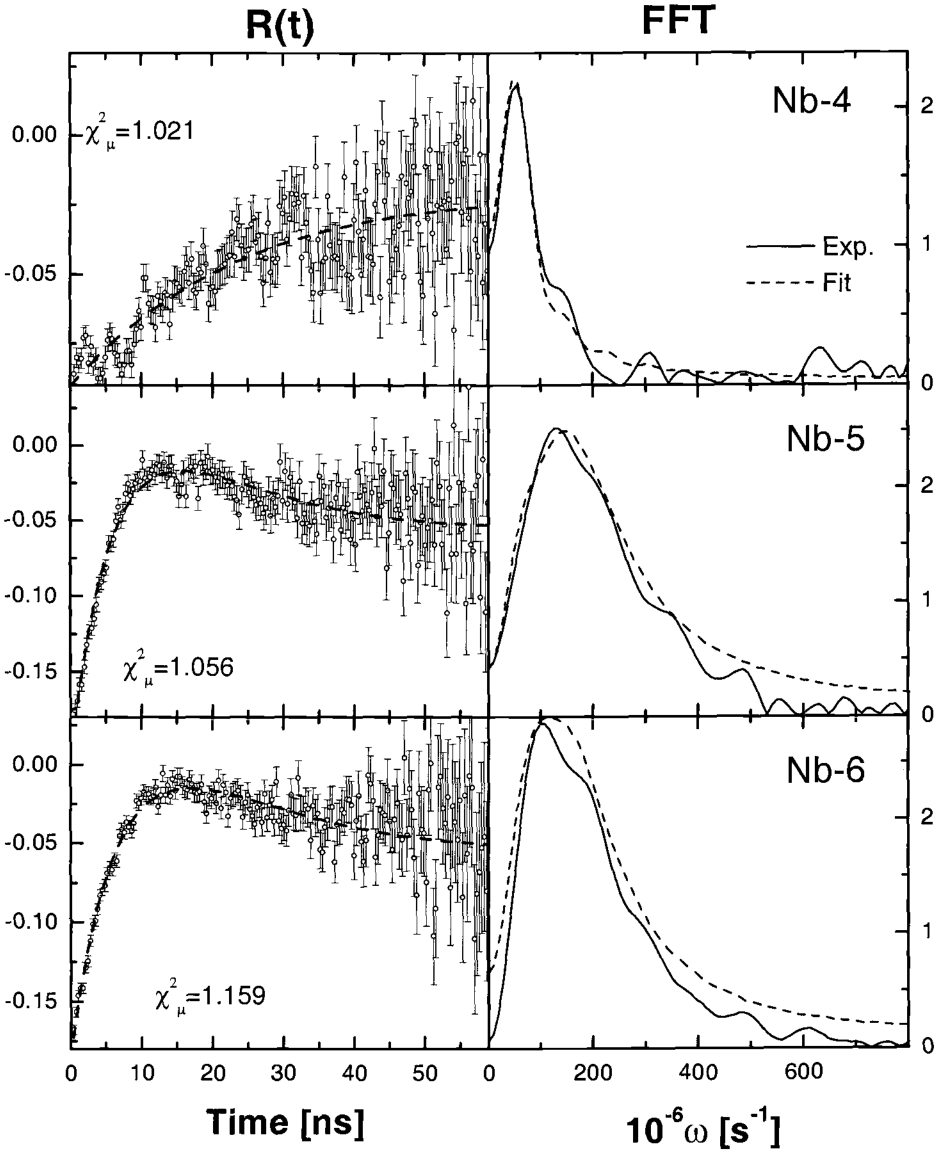

Figure 5.7: PAC time spectra and Fourier transforms of Hf-doped Niobium metal. Samples Nb-3, Nb-4 and Nb-6.

Sample	at.% impur.	A_{22}	ω_Q^{fit} (Mrad/s)	history
Nb-1	0.84	0.163(2)	5.54(1)	CW
Nb-2	0.84	0.174(3)	4.49(2)	AN
Nb-3	1.58	0.066(1)	7.14(2)	CW
Nb-4	1.58	0.081(1)	6.16(1)	AN
Nb-5	8.40	0.191(4)	15.4(2)	CW
Nb-6	8.40	0.183(2)	12.4(2)	AN

Table 5.1: Impurity levels, history and fitting parameters derived with the SRDM for Hf-doped niobium metal.

be distributed on the lattice in many possible ways. As a consequence, there is a distribution of EFGs values, and the probe nuclei will experience different EFGs. The PAC spectrum is formed by a wide range of frequencies that results in a nonoscillatory behavior of the angular correlation function. The total EFG in stabilized zirconia has two components: a static component from the dopant ions in the lattice, and a fluctuating component due to the motion of oxygen vacancies. Anions vacancies are highly mobile in the fluorite structure, and the mobility of the oxygen vacancies gives rise to relaxation [47].

In order to apply the results of the SRDM, Eq. (5.8) needs to be modified to take into account the lattice relaxation. In the high temperature region ($T > 700°C$), and according to (2.91), Eq. (5.8) is transformed to

$$G_{22}(t) = e^{-\lambda_{20}t} f_0 + e^{-\lambda_1 t} f_1(t) + e^{-\lambda_2 t} f_2(t) + e^{-\lambda_3 t} f_3(t) \qquad (5.15)$$

For $I = 5/2$, the relaxation parameters are

$$\lambda_{20} = 100.8\langle {\omega_Q}^2 \rangle \tau_c \qquad (5.16)$$

$$\lambda_1 = 1.048\lambda_{20} \qquad (5.17)$$

$$\lambda_2 = 1.190\lambda_{20} \tag{5.18}$$

$$\lambda_3 = 1.429\lambda_{20} \tag{5.19}$$

where the coupling constant is

$$\langle \omega_Q^2 \rangle = \left\langle \left(\frac{eQV_{zz}}{4I(2I-1)\hbar} \right)^2 \left(\frac{\eta^2}{3} + 1 \right) \right\rangle \tag{5.20}$$

and the correlation time of the fluctuating EFG is

$$\tau_c = \frac{1}{\nu_0} \exp\left(\frac{\Delta E}{kT} \right) \tag{5.21}$$

where ν_0 is the attempt frequency, ΔE is the activation energy for a vacancy jump, and k is the Boltzmann constant.

In the low temperature regime ($T < 700°C$), Eq. (5.8) is modified to

$$G_{22}(t) = e^{-\lambda_c t}(f_0 + f_1(t) + f_2(t) + f_3(t)) \tag{5.22}$$

More details about the derivation of the above equations and constants can be found in [47, 17]. What is relevant to the present discussion is the fact that in order to fit the PAC time spectra, when relaxation is present, it is necessary to include an extra parameter in the fitting function.

PAC spectra for cubic zirconia, doped with 18 wt.% yttria and taken in the temperature range of 22 to 1450°C, were fitted with (5.15) and (5.22). Table 5.2 lists the main fitting parameters and, Figs. 5.8 and 5.9 show the time spectra and corresponding Fourier transforms.

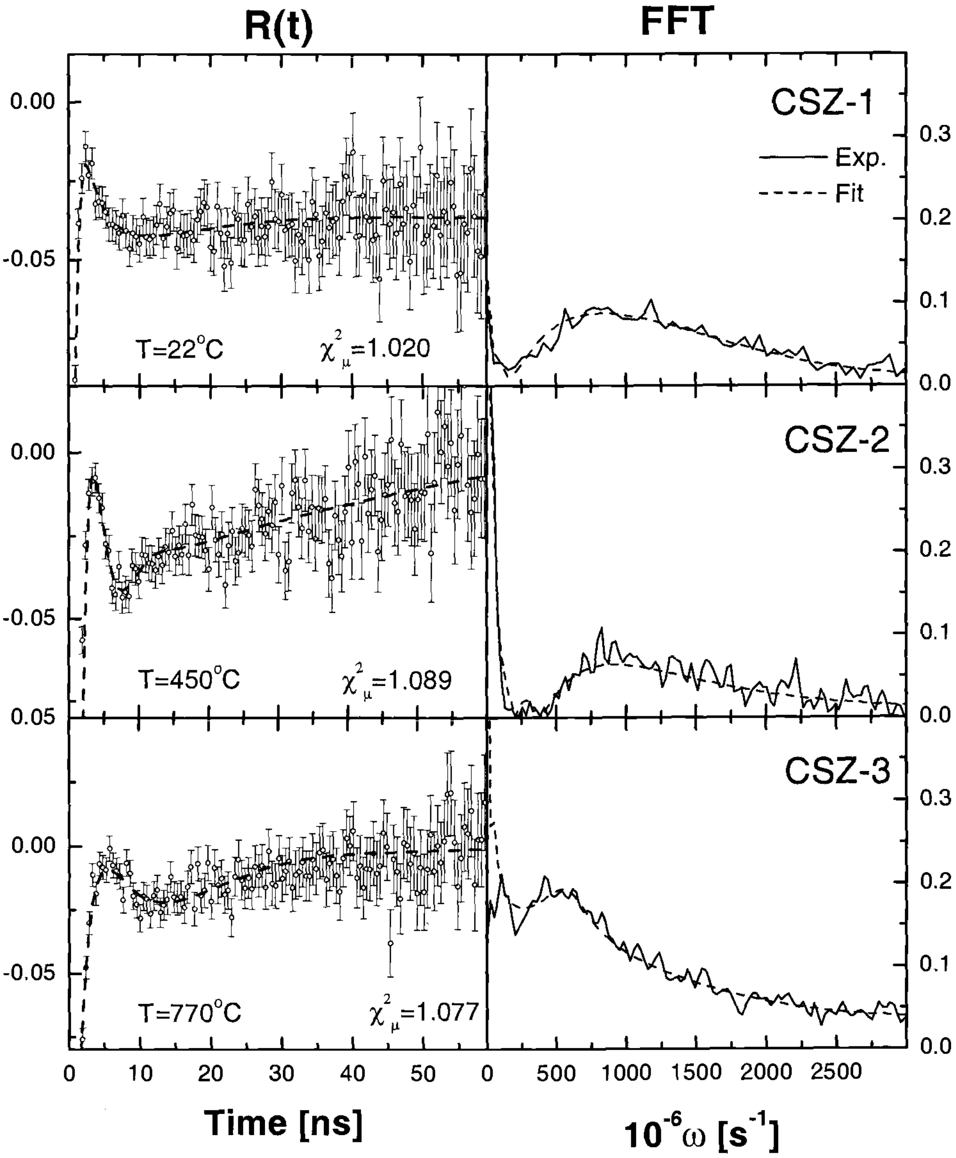

Figure 5.8: PAC time spectra and Fourier transforms of 18 wt.% yttria-doped zirconia: 22°, 450° and 750°C

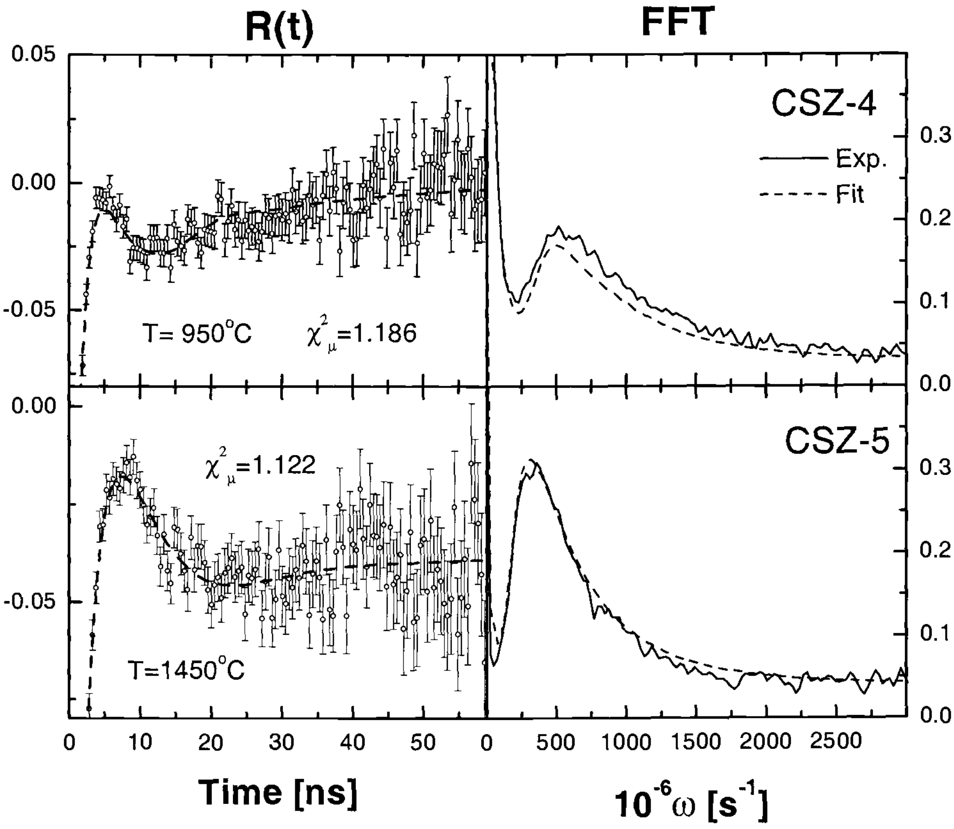

Figure 5.9: PAC time spectra and Fourier transforms of 18 wt.% yttria-doped zirconia: 950°C and 1470°C.

Sample	Temp. (°C)	A_{22}	ω_Q^{fit} (Mrad/s)	λ (Mrad/s)
CSZ-1	22	0.159(2)	112(8)	0.40(18)
CSZ-2	450	0.174(3)	186(12)	32(6)
CSZ-3	770	0.156(21)	70(4)	110(13)
CSZ-4	950	0.171(2)	53(6)	68(3)
CSZ-5	1470	0.173(2)	38(6)	2.3(7)

Table 5.2: Parameters used to fit cubic stabilized zirconia PAC spectra. $\lambda = \lambda_{20}$ for T> 700°C and $\lambda = \lambda_c$ for T< 700°C.

5.3 AXIAL MATERIALS, $\gamma > 0$

For axial materials, the distributions of $|V_{zz}|$, η and ω_n as well as the perturbation functions $G_{22}(t)$ are described as functions of the parameter γ. The value of γ is small for the more defective materials and large for the purer ones. Since the main purpose of this work is to simulate dilute concentrations of defects, only values of $\gamma > 30$ are considered. Simulations to obtain distributions of EFGs were performed with $30 < \gamma < 2000$. Distributions of $|V_{zz}|$, η and ω_n for $\gamma = 30$ and 100 are shown in the Figs. 5.10-12. Fig. 5.13 depicts the perturbation function obtained from the simulations for $\gamma = 30, 100$ and 1000.

The distributions of $|V_{zz}|$ are asymmetric, but they can be well described by a Lorentzian. This asymmetry is also present in the distributions of ω_1. In order to compare the line shapes that result from the simulations, the distributions of ω_1 and ω_2 for $\gamma = 30$ are fitted with a Lorentzian and a Gaussian, as depicted in Fig. 5.13. It can be seen that the Lorentzian fits the simulated distributions better than the Gaussian. As γ increases, the distributions become narrower, and the shape of the ω_1 distribution approaches that of a Lorentzian more closely. The distributions of ω_2 and ω_3 are well fitted with a Lorentzian for any value of γ.

In the axial case, when only static defects are present, the perturbation function (5.8) becomes

$$G_{22}(t,\gamma) = f_0(\gamma) + f_1(t,\gamma) + f_2(t,\gamma) + f_3(t,\gamma) \tag{5.23}$$

with $f_0(\gamma) = f_1(0,\gamma) + f_2(0,\gamma) + f_3(0,\gamma)$.

The constituents $f_1(t,\gamma)$, $f_2(t,\gamma)$ and $f_3(t,\gamma)$ are also fitted with a function that has the form of (5.13) with the difference that now the free fitting parameters are a function of γ.

For each constituent, the fitting functions are

$$\begin{aligned} f_1(t,\gamma) &= a_0(\gamma)\cos[(a_1(\gamma)t)^{a_2(\gamma)}]\exp[-(a_3(\gamma)t)^{a_4}] \\ f_2(t,\gamma) &= b_0(\gamma)\cos[(b_1(\gamma)t)^{b_2(\gamma)}]\exp[-(b_3(\gamma)t)^{b_4}] \\ f_3(t,\gamma) &= c_0(\gamma)\cos[(c_1(\gamma)t)^{c_2(\gamma)}]\exp[-(c_3(\gamma)t)^{c_4}] \end{aligned} \tag{5.24}$$

The dependence of these parameters on γ is given in (5.25-27). The fits were made using a subroutine that allows the fitting of multiple data sets. It was found that the parameters a_4, b_4 and c_4 can be kept as constants.

$$\begin{aligned} a_0(\gamma) &= 0.371445 - 0.243666\gamma^{-1} + 0.821504\gamma^{-2} \\ a_1(\gamma) &= 6.0 - 2.20048\gamma^{-1} + 6.69009\gamma^{-2} \\ a_2(\gamma) &= 1.0 - 0.26855\gamma^{-1} - 0.554205\gamma^{-2} \\ a_3(\gamma) &= 4.14839\gamma^{-1} + 2.43967\gamma^{-2} \\ a_4 &= 0.950049 \end{aligned} \tag{5.25}$$

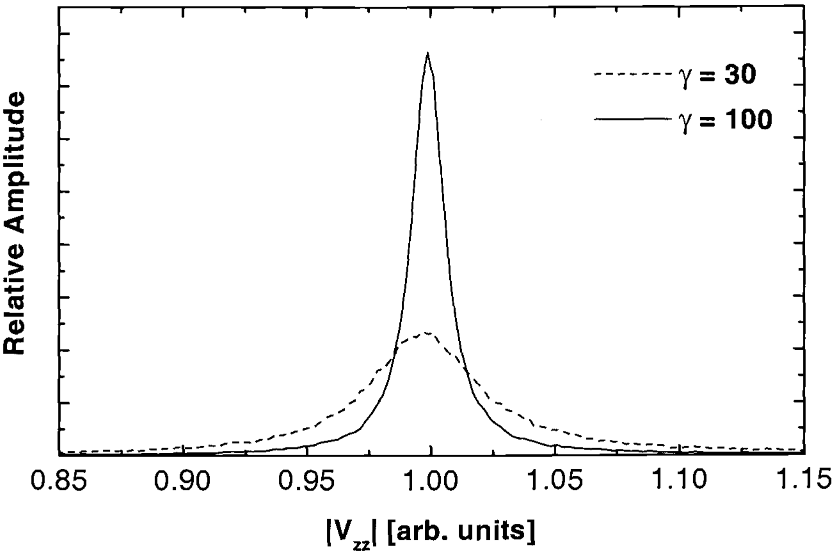

Figure 5.10: Distribution of the absolute values of V_{zz} for $\gamma = 30$ and 100.

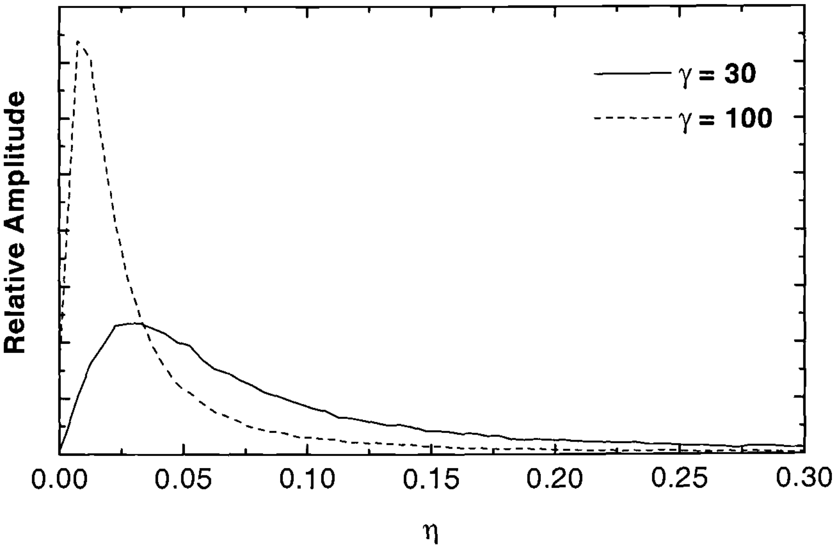

Figure 5.11: Distribution of the asymmetry parameter η for $\gamma = 30$ and 100.

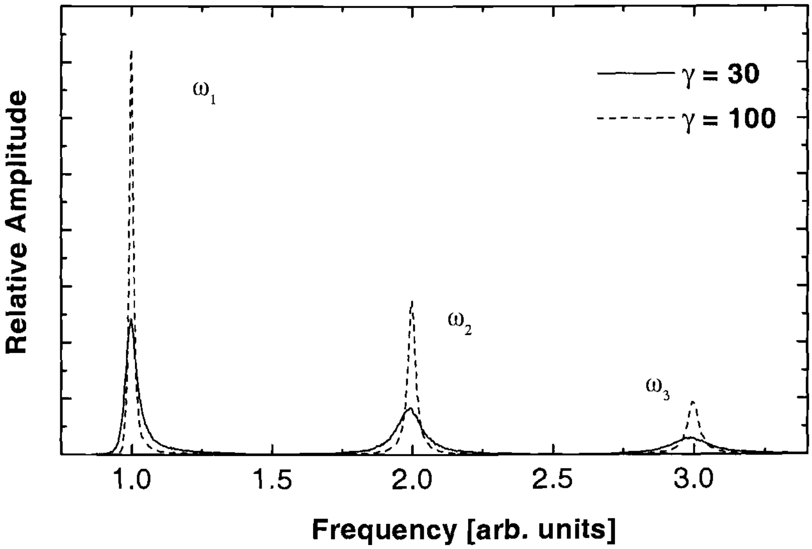

Figure 5.12: Distribution of transition frequencies for $\gamma = 30$ and 100.

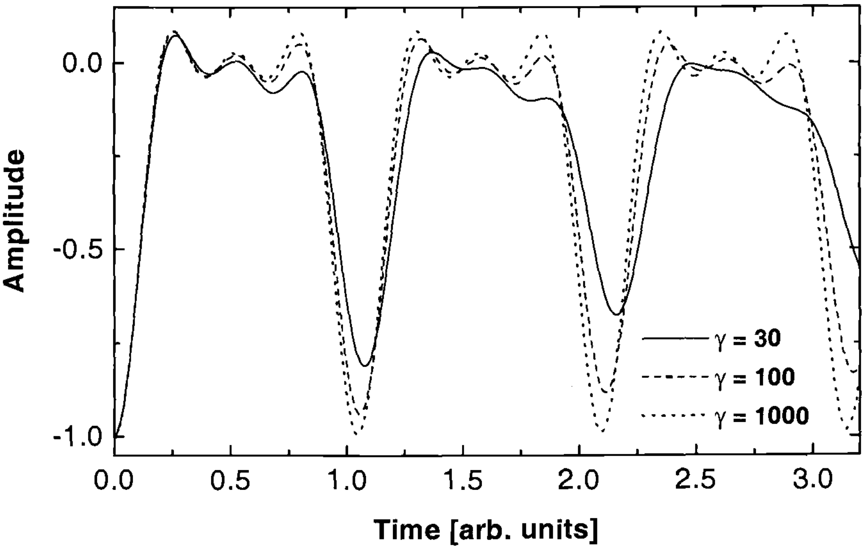

Figure 5.13: Simulated perturbation function $G_{22}(\gamma, t)$ for $\gamma = 30, 100$ and 1000.

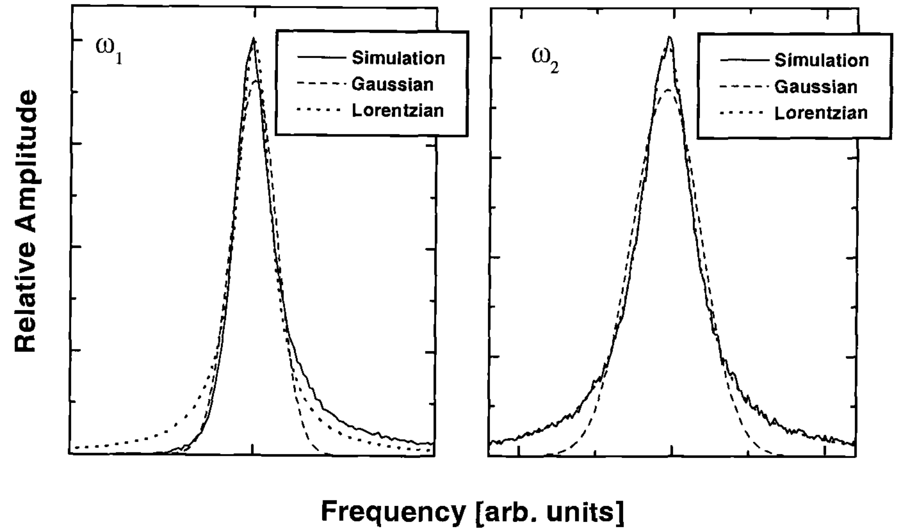

Figure 5.14: Distribution of ω_1 and ω_2, for $\gamma = 30$, fitted with a Lorentzian and a Gaussian.

$$\begin{aligned}
b_0(\gamma) =& 0.285715 - 0.00788611\gamma^{-1} + 0.0518714\gamma^{-2} \\
b_1(\gamma) =& 12.0 - 12.8274\gamma^{-1} + 8.12401\gamma^{-2} \\
b_2(\gamma) =& 1.0 + 0.000365646\gamma^{-1} - 0.334901\gamma^{-2} \\
b_3(\gamma) =& 9.56956\gamma^{-1} - 4.60644\gamma^{-2} \\
b_4 =& 0.984846
\end{aligned} \tag{5.26}$$

$$\begin{aligned}
c_0(\gamma) =& 0.14287 + 0.0334429\gamma^{-1} - 0.0769652\gamma^{-2} \\
c_1(\gamma) =& 18.0 - 18.5204\gamma^{-1} + 24.1541\gamma^{-2} \\
c_2(\gamma) =& 1.0 - 0.01056\gamma^{-1} - 1.21318\gamma^{-2} \\
c_3(\gamma) =& 13.1108\gamma^{-1} - 7.98248\gamma^{-2} \\
c_4 =& 1.024982
\end{aligned} \tag{5.27}$$

Zirconia with negligible vacancy concentrations can be made by doping with pentavalent Nb. In Nb-doped zirconia relaxation is suppressed completely [49]. Therefore, the PAC spectra is influenced only by the lattice EFG and by the distribution of charged defects around the probe sites.

In the present case, the SRDM fits the data with the parameters γ and ω_Q^{fit}. The results from these fits are compared with the commonly used static model (see Eq. 2.87), which is a heuristic representation of PAC spectra. When the static model is used, the fitting parameters are ω_1, ω_2, and δ. The asymmetry parameter η is calculated from the ratio ω_2/ω_1, and the value of ω_Q is calculated from (2.80). The parameters, δ, η and ω_Q, are the parameters from which one obtains information about the environment of a probe site. The SRDM model does not give these results directly. In order to compare the results of these two models, the perturbation functions derived from the numerical simulations, $G_{22}(t, \gamma)$, are fitted with the static model. As a result, for a given value of γ it is possible to assign a pair of values η and δ. In this way, a correspondence is established between these two models. Fig 5.15 shows how η and δ vary with γ.

It must be noted that the static model can produce fits with smaller values of χ^2_μ. This is expected since the SDRM model is more constrained than the static model; for the SRDM any value of γ is associated to a unique pair of values η and δ. The main objective of the SDRM is the unambiguous description of the effects of defects on the PAC spectra. Therefore, slightly larger values of χ^2_μ for the SDRM are not very significant in the present analysis.

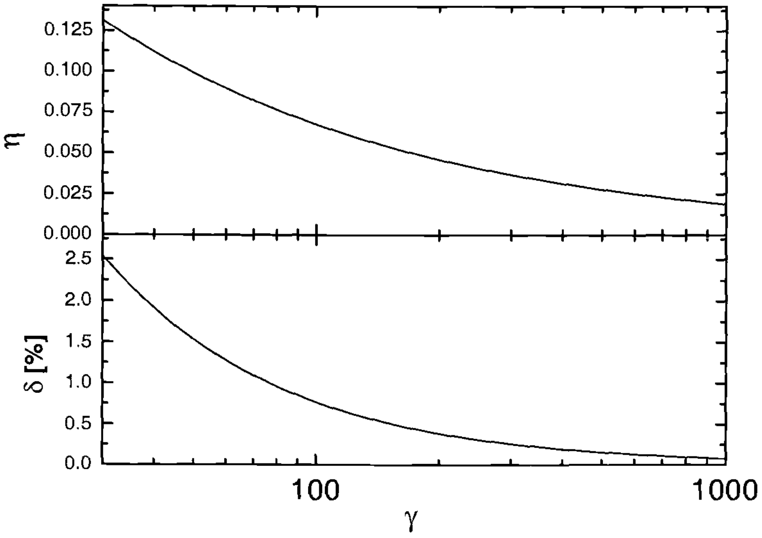

Figure 5.15: Asymmetry parameter η and line broadening δ as a function of γ.

PAC data on Nb-doped zirconia [50] were fitted with the SRDM and static models. Tables 5.3 and 5.4 list the values of the main fitting parameters for the static and SRDM models. The samples were doped with different quantities of Nb: TZA, 0.1 at.%; TZB, 0.2 at.%; TZC, 0.3 at.%; and TZC, 0.5 at.%. Fig. 5.16 shows typical fits of PAC spectra using the SDRM model.

5.4 DISCUSSION OF RESULTS

Using only the χ^2_μ criteria to define the quality of the fits made with the SRDM, one can say that the overall quality of the fits for cubic and tetragonal materials is very good. In the case of Nb-doped tetragonal zirconia, the comparison with the conventional static model shows that although the SRDM is more constrained, it can fit the data satisfactorily.

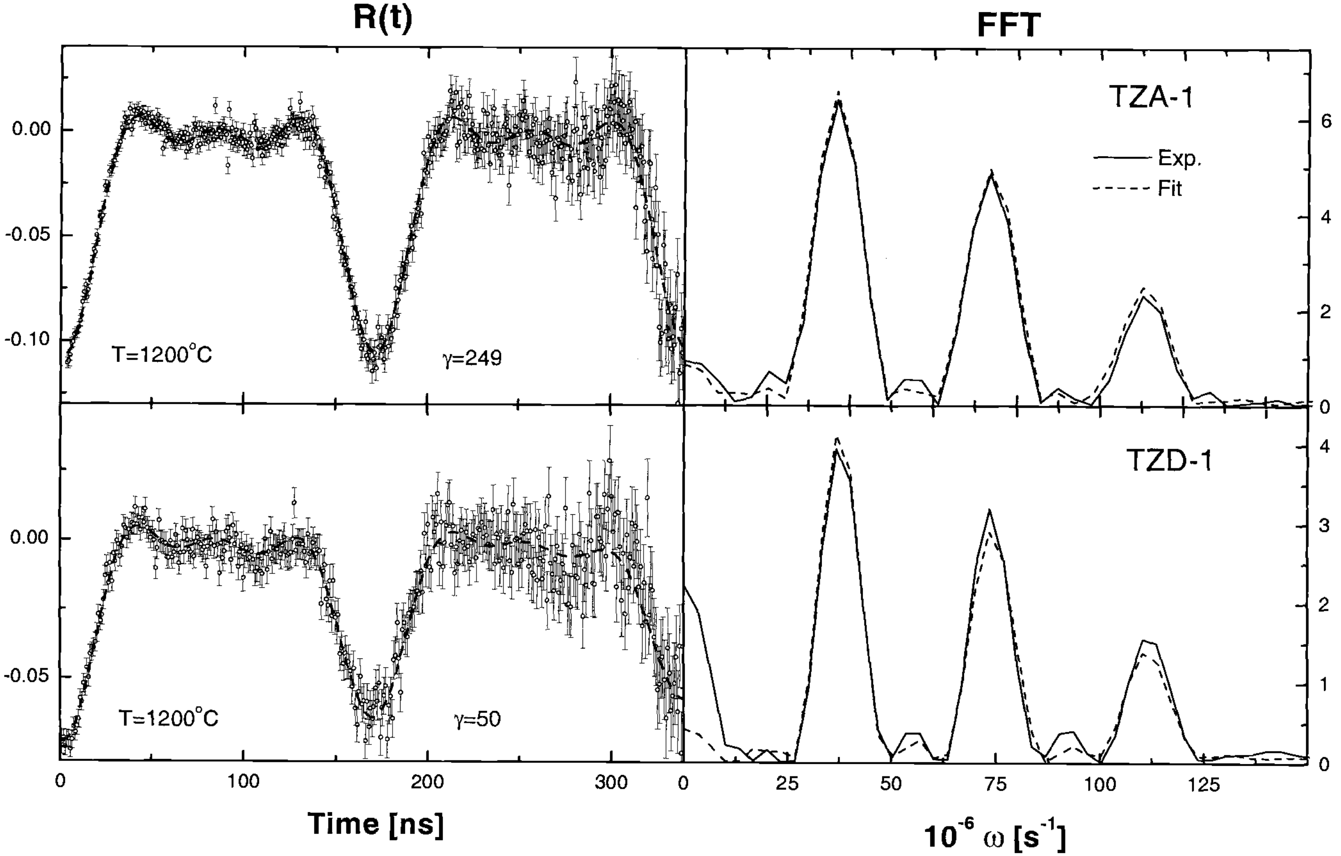

Figure 6.2: PAC time spectra and Fourier transforms for Nb-doped tetragonal zirconia fitted with the SRDM.

Sample	Temp. (°C)	γ	ω_Q^{fit} (Mrad/s)	η	δ (%)	χ^2_μ
TZA-1	1200	309(50)	6.178(4)	0.036(4)	0.25(4)	1.0139
TZA-2	1100	268(45)	6.229(5)	0.039(3)	0.28(4)	1.0632
TZA-3	1000	217(41)	6.262(3)	0.043(3)	0.35(5)	1.1387
TZA-4	1400	323(55)	6.081(2)	0.035(4)	0.24(4)	1.2090
TZA-5	950	193(36)	6.272(2)	0.041(2)	0.31(2)	1.1107
TZA-6	1293	240(62)	6.148(2)	0.042(6)	0.25(7)	1.030
TZB-1	1200	172(29)	6.210(2)	0.050(4)	0.45(6)	1.270
TZB-2	1100	326(100)	6.232(5)	0.035(8)	0.23(11)	1.1662
TZB-3	1000	168(65)	6.276(4)	0.051(8)	0.45(12)	1.1785
TZB-4	950	174(31)	6.306(4)	0.050(6)	0.45(8)	1.1785
TZC-1	1200	119(16)	6.244(4)	0.062(4)	0.65(8)	1.0562
TZC-2	1100	100(10)	6.270(3)	0.068(4)	0.77(8)	1.0656
TZC-3	1000	81(12)	6.307(4)	0.075(5)	0.95(9)	1.0433
TZC-4	900	92(18)	6.312(2)	0.070(8)	0.83(13)	1.1020
TZD-1	1200	51(5)	6.314(3)	0.098(7)	1.50(12)	0.9824
TZD-2	1100	48(5)	6.320(3)	0.101(2)	1.60(12)	1.0013
TZD-3	1000	50(5)	6.354(4)	0.099(3)	1.50(12)	1.1293
TZD-4	950	50(6)	6.400(3)	0.099(2)	1.50(14)	1.1157
TZD-5	920	47(5)	6.407(4)	0.102(3)	1.63(12)	1.0359

Table 5.3: Fitting parameters γ and ω_Q^{fit} obtained by fitting Nb-doped t-ZrO_2 with the SRDM model and the corresponding values of η and δ.

Sample	Temp. (°C)	ω_Q^{fit} (Mrad/s)	η	δ (%)	χ^2_μ
TZA-1	1200	6.137(4)	0.063(8)	0.33(5)	1.0012
TZA-2	1100	6.210(5)	0.066(10)	0.34(2)	1.0642
TZA-3	1000	6.232(3)	0.068(9)	0.37(4)	1.0494
TZA-4	1400	6.071(2)	0.048(10)	0.29(2)	1.0699
TZA-5	950	6.245(2)	0.077(12)	0.43(3)	1.0018
TZA-6	1293	6.097(7)	0.052(9)	0.28(3)	1.0314
TZB-1	1200	6.170(2)	0.074(9)	0.34(3)	1.2743
TZB-2	1100	6.201(6)	0.100(9)	0.41(4)	1.1151
TZB-3	1000	6.236(12)	0.088(6)	0.39(6)	1.1183
TZB-4	950	6.266(4)	0.093(9)	0.61(8)	1.2230
TZC-1	1200	6.167(5)	0.115(12)	0.92(13)	1.0475
TZC-2	1100	6.209(4)	0.106(9)	0.99(10)	1.0631
TZC-3	1000	6.216(3)	0.141(11)	1.15(10)	1.0217
TZC-4	900	6.232(2)	0.156(12)	1.96(9)	1.0942
TZD-1	1200	6.278(1)	0.162(15)	2.01(12)	0.9132
TZD-2	1100	6.300(6)	0.157(14)	1.82(14)	1.0013
TZD-3	1000	6.321(3)	0.166(11)	1.83(11)	1.1215
TZD-4	950	6.354(4)	0.185(12)	1.95(16)	1.1236
TZD-5	920	6.360(6)	0.180(13)	2.01(13)	1.0164

Table 5.4: Fitting parameters ω_Q^{fit}, η and δ obtained by fitting Nb-doped t-ZrO_2 with the static model.

For cubic materials, the results obtained are particularly interesting. The SRDM suggests that random distributions of charges can reproduce non-zero EFGs, and the broad asymmetric distributions of $|V_{zz}|$ observed experimentally. A point charge model (PCM) [75] has been developed to explain the distributions of EFGs in perovskite compounds with cubic symmetry [76]. The distribution of EFGs in these materials is the result of trapped oxygen vacancies in the cubic lattice. The results obtained by the PCM are similar in nature to what is simulated by the SRDM: non-zero EFG in a material with cubic symmetry, and broad asymmetric $|V_{zz}|$ distributions. The shapes of the distributions modeled by the PCM are slightly different from the ones obtained by the SRDM. The PCM requires an exact knowledge of trapped oxygen vacancies, their distribution, etc.

Although the quality of the fits for Nb-doped tetragonal zirconia is satisfactory (compare Tables 5.3 and 5.4), there are noticeable discrepancies between the results given by the SRDM and the static model. Fig. 5.17 depicts the values of η and δ found by fitting the PAC spectra with both models. The values of η and δ found with the SRDM are smaller than those found with the static model. Fig. 5.18 shows the temperature dependence of the parameter ω_Q^{fit} for the sample TZA as calculated from the fits using both models. The decrease of ω_Q^{fit} with increasing temperature is expected, due to lattice thermal expansion, which results in a decrease of the lattice EFG. Data fitted with both models show this weak temperature dependence of ω_Q^{fit}, but there is a consistent difference between the values of ω_Q^{fit} obtained with the SRDM and static models, with the values given by the SRDM always being larger.

These differences can be explained, in part, by the fact that in order to fit the data in the best possible way, the SRDM compensates the smaller values of η with larger values of ω_Q^{fit}. The distribution of ω_1 for the SRDM is not symmetric, and this can also affect the calculation of the asymmetry parameter η.

To understand better the dependence of the parameters η and δ on γ, a series of numerical experiments were performed. These experiments consisted of fitting the perturbation functions derived from the numerical simulations, $G_{22}(t, \gamma)$, when noise and error bars are added to them. These artificially generated PAC time spectra were fitted with the static model. It was found that the values of η and δ and even ω_Q derived in this way are dependent on the noise level and size of error bars. This observation brings into question the validity of the static model for fitting PAC experimental data measured in a laboratory. This is a serious question that needs considerably more work to understand fully. For purposes of this thesis the observation implies that one cannot determine unambiguously any relationship between the γ, ω_Q parameters of the SRDM and the η, δ, and ω_Q parameters of the static model.

On the other hand, the SRDM suggests that the use of a Lorentzian line profile can be justified in certain cases. The SRDM also shows that the asymmetric line profiles should be investigated.

The influence of defects on PAC spectra still can be determined by experimental methods. Fig. 5.17 shows that it is possible to derive an empirical formula that describes the relation η vs. δ for materials with a dilute concentration of defects. To avoid any ambiguity in the interpretation of the data, the results obtained with the conventional static model are used. The Nb-doped tetragonal zirconia data used in this work are of very good quality, and the PAC spectra obtained from these samples are free of most experimental artifacts [52, 50]. Therefore, results derived from their analysis are reliable.

Using the values of η and δ found with the static model one obtains a formula that describes the relation between η and δ:

$$\eta = 0.12(3) \times \delta(\%)^{0.51(2)} \tag{5.28}$$

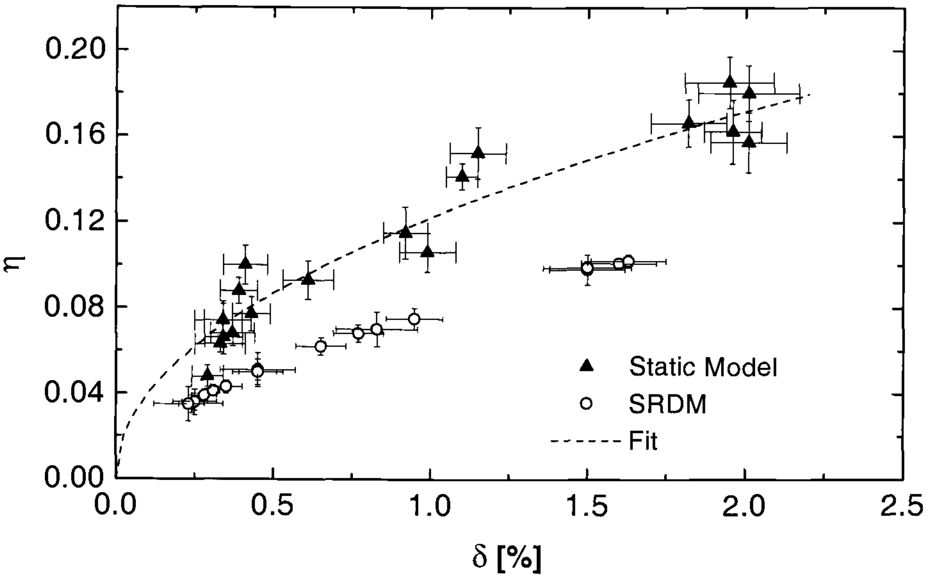

Figure 5.17: Relation between η and δ obtained by fitting Nb-doped tetragonal zirconia PAC spectra with the SRDM and static models. The fit is an experimental derivation of the η vs. δ relation.

Also, another important result can be obtained from the results listed in Table 5.3 and shown in Fig. 5.18. In weakly Nb-doped t-ZrO_2, the observed quadrupole interaction frequency ω_Q^{fit} is the quadrupole interaction frequency of the vacancy-free lattice [50]. The temperature dependence of ω_Q^{fit} is given by:

$$\omega_Q(T) = 6.63(2) Mrad/s - 4.03(5) \times 10^{-4} Mrad/(s°C) \times T \tag{5.29}$$

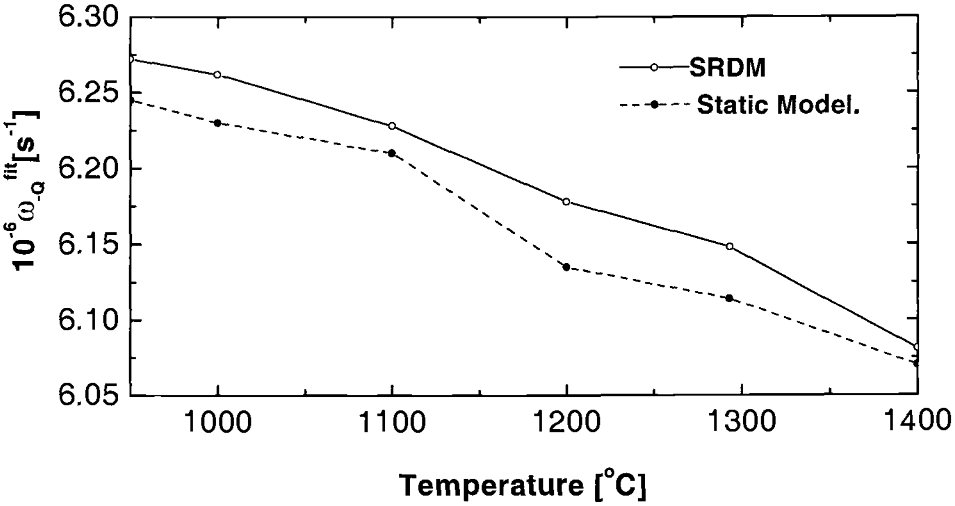

Figure 5.18: Fitting parameter ω_Q^{fit} as a function of the temperature. Sample TZA.

These results are used in the next chapter to quantify the presence of static defects in zirconia ceramics where oxygen vacancies are known to be present.

6 DYNAMIC DEFECTS

Among the important properties of zirconia is its ionic conductivity at high temperatures. At $T > 1000°C$, yttria-doped zirconia becomes an excellent ionic conductor as a result of the high mobility of oxygen vacancies. The ionic conductivity in zirconia at high temperature has many technological applications such as solid electrolytes in fuel cells and oxygen sensors. [77].

In PAC is particularly useful in the study of dynamics of oxygen vacancies in zirconia. In the zirconia lattice, ^{111}Cd has an effective charge of -2, and attracts oxygen vacancies that have an effective charge of $+2$. The PAC probe can trap the vacancy, and their mutual interaction serves as a means to obtain information about the dynamics of oxygen vacancies.

A vacancy can be trapped at and detrap from a PAC probe nucleus. Also, when trapped, a vacancy can hop between equivalent sites around the probe nucleus. The angular correlation of the emission of γ rays by the PAC probe is affected by the fluctuating EFG produced by the moving vacancy. These time-dependent interactions will produce relaxation and damping of the PAC time spectra.

Several stochastic models have been developed [22, 24, 26, 21, 18] to calculate the effects of fluctuating fields on the perturbation function $G_{22}(t)$. A model, whose results can be directly applied to tetragonal zirconia at temperatures between 900 and 1300°C [29], is used in this work to obtain physical quantities of interest. The main characteristics of this model are presented in the next section.

6.1 STOCHASTIC MODEL FOR VACANCY MOTION

This is a physically-motivated four-state model that consists of three trapped states with equivalent axially-symmetric EFGs of mutually orthogonal orientations (x, y and z directions), and a detrapped state with a weaker axially-symmetric EFG whose symmetry axis is oriented along the diagonal between the three trapped EFGs. It corresponds to a cubic structure with the nuclear probe at the center of the cube with the vacancy hopping around the nearest eight lattice positions. The 24 second-neighbor traps are not considered, as experimental evidence shows that oxygen vacancies are trapped in a first neighbor trap by the probe nucleus, ^{111}Cd [50]. The model is based on the families of $XYZS$ models [26] developed to calculate the effects of time-dependent EFGs on the PAC spectra.

This model depends on four parameters: w, the rate a trapped vacancy hops around a probe; w_d, the detrapping rate; w_t, the trapping rate; and γ_s, the ratio of the EFG in the detrapped state (essentially the tetragonal lattice EFG) to the EFG due to a single vacancy in a trap near the probe nucleus. At high temperatures, a vacancy can be trapped, hop among equivalent trap sites and detrap many times during the probe nucleus intermediate state lifetime.

It has been shown that relaxation caused by hopping trapped oxygen vacancies is negligible above 600°C [78]. This implies that the hopping parameter, w, is very large compared to the quadrupole frequency of the static trapped state, ω_Q, and other transition rates. Also, it has been determined that the average detrapping time for oxygen vacancies in tetragonal zirconia at 1200°C is less than or of order 2 ns [78]. With these results, an expression for the perturbation function has been calculated with the following conditions: $w/\omega_Q \geq 200$, $w_d/\omega_Q \approx 30-80$, and $w_t/w_d \approx 0.1-3$. The perturbation function is given by

$$
\begin{aligned}
G_{22}(t) = 0.184e^{-\lambda_0 t} + 0.016e^{-\lambda_0' t} + \frac{13}{35}e^{-\lambda_1 t}\frac{\cos(\omega_1' t + \phi_1)}{\cos(\phi_1)} \\
+ \frac{2}{7}e^{-\lambda_2 t}\frac{\cos(\omega_2' t + \phi_2)}{\cos(\phi_2)} + \frac{1}{7}e^{-\lambda_3 t}\frac{\cos(\omega_3' t + \phi_3)}{\cos(\phi_3)}
\end{aligned}
\tag{6.1}
$$

where

$$
\begin{aligned}
&\omega_n' = \omega_n \frac{w_d}{w_d + 3w_t}, \qquad \omega_n = 6n\omega_{Qs}, \qquad \gamma_s = \frac{\omega_{Qs}}{\omega_Q} \\
&\lambda_n = A_n \left(\frac{\omega_{Qs}}{\gamma_s}\right)^2 \frac{w_t}{w(w_d + 3w_t)} + 3(1-\gamma_s)^2 \omega_n^2 \frac{w_d w_t}{(w_d + 3w_t)^3} \\
&\lambda_0' \approx 2\lambda_0 \\
&A_0 = 110, \qquad A_1 = 110, \qquad A_2 = 120, \qquad A_3 = 90 \\
&\phi_1 \approx 25.0\frac{w_t \omega_{Qs}}{w w_d \gamma_s}, \qquad \phi_2 \approx -21.4\frac{w_t \omega_{Qs}}{w w_d \gamma_s}, \qquad \phi_3 \approx -59.4\frac{w_t \omega_{Qs}}{w w_d \gamma_s}
\end{aligned}
\tag{6.2}
$$

This expression can only be used in the range of temperatures specified above, and it is not valid for slower transition rates. It describes time-dependent EFGs fluctuations around a probe nucleus in a tetragonal lattice site free of static defects. The transition frequencies ω_n and the S_{kn} coefficients in (6.1) refer to the situation where the EFG at the probe site is axial ($\eta = 0$). In this model, the spatial concentration of oxygen vacancies is considered to be uniform.

In order to apply (6.1) when static defects are present, this expression must be modified so that changes in the local EFG, described by the asymmetry parameter η and the line broadening δ, are also included in the perturbation function. In Eq. (6.1) ω_{Qs} is substituted by Eq. (5.29) so that temperature effects on the lattice quadrupole interaction frequency are accounted for. Also, the line broadening caused by static defects is included in (6.1) with (5.29).

The transition frequencies ω_n and the S_{kn} coefficients are explicitly defined as functions of η.

With these modifications (6.1) becomes

$$\begin{aligned} G_{22}(t,\eta) = \frac{0.184}{0.2} S_{20}(\eta) e^{-\lambda_0 t} + \frac{0.016}{0.2} S_{20}(\eta) e^{-\lambda_0' t} \\ + \sum_{n=1}^{3} S_{2n}(\eta) e^{-(\lambda_n(\eta)+\delta\omega_n(\eta))t} \frac{\cos(\omega_n'(\eta)t + \phi_n)}{\cos(\phi_n)} \end{aligned} \tag{6.3}$$

Assuming that the fluctuating EFG in the zirconia ceramic is caused by thermally activated dynamic processes, then the hopping, trapping and detrapping rates follow an Arrhenius behavior. These rates are given by

$$\begin{aligned} w &= w_0 e^{-E_h/kT} \\ w_d &= w_{d0} e^{-E_d/kT} \\ w_t &= w_{t0} e^{-E_t/kT} \end{aligned} \tag{6.4}$$

where E_h, E_t and E_d are the hopping barrier between equivalent trap sites, the trapping and detrapping energy barriers, respectively; the prefactor $w_0 \sim \nu_0$, where ν_0 is the phonon frequency ($10^{13} - 10^{14} s^{-1}$); $w_{d0} = g_d \nu_0$, where g_d is a geometrical factor of order 1 that describes the ways a vacancy can detrap; and, $w_{t0} = g_t [V_O] n \nu_0$ where g_t is a geometrical factor of order 1 that describes the ways a vacancy can trap, n is the number of trapping positions, and $[V_O]$ is the oxygen vacancy concentration. The activation energies are independent of the sample. Also, the prefactors of the hopping and detrapping rates should be the same for every sample. Only the trapping rate varies from sample to sample as it is dependent on the oxygen vacancy concentration. Fig. 6.1 shows the relative energies needed for these processes. It is assumed that the prefactors do not change significantly with temperature.

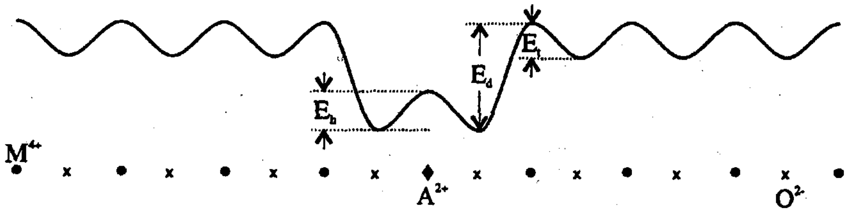

Figure 6.1: Hopping energies in a crystal. The periodic potential in a crystal is perturbed by the presence of a dopant. A lower-valence dopant is represented by A, in the center location. An oxygen vacancy moves between equivalent positions on the crystal until it crosses the hopping barrier E_t and becomes trapped. The vacancy can hop between equivalent trap sites if it posses hopping energy E_h. To escape or detrap, an oxygen vacancy must overcome a large energy barrier E_d [40].

6.2 YTTRIA-DOPED ZIRCONIA

Previous PAC studies on zirconia have been hindered by the inability to make reproducible samples of controlled oxygen vacancy concentrations and uniform distribution of oxygen vacancies. The data used in this work are the results of PAC measurements of high-quality Y-doped zirconia samples [52].

Data from two yttria-doped zirconia samples are used here. Fifteen PAC spectra for the sample TZYA (0.1 at.% Y) were collected in the temperature range of 1000 to 1300°C. For the sample TZYB (0.2 at%. Y), eighteen PAC spectra were collected in the temperature range of 1000 to 1350°C.

Trivalent dopants like yttrium introduce half a vacancy for every yttrium doped. At the 0.1 at.% and 0.2 at.% doping level, a sample contains 250 ppm and 500 ppm of oxygen vacancies to charge compensate for the yttrium, respectively. Also, oxygen vacancies are introduced due to impurities. The concentration of thermally generated vacancies is negligible in comparison with extrinsic vacancies, since the formation energy for intrinsic oxygen vacancies is relatively high at 5 eV [79]. The concentration of vacancies is determined by the introduction of dopants and impurities.

The oxygen vacancies in yttria-doped zirconia jump freely in the anionic sublattice in the crystal when not associated with ^{111}Cd probes. The association energy for the yttrium-oxygen vacancy pair is about 0.3 eV . The trapping probability of vacancies around trivalent yttrium is small for T > 1000°C [80]. Also, the probe nucleus can only trap one vacancy at a time since it is energetically unfavorable to trap two or more vacancies into the same system at the same time [49].

6.3 DATA FITTING

The main purpose in the analysis of Y-doped zirconia data is to obtain the values related to the dynamics of the oxygen vacancies: the hopping, trapping and detrapping energies.

With the large number of spectra taken at different temperatures, the data set is best fitted with a subroutine that fits multiple spectra simultaneously [57]. The experimental counting ratio, $R(t) = A_{22}G_{22}(t)$, is fitted with (6.3), and the hopping, trapping and detrapping rates given by (6.4).

The spectra are fitted simultaneously with nine fitting parameters: the anisotropy A_{22}; the asymmetry parameter η; the energies E_h, E_d and E_t; the prefactors w_0, w_{d0}, and w_{t0}; and the ratio between lattice and fluctuating

EFGs γ_s. With so many free parameters, the multiple spectra data fitting is rather complicated. Some constraints are introduced and then relaxed in order to make the fitting converge. The values of A_{22} do not vary significantly for a sample. At first it can be assumed to be a constant for all the spectra, and once the multiple fits start to converge, it is allowed to vary freely. An initial value of the asymmetry parameter η can be estimated from the Fourier transform of the raw data. Previous work on ytrria-stabilized zirconia [47] found values for activation energies in the order of 1.0 eV. More recently [50], it was determined that oxygen vacancies are trapped at first-neighbor positions to Cd with binding energy 0.62(3) eV. These data suggest that the following constraints can be used in the fittings: $E_d - E_t \sim 0.62$ eV, and $E_t \sim 1.0$ eV. Also, it is reasonable to assume $E_t \sim E_h$. The value of γ_s was kept constant at 0.5 at the beginning of the fits.

Table 6.1 lists the dynamical parameters determined by the fits. Figs. 6.2-5 show PAC time spectra and their Fourier transforms for samples TZYA and TZYB and fits made using (6.3). The observed quadrupole interaction frequencies for the samples TZYA and TZYB are shown in Fiq. 6.6.

Sample	E_h (eV) w_0 (rad/s)	E_d (eV) w_{d0} (rad/s)	E_t (eV) w_{t0} (rad/s)
TZYA	0.91(6) $15(3) \times 10^{13}$	1.54(8) $13.2(6) \times 10^{13}$	0.96(7) $2.1(7) \times 10^{11}$
TZYB	0.86(7) $12(3) \times 10^{13}$	1.49(7) $14.5(5) \times 10^{13}$	0.95(8) $3.6(8) \times 10^{11}$

Table 6.1: Dynamical parameters derived from the fitting of 0.1 and 0.2 at.% Y-doped zirconia PAC spectra.

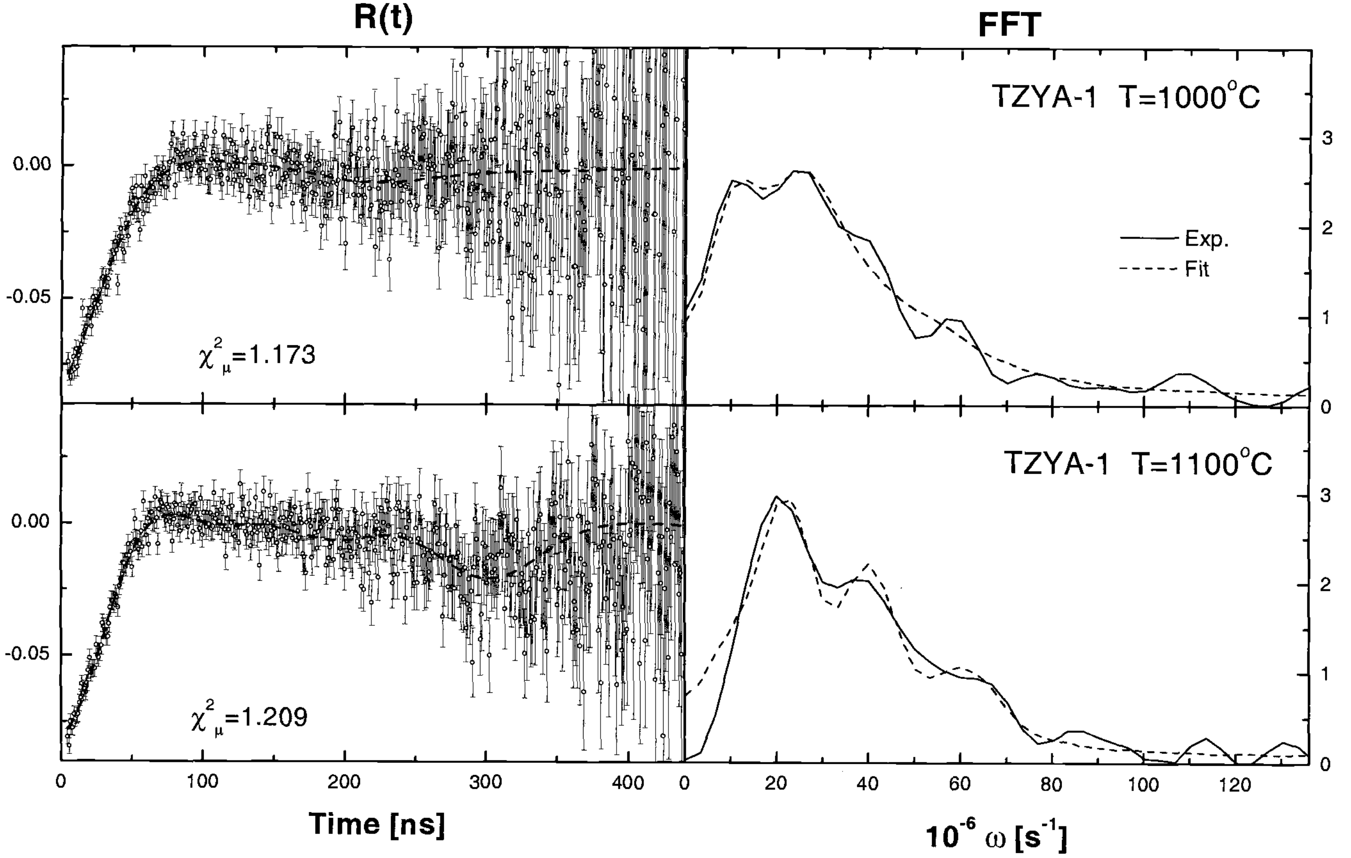

Figure 6.2: PAC time spectra and Fourier transforms for 0.1 at.% Y-doped tetragonal zirconia and fits. Sample TZYA at 1000 and 1100°C.

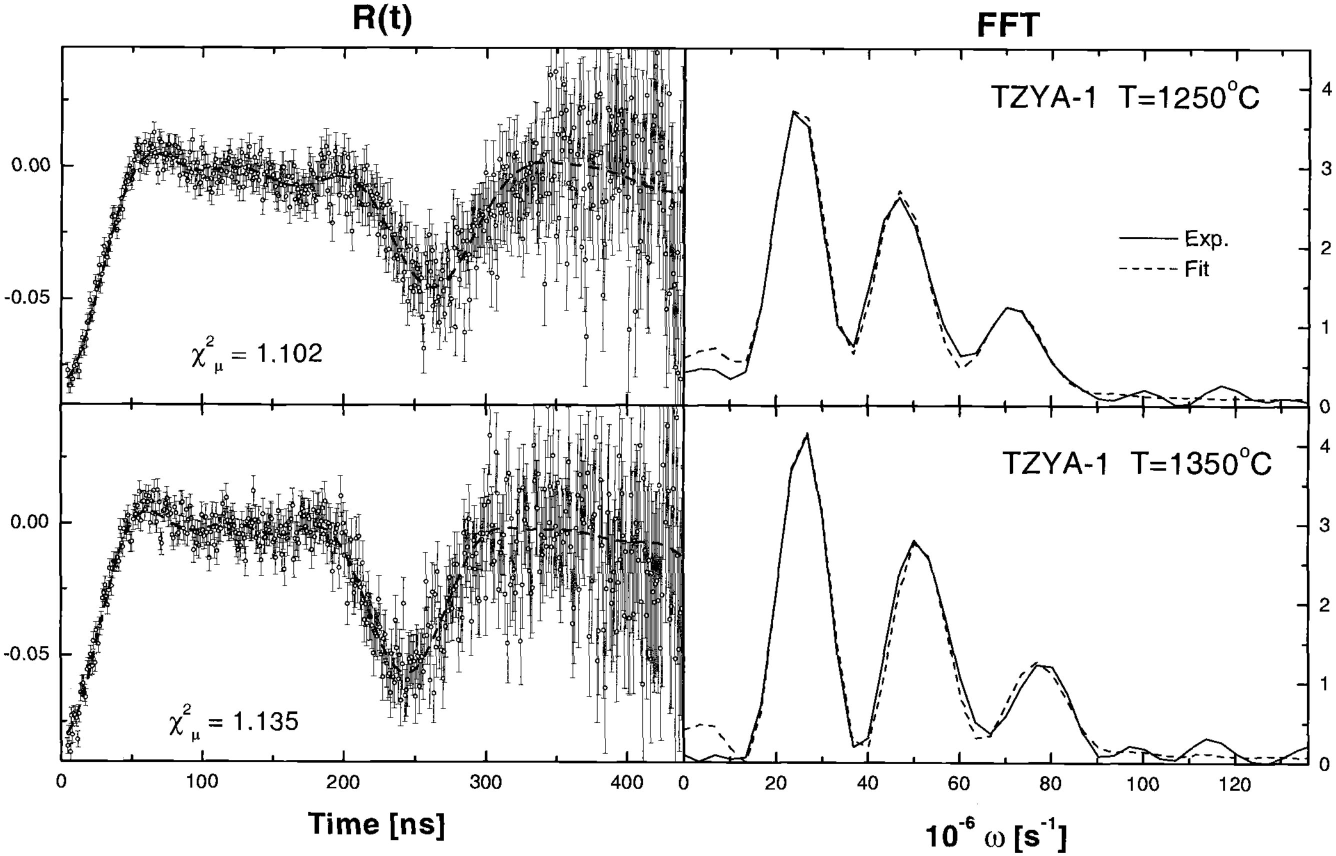

Figure 6.3: PAC time spectra and Fourier transforms for 0.1 at.% Y-doped tetragonal zirconia and fits. Sample TZYA at 1250 and 1350°C.

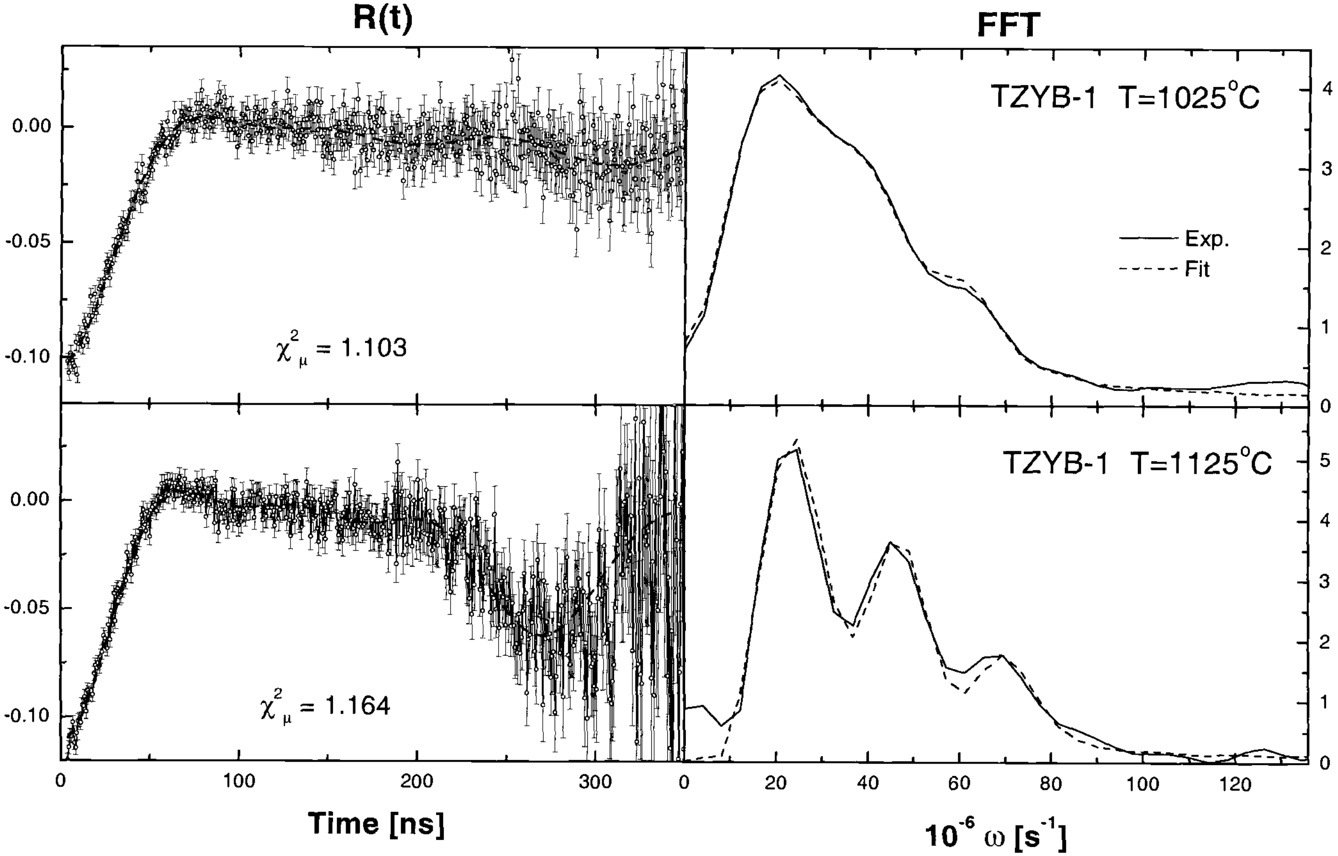

Figure 6.4: PAC time spectra and Fourier transforms for 0.2 at.% Y-doped tetragonal zirconia and fits. Sample TZYB at 1025 and 1125°C.

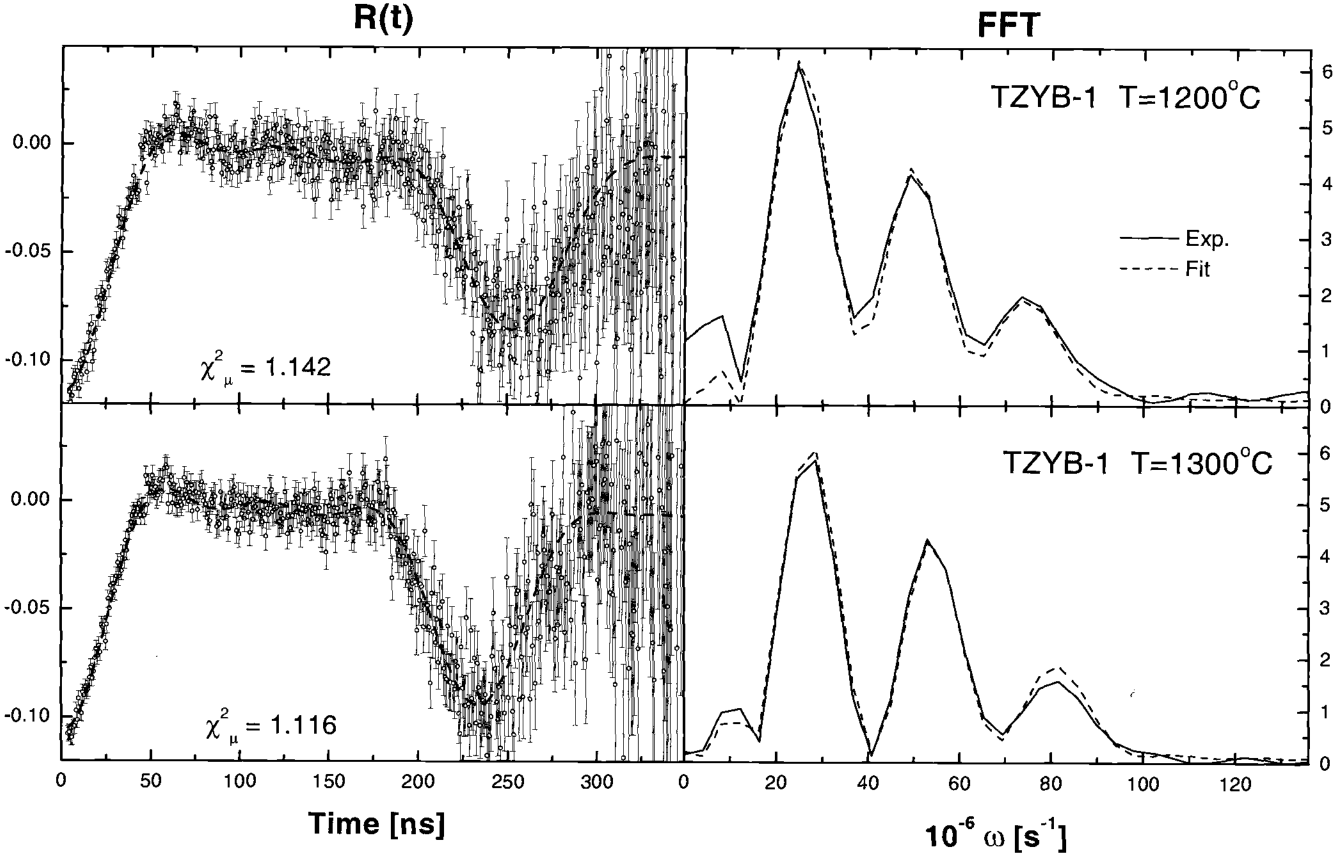

Figure 6.5: PAC time spectra and Fourier transforms for 0.2 at%. Y-doped tetragonal zirconia and fits. Sample TZYB at 1200 and 1300°C.

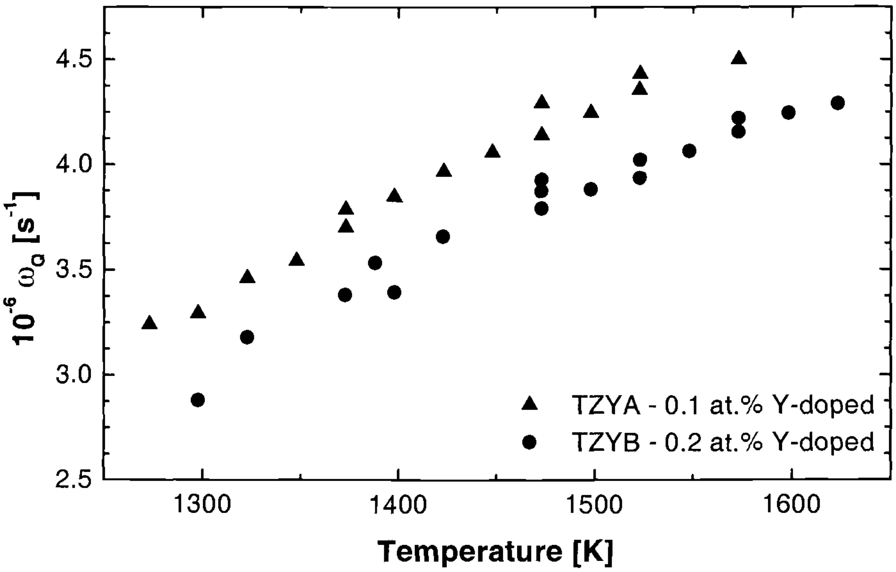

Figure 6.6: Quadrupole interaction frequencies for the samples TZYA and TZYB.

6.4 DISCUSSION OF RESULTS

The quality of the results obtained by the fits is first judged by the χ^2_μ criteria. After results were obtained with the multiple fit program, all the spectra were also fitted separately with the parameters obtained from the multiple fit in order to verify any spurious results. The values of χ^2_μ for the individual fits are in the interval $1.1 < \chi^2_\mu < 1.22$. Figs. 6.2-5 also show that the overall quality of the fits is satisfactory. Fig. 6.6 shows the dependence of the hyperfine parameter ω_Q as a function of the temperature. This figure can be compared with the results shown in Fig. 3.9. The same data sets, TZYA and TZYB, were fitted with different models, [50] and (6.3), and there is a very good agreement between the results. The decrease of the quadrupole interaction frequency ω_Q with temperature can be explained by the trapping of oxygen vacancies by the ^{111}Cd probe nucleus. As a result of the fast motion of the vacancy, the measured quadrupole interaction frequency depends on the average EFG of the sites the vacancy jumps in and out of.

From Table 6.1 a first result is the difference $E_d - E_t$, identified as the binding enthalpy of an oxygen vacancy to the ^{111}Cd probe atom. The values found in this work: 0.57 and 0.56 eV are inreasonable agreement with the value found in [50], 0.62(3) eV.

The hopping energy for a bound vacancy is not expected to be identical to the bulk activation energy of a free vacancy in yttria-doped zirconia. But, it still interesting to compare the hopping energies in both situations as it is physically reasonable to expect them to have similar values. Values for the activation energy in zirconia , measured by other techniques and various dopant content, range from 0.78 to 1.1 eV [81, 82, 83, 84, 85]. The hopping energies listed in Table 6.1 are comparable to these values, indicating that the hopping energy of a bound vacancy can be a good estimate of the bulk activation energy. Also, values of the hopping energies are comparable to the activation energies found in yttria-doped zirconia with Hf PAC [47] .

The prefactors in Table 6.1 can also yield important information about the samples and the fitting procedures. The prefactor w_{t0} is dependent on the concentration of vacancies in the sample. The ratio of the w_{t0} for the two samples is: $\frac{w_{t0}(0.2at.\%)}{w_{t0}(0.1at.\%)} \sim 1.7$. If the only source of vacancies in the material is the dopant, this ratio must be 2. Since impurities introduce an unknown quantity of vacancies, the value found for this ratio is reasonable. The fitted values of the prefactors w_0 and w_{d0} are also physically acceptable.

7 CONCLUSION

Perturbed Angular Correlation spectroscopy can be a very powerful technique to investigate the properties of materials. PAC is a non-contact, non destructive, microscopic probe that can measure the strength and the symmetry of electric field gradients in the proximity of the PAC probe nucleus. Time-varying interactions can provide information about the dynamics of defect transport in the material.

To extract physically meaningful data from a PAC experiment, the PAC spectra must be interpreted correctly. The complexity of the interaction between the PAC probe nucleus and its environment makes the spectra interpretation very difficult to model, particularly when static and dynamic defects are present simultaneously in the material.

In order to isolate the influence of static defects on the PAC spectra, a model (SRDM) that consists of random distributions of point charges in a probe site was developed. Although the SRDM could simulate, with certain success, the presence of defects in cubic materials, it produced inconclusive results in the study of Nb-doped tetragonal zirconia. The PAC data was well fitted with the SRDM, but more work is needed to establish a clear correspondence between the results of the model and the line broadening observed on the PAC spectra.

The influence of defects on the PAC spectra were obtained from the analysis of the Nb-doped tetragonal zirconia with a conventional static model. From fits of the spectra with this model, it was found that the line broadening parameter δ can be expressed as a function of the asymmetry parameter η as:

$\eta = 0.12(3) \times \delta(\%)^{0.51(2)}$.

To extract information about the dynamics of oxygen vacancies in yttria-doped zirconia, a four state stochastic model was combined with results from the static model so that the influence of static defects are also considered when PAC spectra is analysed. The multiple fit of PAC spectra of yttria-doped zirconia taken at various temperatures yielded the energies of activation of a vacancy moving about a probe nucleus. Two samples of yttria-doped zirconia with different concentrations of yttria were analysed. The sample with 0.1 at.% Y yielded the following results: hopping energy E_h = 0.91(6) eV, detrapping energy E_d = 1.54(8) ev and trapping E_t = 0.96(7) eV. For the sample with 0.2 at.% it was found: hopping energy E_h = 0.86(7) eV, detrapping energy E_d = 1.49(7) eV and trapping E_t = 0.95(8) eV. These values are physically reasonable and are in good agreement with values for activation energy for yttria-doped zirconia found by other methods.

It is important to emphasize that the interpretation of PAC spectra is not a straightforward process. It is not difficult to derive mathematical functions that will fit the observed PAC spectra with success, but that are not physically meaningful. One of the objectives of this work was to model the presence of static defects in a material. Although the SRDM did not yield unambiguous results, it indicates that certain procedures such as the use of a Lorentzian line profile to model line broadening may be physically valid. Also, the SRDM suggests that mechanisms that result in asymmetric line profiles should also be taken into consideration.

REFERENCES

[1] R. Vianden, *Hyp. Interact.*, **15/16**, 1081, 1983.

[2] G. L. Catchen, *J. Mater. Educ.*, **12**, 253, 1990.

[3] T. Butz, *Hyp. Interact.*, **84**, 477, 1994.

[4] Gary S. Collins, Washington State University, PAC Groups worldwide. Retrieved October, 15, 2002, from: http://defects.physics.wsu.edu/hfi-group-links.html

[5] G. Schatz and A. Weidinger, *Nuclear Condensed Matter Physics*, John Wiley & Sons, New York, 1994.

[6] K. S. Krane, *Introductory Nuclear Physics*, John Wileys & Sons, New York, 1987.

[7] P. Marmier and E. Sheldon, *Physics of Nuclei and Particles*, Vol. 1, Academic Press, New York, 1969.

[8] H. Fraunfelder and R. M. Steffen, in *Alpha, Beta and Gamma-Ray Spectroscopy*, Volume 2, ed. by K. Siegbahn. North-Holland, Amsterdan, 1965.

[9] D. W. Tom, Ph.D. Thesis, Oregon State University, unpublished, 1995.

[10] J. W. Griffith, Ph.D. Thesis, Oregon State University, unpublished, 2002.

[11] D. Wegner, *Hyp. Interact.*, **23**, 79, 1985.

[12] T. Butz, *Hyp. Interact.*, **52**, 189, 1989.

[13] E. Gerdau, et al., *Proc. R. Soc. A* **311** 197, 1969.

[14] L. A. Mendonza-Zelis, et al., *Hyp. Interact.*, **3**, 315, 1977.

[15] A. M. Stoneham, *Theory of Defects in Solids*, Clarendon Press, Oxford, 1975.

[16] A. Abragan and R. V. Pond, *Phys. Rev.*, **92**, 943. 1953.

[17] A. G. Marshall and C. F. Meares, *J. Chem. Phys.*, **56**, 1226, 1972.

[18] J. Lu. Ph.D. Thesis, Brigham Young University, unpublished, 1995.

[19] P. R. Andrade, et al., *Phys. Rev.*, **188**, 571, 1969.

[20] P. R. Andrade and J. D. Rogers, *Phys. Rev. B*, **3**, 1052, 1971.

[21] H. Guan. Ph.D. Thesis, Brigham Young University, unpublished, 1994.

[22] M. Blume, *Hyperfine Structure and Nuclear Reactions*, ed. E. Mathias and D. A. Shirley, North Holland, Amsterdam, 1968.

[23] M. Blume, *Phys. Rev*, **174**, 351, 1968.

[24] H. Winkler and E. Gerdau, *Z. Physik*, **262**, 363, 1973

[25] A. Baudry and P. Boyer, *Hyp. Interac.*, **35**, 803, 1987.

[26] W. E. Evenson, et al., *Hyp. Interact.* **61**, 1379, 1990.

[27] W. E. Evenson, et al., *Hyp. Interact.* **62**, 283, 1990.

[28] W. E. Evenson, et al., *Hyp. Interact.* **C 1**, 392, 1996.

[29] W. E. Evenson et al., *Hyp. Interact.* **120/121**, 427, 1999.

[30] Y.M. Chiang, D. P. Birnie and W. D. Kingery. *Physical Ceramics*. John Wiley and Sons, New York, 1997.

[31] R. Stevens. *Zirconia and Zirconia Ceramics*. Magnesium Elektron Publication no. 113, Twickenham, United Kingdon, 1986.

[32] Eugene Ryshkewitch. *Oxide Ceramics*. Academic Press, New York, 1960.

[33] A. H. Heuer and L. K. Lenz, *J. Am. Ceram. Soc.*, **65**, 192, 1982

[34] L. Bragg, et al., *Crystal Structure of Minerals*, Cornell Univesity Press, Ithaca, 1965.

[35] R. W. G. Wyckoff, *Crystal Structures*, volume 2. Interscience Publishers, second edition, 1963.

[36] C. J. Howard, *Acta Cryst.*, **B44**, 116, 1988.

[37] P. Aldebert and J. P. Traverse,*J. Am. Ceram. Soc*, **1985**, 34, 1985.

[38] W. M. Kriven et al. *The martensitic crystallography of tetragonal zirconia* in *Science and Technology of Zirconia*, Vol. 3, 82 (1980).

[39] G. Teufer, *Acta. Cryst.*, **15**, 1187,1962.

[40] M. O. Zacate, Ph. D. Thesis, Oregon State University, unpublished, 1997. Vol. 3, American Ceramic Society, 1981.

[41] O. J. Whitmore Jr. and N. N. Ault, *J. Am. Ceram. Soc.*, **39**, 443, 1956.

[42] R. W. Vest, et al., *J. Am. Ceram. Soc.* , **47**, 635, 1964.

[43] R. W. Vest and N. M. Tallan, *J. Am. Ceram. Soc.*, **48**, 472, 1965.

[44] L. A. McClaine and C. P. Coppel, *J. Electro. Chem. Soc.*, **108**, 312, 1961.

[45] P. Kofstad and D. J. Ruzicka, *J. Electrochem. Soc.*, **110**, 181, 1963.

[46] J. Xue and R. Dieckman, *Solid State Ion.* **8**, 36C, 1991.

[47] H. Jaeger, Ph.D. Thesis, Oregon State University, unpublished, 1987.

[48] H. Jaeger et al. in *Better Ceramics Through Chemistry II* edited by C.J. Brinker, D. E. Clark and D.R . Ulrich, MRS Symposium Proceedings, Vol 73, Material Research Society, Pittsburgh, 1986.

[49] H. T. Su, Ph. D. Thesis, Oregon State University, unpublished, 1989.

[50] Niels Mommer et al., *Phys. Rev. B*, **61**, 162, 2000.

[51] Hang-Tzong Su et al., *J. Am. Ceram. Soc.* **73**, 3215 (1990).

[52] Theresa A. Lee, Ph.D. Thesis, Oregon State University, unpublished, 2000.

[53] W. H. Warnes and J. A. Gardner, *Phys. Rev. B*,**40**, 4276, 1986.

[54] H. Jaeger, et al., *Rev. Sci. Instrum.*, **58** 1694, 1987.

[55] A. R. Arends, et al., *Hyp. Interac.*, **8**, 191, 1973.

[56] R. Lumdquist, Ph.D. Thesis, Oregon State University, unpublished, 1994.

[57] Ethan Bernard, Senior Thesis, Oregon State University, unpublished, 2000.

[58] W. H Press, et al., *Numerical Recipes, the Art of Scientific Computing*, Second Edition, Cambridge University Press,Cambridge, 1987,

[59] P. R. Bevington, *Data Reduction and Error Analysis for the Physical Sciences*, McGraw-Hill, New York, 1969.

[60] R. K. Landau and Manuel J. Paez, *Computational Physics*, John Wiley & Sons, New York, 1997.

[61] T. Vattulainen, et al., *Phys. Rev. Lett.*, **73**, 2513, 1994.

[62] T. Vattulainen, Research Institute for Theoretical Physics, Studies of Random Numbers. Retrieved January, 6, 2003, from: http://www.physics.helsinki.fi/ vattulai/rngs.html

[63] P. Andrade, et al., *Phys. Rev. B*, **1**, 2912, 1970.

[64] E. Gerdau, et al., *Z. Phys.*, **263**, 5, 1973.

[65] M. Forker, et al., *Z. Phys. Chem, Neue Folge*, **163**, 889, 1989.

[66] M. Forker, et al., *Nucl. Instr. and Methods in Physics. Res. A*, **337**, 534, 1993.

[67] B.P. Hemming and R.M. Steffen, *Phys. Rev.*, **92**, 832, 1953.

[68] R.M. Steffen, *Phys. Rev.*, **103** , 116, 1956.

[69] H.F. Wagner, et al., *Z. Phys.*, **248** , 195, 1971.

[70] M. Forker, *Phys. Rev. B*, **57**, 5177, 1998.

[71] R. Berend, et al., *Nucl. Instr. and Methods*, **69**, 41, 1969.

[72] M. Forker, *Nucl. Instr. and Methods*, **106**, 121, 1973.

[73] C. Budtz-Jorgensen and K. Bonde-Nielsen, *Hyp. Interact.*, **1**, 81, 1975.

[74] A. M. Stoneham, *Rev. Mod. Phys.*, **41**, 82, 1969.

[75] R. E Alonso and A. Lopez-Garcia, *Z. Naturforsch*, **B42**, 1885, 1990.

[76] R. E. Alonso et al., *J. Physics: Cond. Mat.*. **10**, 2139, 1998.

[77] H. Steele, *Mater. Science Engrg.*, **B1 3**, 79, 1992.

[78] John A. Gardner et al., *Hyp. Interact*, **120/121**, 523, 1999.

[79] A. S. Nowick, *Diffusion in Crystalline Solids*, ed. by G. E. Murch and A. S. Nowick, Academic Press, New York, 1984.

[80] A. N. Cormack and C. R. W. Catlow, *Transport in Nonstoichiometric Compounds*, ed. by G. Simkovich and V. S. Stubican, Plenum Press, New York, 1985.

[81] T. K. Gupta et al., *J. Electrochem. Soc.*, **128**, 929, 1991.

[82] S. Ikeda et al., *J. Mater. Sci.*, **20**, 4593, 1985.

[83] N. Bonanos and E. P. Butler, *J. Mater. Sci. Lett.*, **4**, 561, 1985.

[84] C. Leon et. al., *Phys. Rev. B*, **55**, 882, 1996.

[85] F Capel, et al., *J. Mater. Sci. Lett.*, **35**, 345, 2000.